Magneto-transport properties of some disordered binary and ternary alloys

Thesis submitted for the degree of

Doctor of Philosophy (Science)

in Physics

by

Pampa Pal

Department of Physics

University of Calcutta

January, 2014

Dedicated to my parents…..

Abstract

This thesis describes the unusual effects in some disordered binary (Ni-Mn) and ternary (Ni-Fe-Cr) alloys seen through structural and magneto-transport measurements.

Magnetic phase diagram has been constructed in disordered $Ni_{100-x}Mn_x$ system over a wide concentration range ($15 \leq x \leq 37$) encompassing the critical concentration ($x \sim 25$) in the temperature range $5 \leq T \leq 300$ K. From different magnetic data at several temperatures and applied fields, we find a double transition, one from a paramagnetic to a ferromagnetic long-range order (LRO) at T_C and then another to a ferro-spin-glass mixed phase at T_{SG} for $x \leq 25$ at. % Mn. Then a conventional/canonical spin-glass state appears which gradually evolves to an antiferromagnetic LRO around 37 at. % Mn. From transport measurements below and above the multicritical point (MCP) we found, in the ferromagnetic/ferro-spin-glass ($x \leq 25$) phase, $\rho(T)$ is dominated by large electron-phonon and electron-magnon s-d scattering while in the spin-glass/antiferromagnetic regime ($x \geq 25$) resistivity minima show up due to larger disorder with resistivity ~ (150-185) μΩcm. Here $\rho(T)$ is dominated by e-e interaction ~ $-\sqrt{T}$ and electron-phonon s-d scattering. The magnetoresistance is negative below and positive above the MCP.

Another systematic study has been done to determine the magnetic and transport properties as well as the critical exponents of a set of Cr-rich γ-Ni-Fe-Cr alloys. The static critical exponents and the amplitudes, related to the transition near T_C, are obtained through detailed DC-magnetization and AC-susceptibility measurements. The values depart significantly from those of the 3D-Heisenberg model predictions and those of pure Ni due to the competing pair interactions in the system. In addition, both the resistivity and the magnetoresistance measurements reveal their diverse magnetic phases. For FM and AFM alloys, the resistivity varies as CT^2 above the resistivity minima and the value of C decreases while approaching the higher temperature region and finally it varies as T, consistent with the magnetic states.

Acknowledgements

First and foremost, I would like to thank my supervisor Prof. A. K. Majumdar and joint supervisor Prof. A. Mookerjee for their constant support, patience, and encouragement throughout the course of my Ph.D work. I am fortunate to enjoy learning under their guidance. Prof. Majumdar is not only actively involved in each and every step of this thesis, but also his philosophy of life and science inspired me a lot, which will always show me path in future. Prof. Mookerjee always has lucid explanations of theoretical complications. It would have been impossible to give this thesis a meaningful shape without his theoretical work and keen interest in experiments. I am leaving with a bundle of rich experience and sweet memories I gathered from their friendly company over the years.

I am grateful to Prof. A. K. Nigam and his group at TIFR, Mumbai for sacrificing their valuable time and busy schedule to make the measurement facilities available to me.

Though all of my friends of S N Bose Centre always extended their helping hand, I should mention blessings, help, and care I got from my senior, Dr. Mitali Banerjee during my work. The entire library staff especially Mr. R. Acharyya's help is gratefully acknowledged.

Financial assistance from project No. SR/S2/CMP-18/204 of the Department of Science and Technology, Government of India, and the facilities provided by S. N. Bose National Centre for Basic Sciences are gratefully acknowledged.

My beloved husband, Dibyendu has been my most caring companion throughout the period of my research work. His faithful support is keenly appreciated.

Finally, I would like to express my deepest gratitude to my family, parents-in-law, and my brother for their love and encouragement. My parents raised me with a love of science and supported me in all my pursuits. Their unconditional love and support throughout my life is immeasurable. Thank you all.

Pampa Pal

List of publications forming part of the thesis

I. **Pampa Pal** et al., "Magnetic ordering in Ni-rich NiMn alloys around the multicritical point: Experiment and theory", Phys. Rev. B **85**, 174405 (2012).

II. **Pampa Pal**, A. K. Majumdar, and A. K. Nigam, "Electrical resistivity in disordered NiMn alloys around the multi-critical point", Journal of Magnetism and Magnetic Materials **341**, 65 (2013).

III. **Pampa Pal**, A. K. Majumdar, and A. K. Nigam, Magnetoresistance in disordered NiMn alloys around the multicritical point, Invited talk at the 5th Seeheim Conference on Magnetism, SCM2013, Frankfurt, Germany, September 29-October 3, 2013.

IV**.** **Pampa Pal**, A. K. Majumdar, and A. K. Nigam, "Probing exotic magnetic phases and critical behavior of Ni-rich γ-NiFeCr alloys", to be communicated.

V. **Pampa Pal**, A. K. Majumdar, and A. K. Nigam, "Magneto-transport studies in Ni-rich γ-NiFeCr alloys", to be communicated.

Contents

CHAPTER II: Sample Preparation and Experimental Details

CHAPTER III : Magnetic ordering in Ni-Mn alloys around the multicritical point: Experiment and Theory

List of Figures

List of Tables

CHAPTER I

Introduction

1.1 Disordered systems and their applications

Disordered magnetic alloys and compounds are backbones of modern technology and attract physicists ever since the development of solid-state physics. “Disorderness” governs extrinsic magnetic properties, such as coercivity, remanence, and energy of an intrinsically magnetic material. Nowadays we are getting benefitted from numerous applications of magnetic materials in electronics, detectors, magnetic storage devices, etc. Even if magnetic properties of a material are not used in a particular application, the presence of magnetic order often influences and must be taken into the account when describing other physical properties and processes, which are not directly connected to magnetism – like mechanical properties, structural stability, type of chemical order, temperature dependence and anisotropy of the electrical resistivity, and even recently invented magnetically mediated superconductivity. An atom is characterized by a magnetic moment which is a result of fundamental symmetries of nature and laws of quantum mechanics, such as, in particular, the Pauli Exclusion Principle. On the other hand, when atoms are put together to form a solid body, all atomic symmetries are broken, and it seems at first that there is no space for magnetism in this case. However, the collective behavior of electrons in a solid brings about new effects caused by quantum correlations between electrons, and magnetism arises as a subtle balance between different sorts of correlations. The term “disordered alloy” in general include liquid, vapour or plasma quenched materials as well as alloys obtained by solid state synthesis, whose x-ray diffraction patterns show characteristic broad rings. In solid solutions, the correlations between chemical and magnetic interactions play an important role in determining the magnetic phase diagram of transition-metal alloys. These alloys lack long-range atomic order and consequently exhibit high metallic resistivity (100-200 μΩcm) and no macroscopic magneto-crystalline anisotropy due to the absence of crystal structure. As a result, ferromagnetic 3d transition metal-based ones are generally good “soft” magnetic materials with both low dc hysteresis loss and low eddy current dissipation. In addition, they are characterized

by high elastic limit (i.e., they resist plastic deformation) and for this character they are good corrosion resistant metals. Studying magnetic properties of disordered alloys is important both for the understanding of phase transformation in alloys and from the point of view of fundamental issues of magnetism in solids. Disorder and its degree of ordering in a magnetic system can result in unconventional magnetic structures, such as canonical spin glass, re-entrant spin glass, etc. C. Zener, as early as 1955, in his seminal work "Impact of magnetism on metallurgy"[1], noted that understanding of magnetism is crucial for production and application of alloys. The "exchange bias" phenomena, discovered by Meiklejohn and Bean[2], is the subject of flourishing studies connected to applications in spin-valve devices. Recently, much attention has been given to the studies of the magnetic coupling across a ferromagnet and an antiferromagnet, which is the key element towards understanding the phenomenon. The interaction between an antiferromagnet and a ferromagnet results in a unidirectional anisotropy, which manifests itself through a displaced hysteresis loop. The shift can be useful in controlling the magnetization in devices, such as spin-valves which sense changing magnetic fields through magnetoresistance effects.

1.2 Magnetic Ordering: Different types

The basic criteria for the onset of magnetic order in solids are (i) individual atoms should have magnetic moments (spins) and (ii) exchange interactions must exist between the atoms that couple them together. Exchange coupling originates from overlapping of the electronic wave functions of neighbouring atoms. The exchange interactions depend sensitively upon the interatomic distance and the nature of the chemical bonds, particularly of nearest neighbour atoms. The subject of disordered magnetic systems comprises of the whole field of applied magnetic materials, ranging from extremely soft permalloys to the hardest permanent magnets as well as the physics of model systems of strongly disordered magnetic materials like spin glasses. Magnetic ordering requires that the electron system forms local or itinerant magnetic moments and that there is interaction between these moments. Such interacting magnetic moments will eventually become correlated with temperature and in certain cases form a long-range ordered phase at some critical temperature. A wide variety of magnetic order exists in disordered systems

in the presence of various kinds of disorder. The most commonly known among them are ferromagnetism, paramagnetism, diamagnetism, ferrimagnetism, and antiferromagnetism. Except diamagnetism, all other magnetic properties can be understood classically by the molecular field theories. Some more possible magnetic ordering in disordered systems apart from conventional ferromagnetic and antiferromagnetic orderings are superparamagnetism, spin-glass, cluster-glass, re-entrant spin-glass, etc. A few atomic percent of magnetic impurity in noble metal host or vice versa can give rise to a new magnetic phase known as spin glass, where randomness invokes a competition between the impurity spins/moments when it comes to ordering. The magnetism of intermediate concentration regime of these systems, from time to time, has been interpreted in terms of "ensemble of mutually interacting ferromagnetic and antiferromagnetic domains"[3]; "micromagnetism"[4], "rock magnetism"[5] and "superparamagnetism" based on phenomenological model of Néél[6,7] and developed as "magnetic clusters" or "magnetic clouds"[8] ; and finally "spin-glass"[9] and "cluster-glass"[10]. The two crucial ingredients necessary to produce a spin-glass are disorder and frustration. The canonical representatives of spin-glasses have an oscillatory indirect long-range Ruderman-Kittel-Kasuya-Yosida (RKKY) spin-spin interaction mediated by conduction electrons[11]. The standard Edwards-Anderson model[12] has quenched random nearest-neighbor couplings of both signs which mimics the frustrating effect of the longer-range RKKY interaction. In both cases, as well as in many others, it is the interaction which is both disordered and frustrating (*i.e.* mixture of ferromagnetic (FM) and antiferromagnetic (AFM) couplings) that is responsible for the appearance of a spin-glass phase. There is also a large class of materials where frustration has geometrical origin: the combination of the AFM interactions and geometry of the lattice suppresses the natural AFM order[13] and makes the system extremely susceptible to perturbations. In this case often even a small disorder in the coupling strengths, that does not change their AFM character, is enough to obtain a spin-glass phase[14,15].

Thus when we keep on substituting randomly transition metals with unpaired 3d-electrons like Mn, Fe, or Cr, first we encounter the Kondo regime where the 3d-electrons of magnetic ion interact antiferromagnetically with the conduction electrons. At low temperatures, this interaction makes the isolated magnetic ion non-magnetic and enhances the electron scattering cross-section giving rise to resistivity minimum. When we add more of magnetic ions in the system, they start interacting with each other through, say, RKKY

interaction. This indirect inter-impurity interaction opposes the weakening of moments due to Kondo effect, and beyond a certain concentration of magnetic ions we see the stabilization of magnetic moments where, what is called "good" moment, is formed. Here we encounter a magnetic phase which is commonly known as spin-glass. Below a certain glass transition temperature, many interesting magnetic phenomena like irreversible effects, time-dependent magnetic properties resulting from the randomly frozen (for time intervals over which experiments are carried out) magnetic moments with a degenerate ground state, etc. take place. Also, we come across the effect of "measurement time" on the freezing in a particular experiment, indicating non-equilibrium phenomena, often referred to as non-ergodicity. The manifestation of the irreversible effects, time-dependent magnetic properties, and effects of "measurement time" on the freezing can be seen from many experimental signatures. The state of randomly frozen spins can give rise to a quenched disorder in an otherwise crystalline solid. The randomly distributed magnetic ions interact with one another through RKKY interaction, whose magnitude and sign depend on the distance between the magnetic ions. Thus, spins interact with one another ferro- or antiferromagnetically, depending on their distances. As a result, we find that contradictory interactions coming through different paths are experienced by a magnetic ion. This conflicting situation is called "frustration"[16]. Thus, quenched magnetic disorder and frustration are the basic ingredients of the spin-glass phase which is achieved without having a spatial long-range magnetic order.

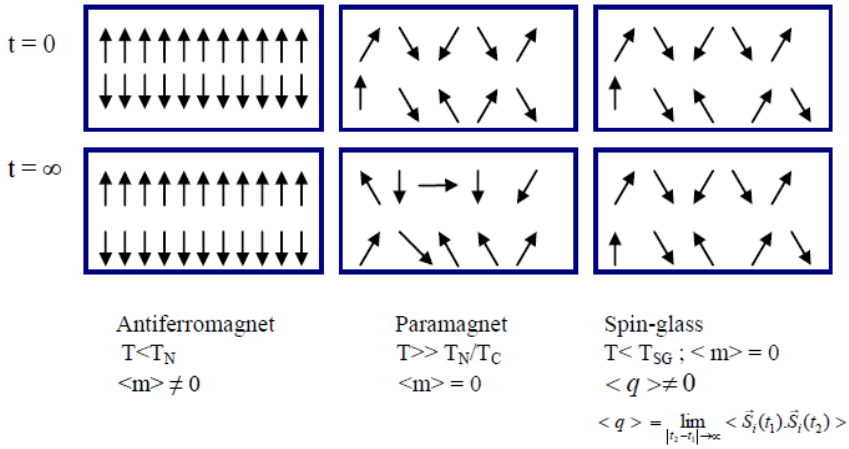

Fig.1.1 Example of random freezing in a spin-glass.

The meaning of random freezing may get clarified in Fig. 1.1 where <m> is the average magnetization while <q> , an auto correlation function, is the order parameter of the spin-glass state and we see that, though the spins in both the paramagnet and the spin-glass are randomly oriented, unlike paramagnets the spin-glass are frozen in time. The spins in an antiferromagnet (shown above at T = 0) seem to be frozen but they are not random and have a long-range order. Quenched disorder and frustration are the two important common features of all the spin-glasses, irrespective of the origin of these two characteristics. This is the reason why we observe spin-glass phenomenon in conducting crystalline and amorphous alloys as well as in insulating systems. Mydosh[17] has classified various types of spin-glasses.

1.3 Magnetic properties

1.3.1 Time Dependent Magnetization

A time-dependent magnetization is not a unique property of canonical spin glass only. It is observed for ferromagnetic and superparamagnetic clusters as well[18]. When a system with superparamagnetic clusters is slowly cooled in a magnetic field H from a temperature which is more than the freezing temperature (T_f) or the blocking temperature (T_B), the system acquires a magnetization M at low temperatures ($T<T_f$) which is almost the equilibrium magnetization at that temperature and field. The change in magnetization with time is given by

$$M(t) = M_0 e^{-\lambda t}, \qquad (1.1)$$

where λ is the relaxation rate.

This type of change in magnetization involves a single relaxation time or barrier height with a constant energy. However, in real systems this type of decay is not observed. So, Street and Woolley[19] considered the change in magnetization with time involving a distribution of relaxation times or a distribution of energy barriers [f (E,t)] and according to their treatment the magnetization varies with time as

$$M(t) = M_0 - S \ln t, \qquad (1.2)$$

where S ∞ < m > and < m > is the average magnetization.

In ferromagnets, attempts have been made to explain the magnetic relaxation using a model based on magnon relaxation on a percolation distribution of finite domains[20]. The other popular prediction of relaxation is the power law decay[21] which can be obtained from scaling theories of domain growth[22] and internal dynamics[23].

1.3.2 Saturation Magnetization

Saturation magnetization M_s is the maximum magnetization under finite large magnetic fields. Assuming each magnetic atom has the same magnetic moment, M_s is dependent only on the magnitude of the atomic magnetic moment 'm' and the number of atoms per unit volume 'n'. Theoretically, we expect saturation magnetization to be insensitive to the metallurgical conditions of the specimen, i.e., saturation magnetization is an intrinsic property of a material. However, for nanostructured materials, as a large fraction of atoms are at the surface and interface, M_s can be significantly affected by the particle size and synthesis route. For example, nanoparticle samples prepared by ball-milling are found to give a value of saturation magnetization much lower than samples prepared by chemical synthesis. Saturation magnetization is found to be reduced with respect to its bulk counterpart. This has been attributed to the existence of magnetic disordered surface called dead layer surrounding ferro/ferrimagnetically aligned core region[24]. According to the other proposed models by Morrish et al.[25] lower values of the observed magnetization were due to surface spin canting. In another study, Pankhurst et al.[26] have argued that this is due to non saturation effects because of the random distributions of anisotropy axes in ferromagnetic particles. Parker et al.[27] have suggested that the canting occurs in the whole particle because of quantum size effects. On the other hand, the microscopic surface magnetic moment has been found to be higher. Moreover, for a bulk material the temperature dependence of saturation magnetization is found to follow Bloch's $T^{3/2}$ law, but the nanometric particles show a deviation from $T^{3/2}$ behavior.

1.3.3 Hysteresis Loss and Coercivity

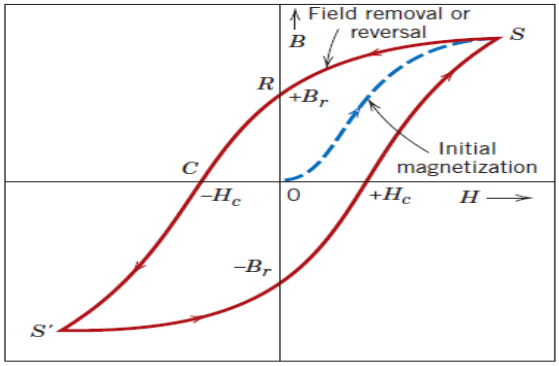

Fig.1.2 Magnetic flux density versus the magnetic field strength for a ferromagnetic material that is subjected to forward and reverse saturations (points S and S'). The hysteresis loop is presented by the solid red curve; the dashed blue curve indicates the initial magnetization. The remanence B_r and the coercive force H_c are also shown.

A hysteresis effect is produced in which B lags behind H. This behavior and saturation magnetization may be explained by the motion of domain walls. Upon reversal of the field direction from saturation, the process by which domain structure changes is reversed. First, there is a rotation of the single domain with the reverse field. Next, domains having magnetic moments aligned with the new field form and grow at the expense of the former domains. Critical to this explanation is the resistance to movement of domain walls that occurs in response to the increase of the magnetic field in the opposite direction; this accounts for the lag of B with H, or the hysteresis. When the applied field reaches zero, there is still some net volume fraction of domains oriented in the former direction, which explains the existence of remanence B_r. To reduce the field, B, within the specimen to zero, and applied field, H, of magnitude $-H_c$ must be applied in a direction opposite to that of the original field; H_c is called the coercivity, or sometimes the coercive force. Upon continuation of the applied field in the reverse direction, as indicated in the figure, saturation is ultimately achieved in the opposite sense. A second reversal of the field to the point of the initial saturation completes the symmetrical hysteresis loop and also yields both a negative romance ($-B_r$) and a positive coercivity ($+H_c$). Irreversibility gives

rise to hysteresis, a phenomenon that can be visualized by plotting either M or B= μ_0(H+M) as a function of H. Positive values of B and H represent fields in one direction, while negative values represent fields in the opposite direction.

1.3.4 AC susceptibility

AC magnetic susceptibility, in which an AC field is applied to a sample and the resulting AC moment is measured, is an important tool for characterizing many states of materials. Since the induced sample moment is time-dependent, AC measurements yield information about magnetization dynamics as well which are not obtained in DC measurements, where the sample moment is constant during the measurement time. In AC magnetic measurements, a small AC drive magnetic field is superimposed on the DC field, causing a time-dependent moment in the sample.

As long as the AC field is small, the induced AC moment is $M_{AC} = (dM/dH)\, H_{AC} \sin(\omega t)$ where H_{AC} is the amplitude of the driving field, ω is the driving frequency, and $\chi = dM/dH$ is the slope of the *M(H)*curve, called the linear magnetic susceptibility. In the higher frequency case, the magnetization of the sample lags behind the driving field. Thus, this linear AC magnetic susceptibility measurement yields two quantities: the magnitude of the susceptibility, χ, and the phase shift, φ (relative to the drive signal). Alternately, one can think of the susceptibility as having an in-phase, or real, component χ' and an out-of-phase, or imaginary, component χ''. They are related by

$$\chi' = \chi \cos\varphi \quad \text{and} \quad \chi'' = \chi \sin\varphi \,. \qquad (1.3)$$

In general, the nonlinearity of magnetization in the presence of a magnetic field is given by[28] the series expansion :

$$m = m_0 + \chi_0 h + \chi_1 h^2 + \chi_2 h^3 + \ldots\ldots, \qquad (1.4)$$

where m_0 is the spontaneous magnetization, χ_0 the linear, and χ_1, χ_2 are the non-linear susceptibilities, and h is the applied field. For ferromagnetic (FM) samples *m* has no inversion symmetry with respect to the applied field because of the spontaneous magnetization, unlike an SG. Hence for an SG where no spontaneous magnetization is present, *m* can be expressed as an odd power series in *h* as[29]

$$m = \chi_0 h + \chi_2 h^3 + \chi_4 h^5 + \ldots\ldots, \qquad (1.5)$$

1.4 Characterization

1.4.1 Crystal structure

X-ray powder diffraction (XRD) is an experimental technique that is commonly used to study crystalline materials. The three-dimensional structure of non-amorphous materials is defined by regular, repeating planes of atoms that form a crystal lattice. When a focused X-ray beam interacts with these planes of atoms, parts of the beam are transmitted, absorbed by the sample, refracted, scattered, and diffracted. When an X-ray beam hits a sample and is diffracted, we can measure the distances between the planes of the atoms that constitute the sample by applying Bragg's Law. Bragg's Law is $n\lambda=2d\ sin\theta$, where the integer n is the order of diffraction, λ is the wavelength of the incident X-ray beam, d is the distance between adjacent planes of atoms (the d-spacings), and θ is the angle of incidence of the X-ray beam. Since we know λ and we can measure θ we can calculate the d-spacings. The characteristic set of d-spacings and theirs intensity generated in a typical X-ray scan provides a unique "fingerprint" of the phases present in the sample. When properly interpreted, by comparison with standard reference patterns and measurements, this "fingerprint" allows for identification of the material. The unit-cell parameters and the crystal structure could be also refined for the identified phases. Powerful modern softwares (RietVeld, FullProf Suite, Powder Cell, *etc.*) are used to solve these problems.

XRD methods for crystallite size determination are applicable to crystallites in the range of 2-100 nm. The diffraction peaks are very broad for crystallites below 2-3 nm, while for particles with size above 100 nm the peak broadening is rather small. If analyzed crystals are free from microstrains and defects, peak broadening depends only on the crystallite size and diffractometer characteristics. In this case classical Scherrer equation is used for crystallite size determination: $d=(Kxl)/(b\ x\ cosq)$, where d is the crystallite size, l is the X-ray wavelength, b is the width of the peak (full width at half maximum (FWHM) or integral breadth) after correcting for instrumental peak broadening (b expressed in radians), q is the Bragg angle and K is the Scherrer constant. The d value, calculated for the (hkl) peak, should be understood as mean crystallite size in the direction that is perpendicular to the (hkl) plane (hkl is Miller indices).

Our systems are $L1_0$ type magnetic alloys. The fcc structures have all their faces and their corner sites occupied by the same atoms, or in the case of an alloy, the probability of each site being occupied by a specific type of atom is the same. $L1_0$ is a crystallographic derivative structure of the fcc and has two of the faces occupied by one type of atom and the corner and the other face occupied with the second type of atom. An important crystallographic feature of the $L1_0$ structure is its c/a ratio. For most structures c/a is less than one. It should be pointed out that even if the values of a and c were equal, the symmetry of the unit cell is tetragonal since there is no three-fold axis and only one four-fold axis. Another important aspect of the structure is the number and type of near neighbors. Since the distortion is small we can say that in the $L1_0$ structure there are 12 near neighbors (along the <110> directions) and six next near neighbors (along the <100> directions).

1.4.2 Chemical Compositions

Each of the alloying elements and their concentrations, in these Ni-based alloys are significantly important for their magnetic and structural properties. So determination of chemical composition of constituent alloys has been done using Energy Dispersive X-Ray analysis, referred to as EDXA. This is an x-ray technique to identify the elemental compositions of materials. EDXA makes use of the X-ray spectrum emitted by a solid sample bombarded with a focused beam of electrons to obtain a localized chemical analysis. All elements from atomic number 4 (Be) to 92 (U) can be detected in principle. Qualitative analysis involves the identification of the lines in the spectrum and is fairly straightforward owing to the simplicity of X-ray spectra. Quantitative analysis (determination of the concentrations of the elements present) entails measuring line intensities for each element in the sample. By scanning the beam in a television-like raster and displaying the intensity of a selected X-ray line, element distribution images or 'maps' can be produced. Also, images produced by electrons collected from the sample reveal surface topography or mean atomic number differences according to the mode selected.

1.4.3 Density of states

The number of available electron states as a function of energy E is the density of available states D(E). This density of states is independent of the available electrons to fill the states; it is simply an expression of what energy values are allowed. The occupational density of states N(E) describes the number of electron states per unit energy interval as a function of energy. This is related to the density of available states D(E) through the probability of occupancy f(E) by the equation

$$N(E) = 2\, f(E)\, D(E), \qquad (1.6)$$

where the factor 2 arises because electrons have 2 spin states, up and down[30] and therefore each available energy state can be occupied by two electrons, one with spin-up and the other with spin-down. This simple expression allows the electron distribution to be described in terms of the available levels D(E) as determined by the ionic potential, and the distribution of electrons among these levels f(E) as determined by temperature, for example.

In alloys, the crystal potential depends upon the kind of atoms and sometimes it is considerably higher at the sites occupied by one kind of atom. Then the energy levels belonging to the atom of higher potential go up and are detached from the remaining levels. The detached levels are "antibonding orbitals" and the remaining levels are "bonding orbitals". The Density of States (DOS) of ordered magnetic Ni-Mn alloys is calculated by Linear Muffin Tin Orbital Potential (LMTO) method. These are ferromagnetic Ni_3Mn and antiferromagnetic NiMn alloys. The DOS of NiMn and that of Ni_3Mn in the minority spin-state show a remarkable character. There appears a narrow and high band in the high energy region, which is separated up from the main band. There is a region in the low DOS between them and the Fermi energy lies in it. This means that bonding and antibonding orbitals are well separated in Ni_3Mn and NiMn.

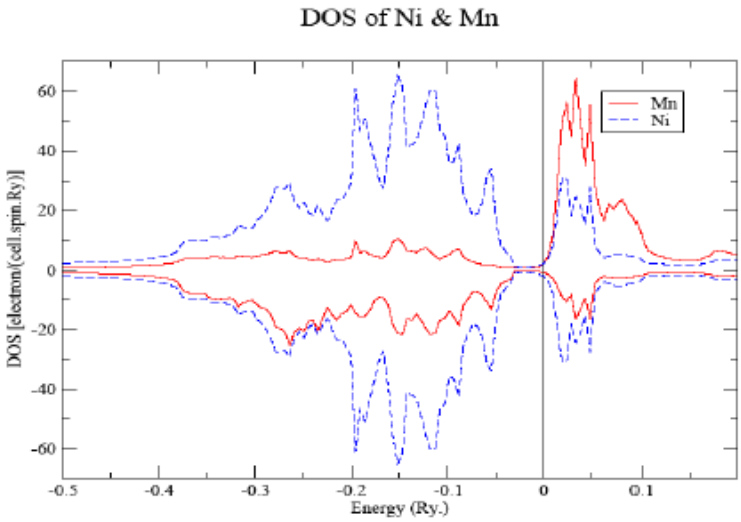

Fig.1.3 Density of states of AFM NiMn alloy for Ni (↑↓) and Mn (↑↓).

The above figure is the density of states of AFM NiMn alloy for Ni (up and down) and Mn (up and down). In this phase the main contribution comes from the d state. The above figure indicates that the density of states for Ni is nearly the same for up and down spin bands but for Mn sites it differs significantly. That's why magnetic moment of Mn exceeds that of Ni. The values of μ obtained for Mn is 3.5 μ_B which agrees satisfactorily with the experimental value ~ 3.8 μ_B and the magnetic moment of Ni is nearly zero.

1.4.4 Phase Diagram

A phase is characterized by a thermodynamic function, typically the free energy. A thermodynamic function is a function of a few macroscopic parameters such as the temperature and the pressure. A *phase diagram* is a graph with those parameters as the axes on which the phase is specified for each point. A typical phase diagram has several specific features including *phase boundaries*, a *critical point*, and a *triple point*. A phase boundary separates different phases. A change in parameters such as the temperature across a phase boundary causes a sudden change in the phase of a substance. A phase boundary sometimes disappears at a critical point where the two phases become indistinguishable and the substance shows anomalous behaviour. Three different phases coexist at the triple point. A phase can be characterized by various

physical quantities, especially the *order parameter*, which measures how microscopic elements constituting the macroscopic phase are ordered in a state.

In magnetic materials, for example, *magnetization* is a characteristic order parameter. With the values of antiferromagnetic, ferromagnetic, spin-glass, or re-entrant spin-glass like transition temperatures on Y-axis and the concentration of transition metal elements in X-axis, one can construct this magnetic phase diagram. This diagram gives a clear idea about different magnetic states at different temperatures as well as at different concentrations of constituting elements.

1.5 Effect of disorder

1.5.1 Magnetic moment variation

The magnetic moment of most amorphous alloys is lower than those of the pure crystalline constituting transition metals. Normally structural disorder in alloys causes little change in the average magnetic moment/atom. The moments are mainly reduced by the change in the local chemical environment caused by the presence of non-magnetic materials. In disordered systems, the fluctuation in nearest neighbour (NN) distance and the degree of overlap of electronic wave functions on neighbouring sites as well as exchange splitting change from site to site giving rise to the variation in local moments.

Magnetic moment variation with composition has been interpreted in Slauter-Pauling like plots. In the general amorphous alloys $(TM)_{1-z-y}F_zG_y$, the magnetic moment of the transition metal atoms can be expressed as[31]

$$\mu = [m(1-z-y)fz-gy]/(1-z-y) \qquad (1.7)$$

Or for the moment per atom of alloy as $\mu = m(1-z-y)fz-gy,$ (1.8)

where F and G represent the metalloid or glass forming atomic species, m is the original number of unpaired spins in the transition metal alloy and f and g are the number of electrons transferred from F and G atoms, respectively.

Some models have been developed to describe the magnetic property variation with alloy content. Magnetic valence model is one of them which is based on Friedel's concept of virtual

bound states and generalized by Terakura and Kanamori[32]. It accounts for the variation of average magnetic moment with alloy content by defining an atom averaged magnetic valence

$$V_m = 2N_d^{\uparrow} - V \qquad (1.9)$$

where V is the average electronic valence $V = N_d^{\uparrow}+N_d^{\downarrow}+ N_{sp}^{\uparrow}+ N_{sp}^{\downarrow}$ and $N_d^{\uparrow}$ is the number of majority-spin d-electrons. Substitution of V in the previous equation leads to the relation

$$V_m = \mu_{av} - 2N_{sp}^{\uparrow} \qquad (1.10)$$

which demonstrates the Slater-Pauling like behavior. This model is applicable to a wide range of transition metal and metalloid alloys.

There is another model, namely, coordination bonding model, which is developed in the local environmental spirit and throws light on the role of co-ordination in the interesting variations of magnetic moments. According to this model, suppression of host magnetization in a transition metal alloy $T_{1-x}M_x$ depends upon how strongly M is bonded with T and the extent of p-d bonding is assumed to be proportional to the number of T atoms surrounding an M atom. Hence, the magnitude of the average magnetic moment μ per T atom in the alloy is suppressed below that in the pure host n_B by an amount proportional to Z^T_M, the T co-ordination about the metal alloy as:

$$\mu_T = n_B [1 - Z^T_M N_M /5N_T] , \qquad (1.11)$$

where N_M/N_T is the ratio of the number of M and T atoms. This model is applicable to metallic glasses as well as crystalline solid solutions based on strongly magnetic host like iron, cobalt, and nickel.

However, Jaccarino and Walker[33] explained the magnetic moment variation in a large number of dilute alloys by a simple phenomenological model based on local environment effect. In this model the influence of very distant neighbors are neglected which are assumed to be unimportant by the damping of "magnetic interactions" by the finite electron mean free path. The variation in the saturation magnetization in binary NiMn, NiCu, and NiRh alloys can be described well by this model.

1.5.2 Exchange interaction

The exchange energy can only alter the alignment of the moments if the reduction in energy due to exchange is greater than the energy difference between the lowest available spin-up state and the highest occupied spin-down state. In other words, the system of spins will always configure itself to the lowest possible energy state, taking the exchange energy into account. If the exchange energy is present but not large enough to alter the ground state in this way then no net magnetic moment will arise.

The exchange field gives an approximate representation of the quantum mechanical exchange interaction. The energy resulting from the exchange interaction, U, is usually represented by the Heisenberg model[34] as

$$U = -2J_{ex}\vec{S}_i.\vec{S}_j \quad , \qquad (1.12)$$

where J_{ex} is the exchange integral related to the overlap of the charge distributions of the atoms i,j. $\mathbf{S_i}$ and $\mathbf{S_j}$ are the electron spins of the atomic sites i, j .

$J_{ex} > 0$ indicates a ferromagnetic interaction (favouring ↑↑ alignment).

$J_{ex} < 0$ indicates an antiferromagnetic interaction (favouring ↑↓ alignment).

So when $J_{ex} > 0$, then we have a tendency to parallel alignment which minimizes the exchange energy and leads to ferromagnetism, but this can only occur if

$$|U| \geq \Delta E,$$

where ΔE is the energy difference between the lowest available spin-up state and the highest occupied spin-down state. This condition simply ensures that any change in orientation of electronic magnetic moment causes a reduction in the total energy of the system.

1.5.3 Anisotropy energy

Experimental study of ferromagnetic single crystals show that the magnetic field required to magnetize them depends on crystallographic directions. The difference in magnetic energy to produce saturation along easy and hard directions is called the magnetocrystalline or anisotropy energy. The anisotropy field H_a is defined as the field needed to saturate the magnetization along

the hard direction. The magnetic anisotropy energy E is defined as the work required to rotate the magnetization from the easy axis to the hard axis with an applied magnetic field and is given by

$$E = K_u \sin^2\theta - \mu_0 M_s H \cos(\pi/2 - \theta) \qquad (1.13)$$

Minimizing E, $\partial E/\partial\theta = 0$ and setting $\theta = \pi/2$, $H_a = 2K_u/\mu_0 M_s$, K_u is anisotropy constant which is material specific constant.

Since $\mu_0 M_s \approx 1$ T for a typical ferromagnet, H_a can range from < 2 kAm^{-1} to more than 20 MAm^{-1}, with typical values of shape anisotropy of 200 kAm^{-1}.

For a cubic crystal, the anisotropy energy can be expressed as

$$E_{ani} = K_1(\alpha^2\beta^2+\beta^2\gamma^2+\gamma^2\alpha^2) + K_2\alpha^2 \qquad (1.14)$$

where K_1 and K_2 are anisotropy constants and α,β,γ are the direction cosines of the magnetization vector with respect to cubic axes. The exchange energy, magnetic field energy, and anisotropy energy are the main determinants of the domain characteristics. The size of the domain is determined by a balance between the exchange energy and the magnetic field energy. On the other hand, the thickness of the domain wall is determined by a balance between the exchange energy and the anisotropy energy.

1.5.4 Extraordinary Hall coefficient and the Split-Band (SB) model

Hall effect in magnetic materials is commonly described by the equation:

$$\rho_H = \mu_0 R_0 B + \mu_0 R_S M_S \quad \text{(SI units)}, \qquad (1.15)$$

where ρ_H is the Hall resistivity, B is the magnetic induction along the z-axis. R_0, the ordinary Hall coefficient, is related to the Lorentz force acting on the moving charge carriers. R_S, the extraordinary or the anomalous Hall coefficient, is associated with a left-right asymmetry in the differential scattering cross-section about the x-y plane due to the spin-orbit interaction present in a ferromognet. The extraordinary Hall coefficient, R_S, changes sign for the same electron-to-atom ratio in Ni-Fe and Ni-Co alloys which is associated with the Fermi level crossing some degeneracy in the Ni-band[35]. These are satisfactorily discussed in terms of the split-band (SB) model[36] where all the three constituents have distinctly separate sub-bands. Figure 1.4 is the band picture suggested by the SB model.

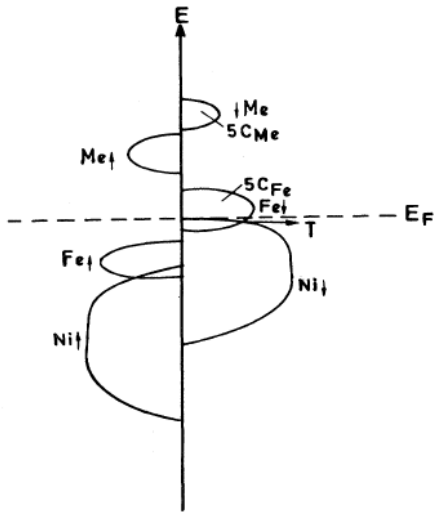

Fig.1.4 The schematic density of states for ternary Ni-Fe-M (M = Cr, V, etc.) alloys according to the SB model.

From Fig. 1.4 it can be seen that the bands of Ni are at the bottom while that of M are split from the host and are at the top due to large valence difference between Ni and M. The sign change of R_S is associated with Fermi level (E_F) crossing the point where the spin-down sub-bands for Fe and Ni meet.

As the total number of states in a 3d sub-band is 5 times the concentration of the corresponding atoms, the Fermi level crossover will take place when the total number of holes in the ternary alloy system is equal to the 5 times the concentration of Fe atoms ($5C_{Fe}$), i.e.,

$$5C_{Fe} = 0.55 + 2\,C_{Fe} - (10+Z)\,C_M \qquad (1.16)$$

Here, C is the concentration, Z is the valence difference between M and Ni (Z = - 4 for Cr) and 0.55 is the number of holes per atom in Ni.

1.6. Electron-scattering in metals and alloys

1.6.1 Electron-phonon scattering

For simple metals and alloys, one of the major contributions to the temperature dependent resistivity which originates from the lattice contribution $\rho_{L,}$ is scattering of conduction electrons

by lattice vibrations (i.e., phonons). This temperature dependent part is well described by the Bloch-Grüneissen (BG) function, $f\,(T/\theta_D)$,

$$\rho_L(T) = \alpha_{el=ph} f\left(T/\theta_D\right),$$

$$\rho\ (\frac{T}{\theta_D}) = A\left(\frac{T}{\theta_D}\right)^n \int_0^{\frac{\theta_D}{T}} \frac{z^n dz}{(e^z - 1)(1 - e^{-z})}, \qquad (1.17)$$

where A is a constant and θ_D is the Debye temperature. This is known as the Bloch -Grüneissen relation which, on simplification, gives

$$\rho_{phonon}(T) = BT^n \qquad T < \theta_D$$

$$= CT \qquad T > \theta_D \qquad (1.18)$$

n = 3 (Bloch–Wilson) for magnetic metals and alloys with large *d*-band density of states giving rise to electron–phonon scattering involving $s - d$ transitions. The single band ($s - s$) electron–phonon scattering is described well with n = 5 (Bloch –Grűneissen) in simple metals and alloys.

1.6.2 Spin-disorder scattering

Studies of spin-disorder resistivity provide important information on magnetic short range order in ferromagnets and it is an intrinsic thermodynamic feature of spin disorder. Spin disorder intermixes the spin channels and thereby introduces finite spin diffusion length in ferromagnets. In these metals the resistivity has an "anomalous" contribution which contains signatures of magnetic phase transitions. This magnetic contribution ρ_{mag} may be extracted from the measured resistivity assuming that Matthiessen's rule is valid, and that the anomalous contribution is temperature independent well above the Curie temperature[37]. The anomalous resistivity ρ_{mag} may be attributed to spin disorder scattering, which has been studied using the *s-d* model Hamiltonian[38]. This approach assumes that 3*d* electrons in transition metals are localized at atomic sites while the conductivity is due to mobile 4*s* electrons forming an itinerant band and coupled to the *d* electrons by exchange interaction. At finite temperatures, the directions of the *d*-electron spins fluctuate, and the conducting *s* electrons scatter from the fluctuating exchange

potential. As the temperature is increased toward the Curie temperature $T_{C,}$ the spins become more disordered, and ρ_{mag} quickly increases, sometimes surpassing the phonon contribution. At elevated temperatures the *s-d* model calculations of ρ_{mag} were done using the mean-field approximation. In this approximation, the spins are completely disordered above T_C, and hence ρ_{mag} is constant. In the Born approximation below T_C it decreases as

$$\rho_{mag}(T) = \rho_{mag}(T_C)[1-M^2(T)/M^2(0)], \qquad (1.19)$$

where $M(T)$ is the magnetization at temperature T[39] .

In general, ρ_{mag} is sensitive to magnetic short-range rather than long-range order[40].

1.6.3 Kondo spin-flip model

Anderson[41] showed how a transition metal impurity can either retain or lose its local magnetic moment when dissolved in a metal. Kondo[42] first realised the complexity of the behavior when the local moment is retained. The relevant part of the Hamiltonian is

$$H_{Kondo} = -\sum_{i,l} J(\vec{r}_i - \vec{R}_l)\vec{\sigma}_i.\vec{S}_l \quad , \qquad (1.20)$$

where the i^{th} electron of spin $\boldsymbol{\sigma_i}$ has a spin-flipping interaction with the l^{th} magnetic impurity with spin $\mathbf{S}_l$. Perturbation theory for spin-flipping interactions differs from ordinary potential scattering from non-magnetic impurities in having a time dependent impurity spin. For any time-dependent perturbation in a metal, the sharpness of the Fermi distribution causes logarithmic singularities in integrals. These diminish with T at least as fast as log (ε_F/k_BT) because of blurring of the Fermi distribution. An exact solution was found by Wilson[43] using the renormalization group, and by Andrei[44] using the Bethe Ansatz. These solutions were given a physical interpretation by Nozieres[45]. In particular, advanced experimental tools applied to nanosystems permit more detailed exploration[46]. Finite biases in tunnel junctions allow the ‘‘Kondo resonance’’ to be explored by inelastic spectroscopy[47].

1.6.4 Weak localization and quantum interference effects

A huge range of fascinating low T transport effects goes under the various names ‘‘weak localization’’, or ‘‘mesoscopic fluctuations’’, or ‘‘interaction effects’’ or ‘‘quantum corrections.’’ These effects show up as small corrections when electrical resistivities are large, but can be more significant when samples are small, especially in lower dimensions, d = 1 or 2. Quantum coherence is not just a property of well-organized propagating Bloch states where coherence is easily predictable. All solutions of *t*-independent Schrödinger equations are coherent. Components of a wave function interfere with other components of a superposition state. The coherence is only destroyed by t-dependent environmental perturbations such as scattering by phonons. Let $\hbar/\tau_{inel}$ be the lifetime broadening of a single particle state caused by an environmental inelastic process. At low T, the scattering rate gets very small. Electrons therefore remain coherent for a long time, and may diffuse coherently over distances $L_{coh} = \sqrt{D\tau_{inel}}$, where the diffusion constant D is determined by elastic processes. In weakly disordered materials, $D \approx \hbar/4eH_i\tau_{elast,}$ H_i being the elastic field while in strongly disordered systems the diffusion constant is a^2/τ_{hop} where τ_{hop} is the time to hop to a nearest neighbor a distance ‘a’ away. This time is of order $\hbar/W$, where *W is* the band width. When the sample is smaller than L_{coh}, large ‘‘mesoscopic’’ fluctuations could be expected. The same wave function coherence is required for a single particle state to become Anderson-localized. This is why quantum coherency corrections are called ‘‘weak localization’’ even though the system may be very far from true localization. Electron–electron Coulomb interactions also become enhanced at low *T* by the effects of disorder. For perfect Bloch states, Coulomb interactions are suppressed by Fermi degeneracy, $\hbar/\tau_C \approx \varepsilon_F (k_BT/\varepsilon_F)^2$. However, if the propagation is diffusive, two electron states, close enough to interact with each other, see the same pattern of disorder and tend to propagate similarly, giving an enhancement of the Coulomb interaction. When samples are fairly clean, the corrections to ballistic propagation are weak and perturbative theories predict leading corrections[48]. These theories go beyond conventional Fermi liquid theory and have been confirmed in numerous experimental tests.

In highly disordered systems in which the electron mean free path is of the order of lattice spacing, motion of electrons at low temperatures is diffusive rather than ballistic and this realization has prompted many workers to propose quantum corrections to the normal Boltzmann conductivity, arising from enhanced electron-electron interaction (EEI) effects and quantum interference or weak localization (WL) effects. The conduction electrons in disordered systems with high values of resistivity undergo more frequent collisions than in crystalline systems. Such an increased scattering reduces the effective electronic screening and thus enhances the electron-electron interactions The enhanced electron-electron interaction gives rise to an additional contribution to conductivity, which can be expressed as[49]

$$\Delta\sigma_{EEI}(T) = [\sigma(T) - \sigma(0)]_{EEI} = \frac{e^2}{4\pi^2\eta}\left(\frac{1.294}{\sqrt{2}}\right)\left(\frac{4}{3} - \frac{3}{2}\tilde{F}_\sigma\right)\left(\frac{k_B T}{\eta D}\right)^{1/2} \quad (1.21)$$

$$\text{where,} \quad \tilde{F}_\sigma = \frac{32}{3F}\left[(1+\frac{1}{2}F)^{3/2} - \frac{3}{4}F - 1\right] \quad (1.22)$$

where F is the average static screened Coulomb interaction potential over the Fermi surface and D is the diffusion constant. The above equation is rewritten in the following form representing the EEI contribution to resistivity

$$\frac{\rho_{EEI}(T)}{\rho_{EEI}(0)} = 1 - \rho_{EEI}(0)\left(\frac{1.294}{\sqrt{2}}\right)\left(\frac{4}{3} - \frac{3}{2}\tilde{F}_\sigma\right)\left(\frac{k_B T}{\eta D}\right)^{1/2} \quad (1.23)$$

The contribution of electron-electron interaction to total resistivity is thus proportional to $\sqrt{T}$. It turns out that the effect of this Coulomb anomaly is an additional contribution to the resistivity, which varies as $-T^{1/2}$ at low temperatures.

1.7 Magnetoresistance

Magnetoresistance, the change of a material's resistivity with the application of a magnetic field, is a well known phenomenon. It is usually measured in two orientations, one is longitudinal mode and the other is transverse. In the longitudinal mode, the magnetic field is applied along the direction of the electric current while the field is perpendicular in the transverse mode. Classically, the MR effect depends on both the strength of the magnetic field and the relative direction of the magnetic field with respect to the current. Several distinct types

of magnetoresistance are found: ordinary magnetoresistance (OMR), anisotropic magnetoresistance (AMR), giant magnetoresistance (GMR), tunnel magnetoresistance, and colossal magnetoresistance (CMR). The materials and mechanisms for these five types are distinctly different.

Magnetoresistance in ferromagnets (AMR)

The discovery of anisotropic magnetoresistance in ferromagnetic metals was made by William Thomson[50]. In ferromagnetic materials, due to the presence of spontaneous magnetization, magnetoresistance in both longitudinal (LMR) and transverse (TMR) orientations are quite different from the normal magnetoresistance. In general, at low applied magnetic fields, longitudinal (LMR) and the transverse magnetoresistance (TMR) are positive and negative, respectively. At higher fields, they show only a small decrease with field, called the technical saturation. This negative magnetoresistance (i.e., $\frac{1}{\rho}\frac{d\rho}{dH}$) beyond technical saturation could be understood from the localized model and is the characteristics of ferromagnets.

According to this model, the magnetoresistance is proportional to $(M_s(H,T)^2 - M_s(0)^2)$, $M_s(0)$ being the spontaneous magnetization. The negative slope in magnetoresistance arises when the value of magnetization ($M_s(H,T)$) dominates over the spontaneous one ($M_s(0)$) with increasing magnetic field. However, at very low temperatures ($T<<T_C$), this slope disappears since $M_s(T) \approx M_s(0)$. According to the domain theory[51,52], the zero- field magnetoresistance, for isotropic distribution of domains, is written as

$$\rho = (1/3)\rho_{\|s} + (2/3)\rho_{\perp s}, \qquad (1.24)$$

where

$$\frac{\rho_{\|s} - \rho}{\rho_{\perp s} - \rho} = \frac{\Delta\rho_{\|s}}{\Delta\rho_{\perp s}} = -2. \qquad (1.25)$$

The ferromagnetic anisotropy of resistivity (FAR) is defined as

$$FAR = \frac{\Delta\rho_{\|s} - \Delta\rho_{\perp s}}{\rho}, \qquad (1.26)$$

here the values of $\Delta\rho_{\|s}/\rho$ and $\Delta\rho_{\perp s}/\rho$ are obtained from the high-field LMR and TMR data extrapolated to zero internal magnetic field (H_{int}) and this internal field H_{int} is defined as $H_{int} = H_{ext} - \beta M_s$ where β is the demagnetization factor. This factor depends on the dimensions of the sample and its orientation with respect to the applied field. It is interesting to note that the FAR is independent of the zero-field resistivity and is an inherent property of ferromagnetic materials. The origin of FAR is generally attributed to the spin-orbit interaction present in a ferromagnet.

1.8 Summary and Outline of the Thesis

This thesis will describe our studies on the magnetic and transport properties of disordered binary (Ni-Mn) and ternary (Ni-Fe-Cr) alloys as a function of temperature, magnetic field, and composition. Our study clearly shows that the magnetic moment of Ni-Mn and NiFeCr alloys depends sensitively on the concentration and local chemical environment. We present experimental results for the Curie temperature, magnetization, and paramagnetic susceptibility of disordered states. The interplay between magnetic and transport properties in magnetic materials have been utilized in several electronic applications from the memory element to magnetic field sensors and is still a subject of extended basic research. Sometimes these could be used as corrosion resistant materials. The behavior of the alloys strongly depends on the exchange interaction between the neighboring atoms. The application of magnetic fields and temperature as external control parameters shows different magnetic phases. The high-field magnetization and magnetoresistance measurements indicate an intimate relationship between their transport and magnetic properties. These magnetic alloys with competing exchange interactions exhibit long-range order as well as spin-glass-like ordering depending upon the concentration of the non-magnetic component present. They show double transitions (PM→FM→RSG) below certain critical concentration which might be important for application potentials. The main purpose of our investigation is to study the interplay between atomic ordering and magnetic behavior, both theoretically and experimentally, by determining the magnetic transition in the alloys with different degrees of short and long range order. In this work we report a detailed determination of chemical and magnetic phase diagram in a wide temperature-composition

range. Furthermore, we also show that the experimental results can be accurately explained by a simple model Hamiltonian, solved by using the density functional based first-principles theoretical approximation that includes chemical and magnetic interactions. In both alloy systems there are ferromagnetic and antiferromagnetic concentration region in which only magnetic short-range order (MSRO) develops. Though they are well studied in the low concentration spin-glass regime, the high concentration range up to the long range ordered state, and concentrations near and around the critical concentration have their own glories and difficulties. As the system proceeds toward long-range order, it goes through a state which tries to retain the signatures of spin-glass, while some manifestation of long-range order is also evident. Hence the phenomenon of the coexistence of different magnetic phases and double transitions show up.

Bibliography

1. Clarence C. Zener, Trans. AIME **203**, 619 (1955).

2. W. H. Meiklejohn and C. P. Bean, Phys. Rev. **102**, 1413 (1956).

3. P. A. Beck, J. Less-Common Metals **28**, 193 (1972).

4. E. P. Wohlfarth, Physica **86-88B**, 852 (1977).

5. L. Neel, Adv. Phys. **4**, 191 (1955).

6. J. L. Tholence and R. Tournier, J. de Physique **35**, C4-229 (1974)

7. J. L. Tholence and R. Tournier, Physica **86-88B**, 873 (1977).

8. J. A. Mydosh and G. J. Nieuwenhuys, in *Ferromagnetic Materials*, Vol. 1, edited by E.P. Wohlfarth (North-Holland, Amsterdam, 1980), p.71.

9. A. P. Murani, S. Roth, P. Radhakrishna, B. D. Rainford, B. R. Coles, K. Ibel, G. Goeltz, and F. Mezei, J. Phys. F: Metal Phys. **6**, 425 (1976).

10. P. W. Anderson, in *Ill-Condensed Matter*, edited by R. Balian, R. Maynard, and G. Toulouse (North-Holland, Amsterdam, 1979), p.159.

11. J. A. Mydosh, *Spin Glasses: An Experimental Introduction* (Taylor and Francis Inc., 1993).

12. S. F. Edwards and P. W. Anderson, J. Phys. F: Metal Phys. **5**, 965 (1975).

13. H. C. L. Annu, Rev. Condens. Matter Phys. 1, 179 (2010).

14. T. E. Saunders and J. T. Chalker, Phys. Rev. Lett. **98**, 157201 (2007).

15. A. Andreanov, J. T. Chalker, T. E. Saunders, and D. Sherrington, Phys. Rev. B **81**, 014406 (2010).

16. G. Toulouse, Commun. Phys. **2**, 115 (1977).

17. J. A. Mydosh, J. Mag. Mag. Mater. **7**, 237 (1978).

18. D. J. Dunlop, Rev. Geophys. Space Phys. **11**, 855 (1973).

19. R. Street and J. C. Woolley, Proc. Phys. Soc. London, A **62**, 562 (1949).

20. R.V. Chamberlin and D. N. Haines, Phys. Rev. Lett. **65,** 2197(1990).

21. R. J. Borg and T. A. Kitchens, J. Appl. Chem. Solids **34**, 1323(1973).

22. J. D. Gunton, M. Sam Miguel, and P. S. Sahui, in Phase Transitions and Critical Phenomenon, Eds. C. Domb and J. L. Lebowitz (Academic Press, New York, 1983) Vol. 8.

23. P. C. Hohenberg and B. I. Halperin, Rev. Mod. Phys. **49**, 435 (1977).

24. J. P. Chen, C. M. Sorensen, K. J. Klabunde, G. C. Hadjipanayis, E. Devlin, and A. Kostikas, Phys. Rev. B, 54, 9288 (1996).

25. A. H. Morrish, K. Haneda, and P. J. Schiurer, J. Physique Coll. **C6**, 301(1976).

26. Q. A. Pankhurst and R. J. Pollard, Phys. Rev. Lett. 67, 248 (1991).

27. F. T. Parker and A. E. Berkowitz, Phys. Rev. B 44, 7437 (1991).

28. T. Sato, Y. Miyako, J. Phys. Soc. Japan **51,**1394(1982).

29. M. Suzuki, Progr. Theor. Phys. **58** (1977) 1151.

30. S. Goudsmit and G. E. Uhlenbeck, Nature 117, 264, (1926).

31. F. E. Luborsky, Ferromagnetism Vol. I, Ed. E. P. Wohlfarth (North Holland, Amsterdam, 1980) p. 451.

32. R. C. O'Handley, J. Appl. Phys. **62**, R15 (1987).

33. V. Jaccarino and L. R. Walker, Phys. Rev. Lett. **15,** 259 (1965).

34. W. Heisenberg, Z. Physik **49**, 619 (1928).

35. L. Berger, Physica **30**, 1141(1964).

36. H. Ashworth, D. Sengupta, G. Schnakenberg, L. Shapiro, and L. Berger, Phys. Rev. **185**, 792 (1969).

37. R. J. Weiss and A. S. Marotta, J. Phys. Chem. Solids **9**, 302 (1959).

38. P. G. de Gennes and J. Friedel, J. Phys. Chem. Solids **4**, 71 (1958).

39. I. Mannari, Prog. Theor. Phys. **26**, 51 (1961).

40. M. E. Fisher and J. S. Langer, Phys. Rev. Lett. **20**, 667 (1968).

41. P. W. Anderson, Phys. Rev. **124**, 41 (1961).

42. J. Kondo, Progr. Theoret. Phys. (Kyoto) **32**, 37 (1964).

43. K. G. Wilson, Rev. Mod. Phys. **47**, 773 (1975).

44. N. Andrei, K. Furiya, and J.H. Lowenstein, Rev. Mod. Phys. **55**, 331 (1983).

45. P. Nozieres, J. Low. Temp. Phys. **17**, 31 (1974).

46. K. Nagaoka, T. Jamneala, M. Grobis, and M.F. Crommie, Phys. Rev. Lett. **88**, 077205 (2002).

47. D. Goldhaber-Gordon, H. Shtrikman, D. Mahalu, D. Ambusch-Magder, U. Meirav, and M.A. Kastner, Kondo effect in a single-electron transistor, Nature 391, 156 (1998).

48. B. L. Altschuler and P. A. Lee, Physics Today 41, 36 (1988).

49. B. L. Altschuler and A. G. Aronov, *"Electron-Electron Interactions in Disordered Systems"* edited by F. L. Efros and M. Pollak, Elsevier, New York (1985).

50. W. Thomson, Proc. Roy. SOC., vol. 8, pp. 546-550, (1857).

51. R. M. Bozorth, "Phys, Rev. vol. 70, 923(1946).

52 G. F. Koster : Solid State Physics, eds. F. Seitz and D. Turnbull, (Academic Press, New York, 1957) vol. 5, p. 173.

CHAPTER II

Sample Preparation and Experimental Details

2.1 Preamble

In this chapter, a brief overview of the sample preparation and their characterization as well as various experimental set-ups are discussed which were used during this thesis work. The magnetic and the transport property measurements were done using Quantum Design's Magnetic Property Measurement System (MPMS) along with Lake Shore's Vibrating Sample Magnetometer (VSM) and Quantum Design's Physical Property Measurement System (PPMS) respectively. The structural and phase characterizations of the samples are done using SEM, EDXA, and XRD.

2.2 Sample Preparation

Samples of both Ni-Mn (six samples) and Ni-Fe-Cr (seven samples) alloy series are prepared by arc melting, in pure argon atmosphere, of required amount of 99.999 % spectroscopically pure constituent elements, obtained from Johnson–Mathey, Inc. (England). The elements are cleaned with organic solvent and etched with dilute HNO_3. For NiMn series, we have taken a little more Mn than that required anticipating some Mn loss due to evaporation.

The melting is performed in a water-cooled coil type induction furnace, with a maximum power of 7 kW, fed by an "Ajax Magnethermic Converter" which converts line current of 50 Hz to a value between 20 to 40 kHz. The elements are taken in a high quality alumina crucible which is placed in a graphite susceptor and the whole thing is put in a vacuum-sealed quartz tube. This zone was repeatedly evacuated to 10^{-3} torr and flushed with high purity argon gas. Finally, this quartz tube is filled with argon gas at less than atmospheric pressure. During heating process the temperature is monitored with an optical pyrometer. The furnace is switched off as soon as the melting of the constituents is completed. The alloy ingot thus prepared is subjected to a homogenization process. The ingot is put in a quartz capsule which is then repeatedly evacuated and flushed with argon gas and finally sealed in a partial pressure of argon. The

capsule is then heated for 3 days in a vertical furnace at a temperature which is roughly 100^{o}C less than the melting point of the alloy, decided from the phase diagram. The alloy is then dropped in a bucket full of brine to quench it to room temperature. Then the alloy ingot is swaged, cold-rolled and cut into various shapes for different measurements. The sample pieces are then sealed in quartz tubes in argon atmosphere and heated for a day in a vertical furnace at temperatures close to their melting points and then fast quenched in brine. This heat treatment is very important since this process helps in preserving both the high temperature crystallographic phase (γ- phase) and the random substitutional nature of the polycrystalline samples and preventing any possible chemical clustering. The quenching process has to be done as fast as possible as slow quenching can introduce other lower temperature crystallographic phases.

2.3 Characterization techniques

2.3.1 Superconducting Quantum Interference Device (SQUID)

One of the most sensitive forms of magnetometry is SQUID magnetometry. The technique of combination of superconducting material and Josephson junction is being used here. Most of the magnetic measurements of our Ni-Mn and Ni-Fe-Cr alloys were carried out using Quantum Design's Magnetic Property Measurement System (MPMS) magnetometer which is basically a Superconducting Quantum Interference Device (SQUID) magnetometer. A SQUID magnetometer consists of a superconducting ring containing one or more Josephson junctions. A brief description[1] of the superconducting ring with two junctions is given below as shown in Fig. 2.1.

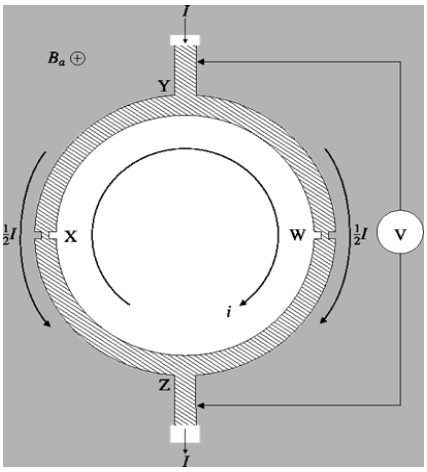

Fig.2.1 Superconducting quantum interference device (SQUID) as a simple magnetometer.

If a current I is passed through this circuit, current I/2 flows through each junction. Now if a magnetic field of gradually increasing flux density B is applied perpendicular to the plane of the ring then a circular current i is induced within the ring. This means that currents i+(I/2) and i-(I/2) flow through the right-junction and the left-junction of the ring, respectively. The phase change of an electron around any closed superconducting circuit is $2\pi n$, where n is an integer. An applied magnetic field produces a phase change around a ring, which in this case is equal to

$$\Delta\varphi(B) = 2\pi\,(\varphi_a/\varphi_0) \qquad (2.1)$$

where φ_a is the flux produced in the ring by the applied magnetic field. The magnitude of the critical measuring current is dependent upon the critical current of the weak-links and the limit of the phase change around the ring being an integral multiple of 2π. For the whole ring to be superconducting, the following condition must be met:

$$\alpha + \beta + 2\pi(\varphi_a/\varphi_0) = 2\pi n, \qquad (2.2)$$

where α and β are the phase changes produced by the currents across the weak-links. Here, φ_a is the magnetic flux passing through the ring and φ_0 is the quantum of magnetic flux (= h/2e = 2.0678×10^{-15} T m^2).

In the absence of any measuring current, $\alpha = \beta = \pi\,[n-(\varphi_a/\varphi_0)]$.

When the measuring current I is applied, $\alpha \neq \beta$. Since $\alpha + \beta$ = constant, the phase changes can be written as

$$\alpha = \pi\,[n-(\varphi_a/\varphi_0)] - \delta \qquad (2.3)$$

$$\text{and } \beta = \pi\,[n-(\varphi_a/\varphi_0)] + \delta \qquad (2.4)$$

where δ is related to the magnitude of the measuring current I.

Using the relation between current and phase: $i \pm I/2 = i_c \sin\{\pi\,[n-(\varphi_a/\varphi_0)] \pm \delta\}$ (2.5)

we obtain, $I = 2i_c \cos\{\pi\,[n-(\varphi_a/\varphi_0)]\}\ \sin\delta$. (2.6)

As $\sin\delta \leq 1$, $I \leq 2i_c \cos|\pi(\varphi_a/\varphi_0)|$. (2.7)

The critical measuring current is $I_c = 2\ i_c \cos|\pi(\varphi_a/\varphi_0)|$ which is an oscillating function with a period of φ_0 and whenever the magnetic flux φ_a becomes a multiple of φ_0 there is a maximum. Hence, the magnetic flux passing through the ring can be measured as multiples of φ_0. The measurement of such a digitized quantity can be made very accurately, particularly since the magnitude of φ_0 is extremely small which helps us to measure very weak magnetic field[2].

This SQUID magnetometer does not directly detect the magnetic field created due to the sample. A measurement is performed by moving a sample through the superconducting detection coils which are located at the center of the magnet provided with a constant dc magnetic field required during measurements. The sample moves along the symmetry axis of the detection coil and the magnet. Moving sample induces an electric current in the detection coils which are connected to the SQUID input coil with superconducting wires, allowing the current from the detection coils to inductively couple to the SQUID sensor. The detection coil is basically a second-order-gradiometer detection coil. It is a single piece of superconducting wire wound in a set of three coils. In this configuration, the upper coil is a single turn wound

clockwise, the center coil comprises two turns wound counter-clockwise, and bottom coil is a single turn wound clockwise.

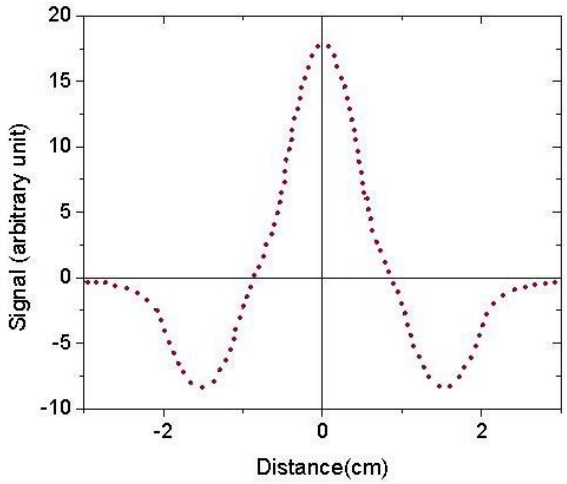

Fig.2.2 Sample position in SQUID detection coil and the corresponding signal.

Figure 2.2 shows the calculated output (in arbitrary units) of the SQUID electronics as a function of sample position. The x-axis shows the sample position, when x = 0, the sample is at the center of the detection coils. In this figure the single turn upper and bottom coils are ± 1.5 cm from the central coil. For our magnetic measurements, we have used straw packing to fit the sample in the sample holding straw. Quantum Design provides two standard transport options to be used with the MPMS. The DC transport and RSO transport. The RSO transport is primarily used for samples with small magnetic moments.

2.3.2 Vibrating Sample Magnetometer (VSM)

Vibrating sample magnetometer (VSM) is based on Faraday's law that states, an emf (electromotive force) 'V' will be generated in a coil if there is a change in magnetic flux, Φ linking the coil. The induced emf in a coil with 'n' turns with a cross-sectional area of 'a' can be written as

$$V = -n\,a\,(dB/dt). \qquad (2.8)$$

When the coil is positioned in a constant magnetic field 'H',

$$B = \mu_0 H, \qquad (2.9)$$

where μ_0 is permeability of vacuum. Now if we place a magnetic sample having magnetization 'M' near the coil, then

$$B = \mu_0 (H + M). \qquad (2.10)$$

The corresponding change in B due to the magnetic sample can be written as

$$\Delta B = \mu_0 M. \qquad (2.11)$$

The induced emf in the pick-up coils can therefore be expressed as

$$Vdt = -na\mu_0 M. \qquad (2.12)$$

The above equation implies that the output signal of the coil is proportional to the magnetization M but independent of the magnetic field in which the magnitude of M is to be determined. Schematic diagram of a VSM is shown in Fig. 2.3. In a VSM, the sample is subjected to a sinusoidal motion (of frequency ν) and the corresponding voltage is induced in suitably located stationary pickup coils which generate output signal of frequency ν. Also, the intensity of the signal is proportional to the magnetic moment of the sample, the vibration amplitude, and the frequency ν. The sample to be measured is centered in the region between the poles of an electromagnet which can generate a uniform magnetic field H_0. A thin vertical non magnetic sample rod (made of plastic/quartz) connects the sample holder with a transducer assembly located above the magnet. The transducer converts a sinusoidal as drive signal (generated by an oscillator/amplifier circuit) into a sinusoidal vertical vibration of the sample rod. The sample is thus subjected to a sinusoidal motion in the magnetic field H_0.

Pickup coils made of copper and mounted on the poles of the electromagnet pick up the signal resulting from the motion of the sample. The magnetic moment readings taken simply by measuring the amplitude of the signal are subjected to errors due to the variation in amplitude and frequency of vibration of the sample. In order to avoid this difficulty, a nulling technique is introduced employing a vibrating capacitor for generating a reference signal that varies with vibration amplitude and frequency in the same manner as the signal coming from the pickup

coils. When these two signals are processed in an appropriate manner, it is possible to eliminate the effects of vibration amplitude and frequency shifts. In that case, one obtains readings that vary only with the moment of the sample.

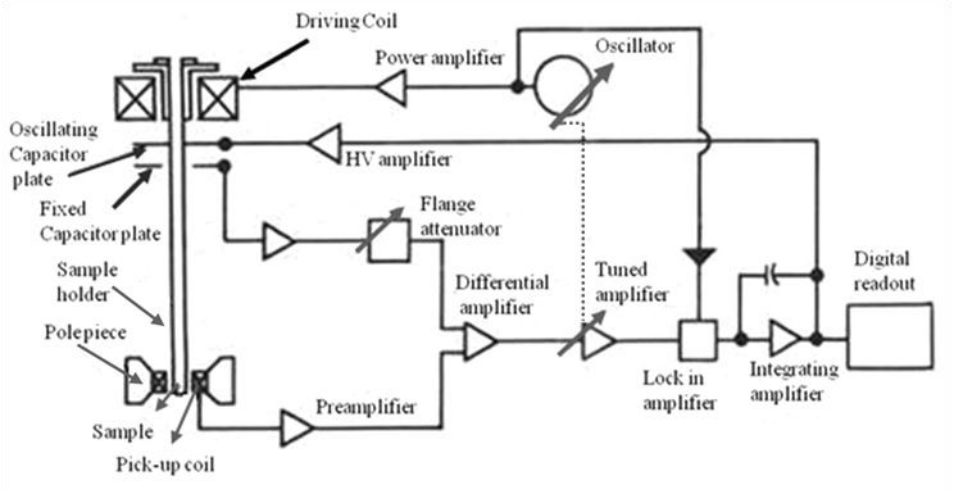

Fig. 2.3 Schematic diagram of a VSM unit.

The VSM in our laboratory (Lakeshore make) has maximum magnetic field generating capability of 2.1 T without cryogenic system and 1.76 T can be achieved with LN_2/LHe dewar between the coils. The moment versus temperature and isothermal hysteresis loops at various temperatures can be measured using a cryogenic system (Liq. N_2) that can operate within a temperature range of 80 to 400 K with temperature stability of ± 0.2 K and temperature resolution of 0.001 K. Noise level of 1.25 μemu (RMS value) in moment measurement can be achieved using the system[3].

2.3.3 Physical Property Measurement Systems (PPMS)

The electrical transport and ac susceptibility measurements were done using Quantum Design's Physical Property Measurement System (PPMS)[4]. The resistivity of the samples was

measured down to 2 K and magnetic fields up to 5 T using standard dc four-probe methods. Fig. 2.4 shows the schematic diagram of the 8 T PPMS system along with the pucks used for resistivity measurements. The system works down to 2 K in standard form and down to 300 mK with ^{3}He insert. Fields up to 8 T is achieved using hybrid NbTi and Nb_3Sn magnets. The temperature can be controlled to better than 10 mK. A 9.3 Hz square wave is used for resistivity measurements and noise reduction is done by lock-in technique and data averaging.

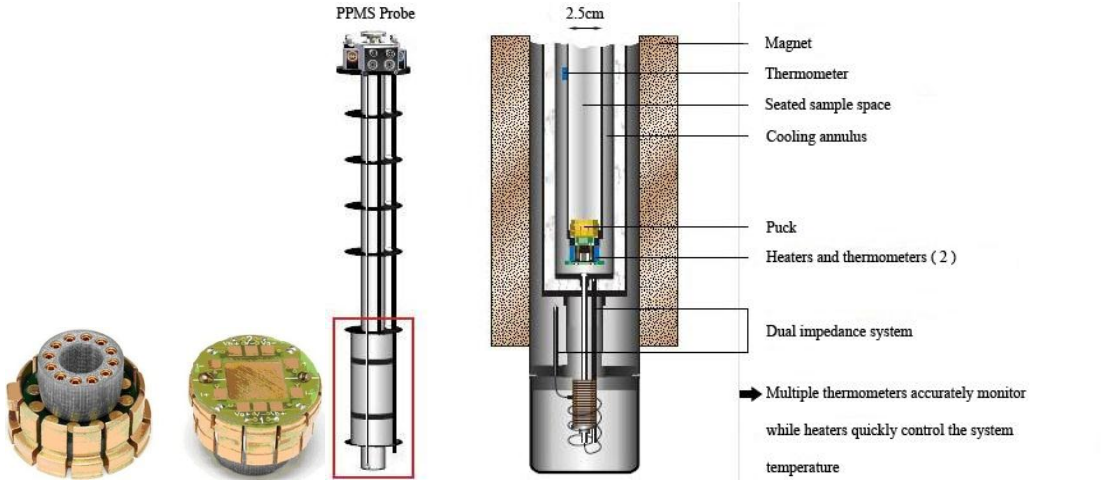

Fig.2.4 Schematic diagrams of QD-PPMS system and the photograph of pucks used for mounting samples.

The ac transport measurement system (ACT) option has a precision current source and voltage detector that support four different types of automated, electrical transport measurements: ac resistivity, five wire Hall effect, I-V curve, and critical currentS. The ac measurement systems (ACMS) provide the capability to perform both ac susceptibility and dc magnetization measurements. The sample is mounted near the center of the detection coils (approximately (10.5 ± 0.8) cm from the end of the long sample rod on the ACMS sample holder); the ACMS sample transport can automatically center it by adjusting the sample position relative to servo motor zero. The samples were pasted on the sample holder using GE varnish (good thermal conductor but bad electrical conductor). One end of the silver wires (due to softness) was soldered on the sample puck copper connectors with zinc-cadmium solder. The other end of the silver wire was connected to the sample using silver paste. After making the

contacts the samples were kept under IR lamp for drying. Indium has not been used as it becomes superconducting around 3.6 K.

2.3.4 Scanning Electron Microscope (SEM)

In an Electron Microscope a stream of electrons is formed in high vacuum (by electron guns). The stream is accelerated towards the specimen (at a positive potential) and is confined, focused and directed in a particular direction using metallic charged plates and magnetic lenses resulting in a monochromatic beam. As the beam is incident on the sample, it interacts with the atoms of the sample and which in turn affects the electron beam. These interactions and effects are detected and transformed into an image.

In SEM (Schematically shown in Fig. 2.4), the electron beam is either thermionically or field emitted from an electron gun[5] and focused in vacuum into a fine probe that is rastered (A scanning pattern of parallel lines that form the display of an image projected on a display screen) over the surface of the specimen. SEM works on a voltage between 2 to 50 kV and its beam diameter that scans the specimen is 5 nm-2 μm. A field-emission cathode in the electron gun of a SEM (FESEM) provides narrower probing beams at low as well as high electron energy.

When the electron beam interacts with the sample, the energy exchange between the electron beam and the sample results in the deceleration of incident electrons through energy dissipation and produces a variety of signals. These signals include secondary electrons (produced by inelastic scattering of incident electrons with the atoms of the sample), backscattered electrons, diffracted backscattered electrons, characteristic X-rays (produced by inelastic collisions of the incident electrons with electrons in discrete orbitals of the atoms of the sample), visible light (cathodo-luminescence), and heat. Secondary and backscattered electrons are conventionally separated according to their energies[6]. The electrons are detected by suitable detectors placed in the microscope in proper positions. The secondary electrons produce the SEM micrograph of the sample.

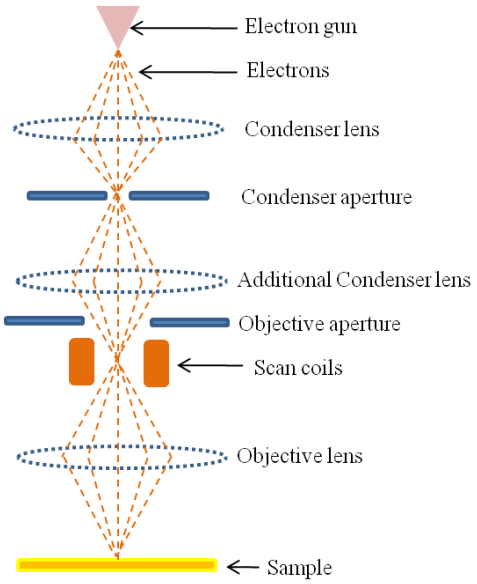

Fig. 2.5 Schematic diagram of a SEM unit.

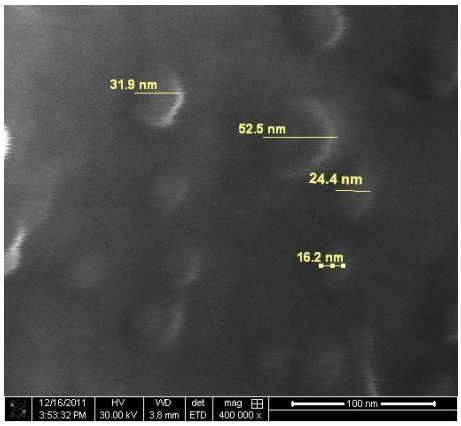

Fig. 2.6 SEM micrographs of $Ni_{75}Mn_{25}$ sample to check short range ordering.

2.3.5 Energy Dispersive X-Ray Analysis (EDXA)

When a high-energy electron beam hits a specimen, X-rays characteristic of the atoms in the specimen are generated within the region illuminated. This allows the possibility of microanalysis, that is, the chemical analysis of a small amount of material, or a small part of a larger specimen. If we can measure the energy of the X-rays (or equivalently their wavelength,

since they are related by Planck's constant, $E = hc/\lambda$ or specifically $E_{kV} = 12.4/\lambda_{Angstroms}$), then we can immediately tell qualitatively which elements are present in the part of the specimen under investigation. If we measure X-ray intensities, we also get an immediate rough idea of how much of each element is present. EDXA makes use of the X-ray spectrum emitted by a solid sample bombarded with a focused beam of electrons to obtain a localized chemical analysis. Qualitative analysis determining the concentration of elements present entails measuring line intensities for each element in the sample and for the same elements in calibration standards of known composition. X-ray intensities are measured by counting photons. As well as producing characteristic X-ray lines, the bombarding electrons also give rise to a continuous X-ray spectrum, which limits the detachability of small peaks owing to the presence of a background.

The characteristic peaks carry the compositional information[7]. They arise when the energy of the incident electrons is high enough to eject inner-shell electrons from atoms in the specimen. For example, the ejection of a K-shell electron leaves the atom in an excited state. One of the ways it can lower its potential energy is by an electron from an outer shell falling to the vacant inner-shell position and at the same time emitting an X-ray of characteristic energy (Fig. 2.7). This characteristic energy is determined by the difference in the electron energy levels of the atom and therefore can provide direct information about the chemistry of the electron beam/specimen interaction volume.

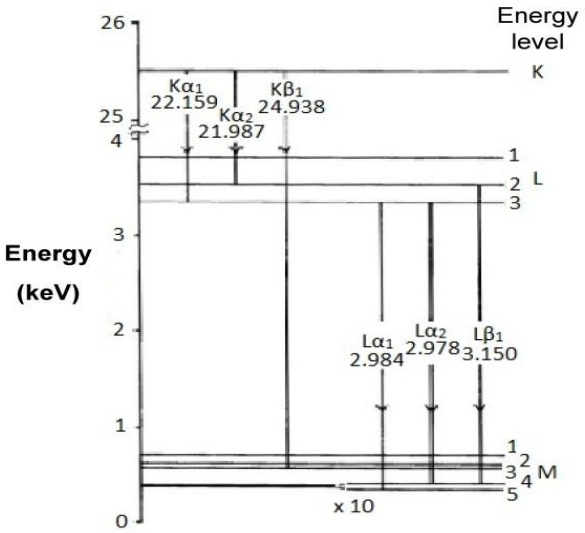

Fig. 2.7 Transitions leading to the generation of characteristic X-rays.

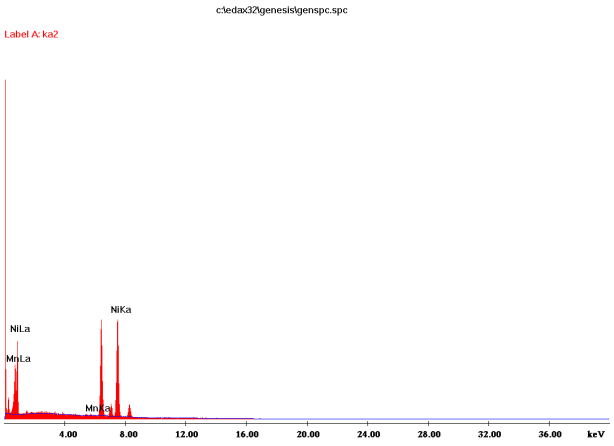

Fig. 2.8 EDXA spectra of $Ni_{63}Mn_{37}$.

EDAX ZAF Quantification (Standardless) Element Normalized

Elem	Wt %	At %	K-Ratio	Z	A	F
MnK	36.85	38.41	0.3919	0.9756	0.9878	1.1034
NiK	63.15	61.59	0.6060	1.0141	0.9464	1.0000

A typical X-ray spectrum is shown in figure 2.7. It consists of characteristic peaks superimposed on a background of "Bremsstrahlung". The width of a characteristic X-ray peak is given by the equation:

$$FWHM = [N^2 + 5.5F\ \varepsilon\ E]^{1/2} \qquad (2.13)$$

where: N = electronic noise in the system

F = Fano factor (0.11 for Si)

ε = Energy to produce an electron hole pair (3.8 eV)

E = X-ray line energy

Typical values of FWHM for modern detectors are 133 eV for Mn K_α.

2.3.6 X-ray Powder Diffraction (XRD)

X-ray crystallography relies on the dual wave/particle nature of x-rays to collect information about the crystalline structure of crystalline samples under test among which X-ray powder diffraction is the most common technique for powder samples.

The physics and mathematics describing the generation of monochromatic X-rays (an electromagnetic radiation) and the diffraction of those X-rays by crystalline powdered materials are very complex. However in short, X-rays are generated by a cathode ray tube, filtered to produce monochromatic radiation, collimated to concentrate, and directed toward the sample[8]. The X-ray we use is of K_α emission of a copper metal with an average wave length of ~ 1.5418 Å. Upon incidence on crystalline samples, atoms within the sample elastically scatter the X-ray waves, primarily through the atomic electrons. The regular array of scatterers (electrons) within a crystalline sample produces a regular array of outgoing spherical waves of scattered X-rays. Although these waves cancel one another in most directions through destructive interference, they add constructively in a few specific directions, determined by Bragg's law. These diffracted X-rays are then detected, processed, and counted. By scanning the sample through a range of 2θ angles, all possible diffraction directions of the lattice should be obtained due to the random orientation of the powdered material. Conversion of the diffraction peaks to d-spacings allows identification of the elements/compound present in the sample because each element/compound has a set of unique d-spacings. Typically, this is achieved by comparison of d-spacings with standard reference patterns (i.e., ICSD or Inorganic Crystal Structure Database).

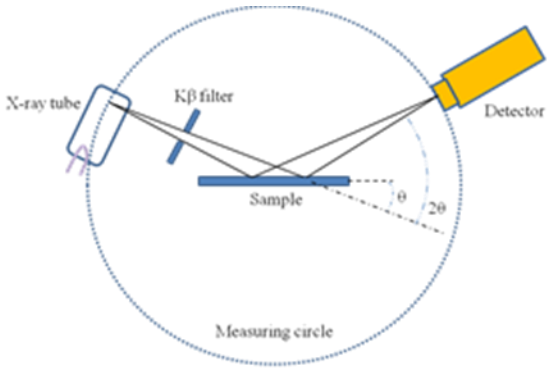

Fig. 2.9 Schematic diagram of X-ray diffraction optics used in θ/2θ mode.

Powder diffractometers come in two basic varieties: θ-θ in which the X-ray tube and detector move simultaneously or a θ-2θ in which the X-ray tube is fixed, and the specimen moves at half the rate of the detector to maintain the θ-2θ geometry. We use X-ray Panalytical (X'Pert Pro) system which has a θ-2θ system during data collection as shown in Fig. 2.9.

The angles and intensities of diffractions are recorded electronically using a detector, electronics, and specialized software resulting in a plot of 2θ (horizontal axis) vs. intensity (vertical axis) for the specimen. Fig. 2.10 shows a typical XRD pattern obtained for one of our f.c.c alloys.

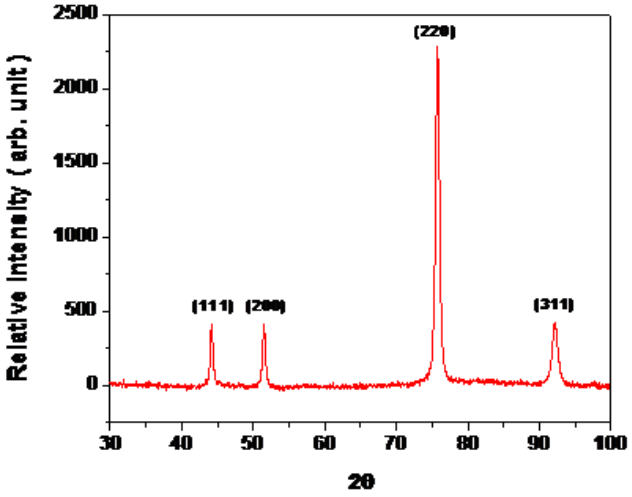

Fig. 2.10 X-ray diffraction pattern of $Ni_{79}Fe_1Cr_{20}$.

Bibliography

1. M. McElfresh, Fundamentals of Magnetism and Magnetic Measurements, Technical Resources from Quantum Design, San Diego, CA 92121-3733, USA (2000).

2. R. L. Fagaly, Review of Scientific Instruments, 2006, **77**, 101101.

3. Lake Shore Cryotronics, Inc., USA.

4. Physical Property Measurement System, Quantum Design Mannual.

5. Groves, T.R., Pfeiffer, H.C., Newman, T.H., and Hohn, F.J., J. Vac. Sci. Technol. B, **6**(6), 2028 (1988).

6. Brundle, C. R., Evans, C. A. Jr., and Wilson, S., Encyclopedia of materials characterization, Butterworth-Heinemann publications, 1992.

7. Russ, J. C. (1984) Fundamentals of Energy Dispersive X-ray Analysis, Butterworths. London.

8. Cullity, B. D. and Stock, S. R., Elements of X-ray Diffraction, 3rd Edition**,** Prentice Hall (2001).

CHAPTER III

Magnetic ordering in Ni-Mn alloys around the multicritical point: Experiment and Theory

3.1 Preamble

We have carried out an experimental study of Ni-rich Ni_{100-x} Mn_x ($15 \leq x \leq 37$) alloys in a series of compositions across the multicritical point and determined the phase diagram within that range. We have observed ferromagnetic long-range order with re-entrant spin-glass/ferro-spin-glass phase for $x \leq 25$, an antiferromagnetic long-range order around $x \sim 37$, and a gradual change from a canonical spin-glass state to a long-range antiferromagnetic phase in the intermediate composition region. In order to explain the experimental observations, we have examined the physical properties from a density functional based first-principles theoretical analysis and used it to understand the experimental results. Using atomic spin dynamics simulations based on the Landau-Lifshitz-Gilbert equation, we have found the aging behaviour and anomalously slow relaxation of magnetization in the composition range where experiments show spin-glass behaviour.

3.2 Motivation behind the work

Magnetism in $Ni_{100-x}Mn_x$ (x = Mn content in atomic %) alloys provides a classic example of a disordered system with competing interactions. Magnetic parameters, such as transition temperatures, saturation magnetization, and coercivity, for different compositions are useful in assessing their application potentials. In an earlier work, Hahn and Kneller[1] carried out magnetic

studies on Ni-Mn alloys as a function of heat treatment. They found that in spite of quenching from well above the ordering temperature, there exists small ferromagnetically ordered Ni_3Mn regions of about 20 Å in diameter in a matrix of disordered material. This made the preparation of single-phase Ni-Mn alloys a difficult task. Soon after, Kouvel and Graham[2] established the coexistence of ferromagnetism and spin-glass like state coming from competing pair exchange interactions between the components at low temperatures in disordered Ni_{100-x} Mn_x alloys with x = 20, 25, and 30, through hysteresis loop and torque measurements. Abdul-Razzaq and J. S. Kouvel[3] reported the magnetic phase diagram in the composition range $23 \leq x \leq 27$. They observed, below the multicritical point (MCP) of x = 23.9 and T = 102 K, a double transition from a paramagnetic to a ferromagnetic state at T_C followed by a spin-glass (SG) like state at $T_{fg} < T_C$ with a re-entrant character. Above x = 23.9 they found a paramagnetic to a normal SG state at T_g. Aitken *et al.*[4] found the MCP to be above x = 26. This difference could arise from the difference in atomic short-range order in the two reports. Hauser and Bernardini[5] studied sputtered films of Ni_{100-x} Mn_x alloys and their bulk counterparts. They observed paramagnetic to spin-glass transition through ac susceptibility, χ measured at 10 kHz and 4 Oe ac field. Bulk samples with x = 22, 27, and 31 gave T_g of 40, 78, 73 K (much lower than 110 K found by Aitken *et al.*[4]) and the Curie-Weiss plot ($1/\chi$ vs T) for x = 27 gave a Neel´ temperature θ = 125 K and n_{eff} of 2.5 μ_B which lies in between 0.3 and 3.2 μ_B found from neutron scattering experiments. It also gave a displaced hysteresis loop. Ferromagnetism disappeared at x = 27 since χ fell abruptly to 0.767×10^{-3} from 14.7×10^{-3} for x = 22 where $T_C \sim 290$ K and $T_g \sim 40$ K. They concluded that the presence of ferromagnetism below x = 26 is independent of preparation conditions, be they induction melted or quenched bulk alloy or sputtered films. However, the magnetic parameters such as T_C, T_g, and χ (T) varied considerably. Needless to say that a more detailed magnetic phase diagram of this interesting system is certainly necessary, especially away from the multicritical composition. In the experimental part of this paper we have investigated in detail the magnetic properties of six samples of disordered Ni_{100-x} Mn_x alloys encompassing the critical concentration (x = 25) in the composition range x = 15 – 37 at. % Mn which was the transition region from ferromagnetism to antiferromagnetism. For alloys with x = 15 and 20, with decreasing temperature, we observed a paramagnetic (PM) to a ferromagnetic (FM) transition at T_C and then below T_{fg} the occurrence of a spin-glass(SG)-like

phase. Previous theoretical studies[6] had also shown that this SG-like phase below T_{fg} has a spontaneous FM moment with the transverse spin components ordered in a spatially random manner. It has therefore been called a "mixed phase". We indeed found that the SG-like phase has a spontaneous moment and the FM to SG-like transition temperature (T_{fg}) increased while the FM Curie temperature (T_C) decreased with increasing Mn concentration. They met at x = 25 and $T \sim 100$ K, the multicritical point (MCP). For alloys with x = 30 and 35, we observe only a single transition from a paramagnetic to a spin-glass-like (or an antiferromagnetic for x = 35) phase which is different from that of the previous "re-entrant spin-glass" phase. At higher concentrations such as x = 37, a paramagnetic to an antiferromagnetic transition is noticed.

We shall interpret the above behaviour in terms of the work of Carr Jr.[7] which takes the view that for the 3d electrons a Heitler-London approximation holds and so the electrons are to be associated with the individual atoms. For Ni-Mn alloys, the dominant exchange energies are antiferromagnetic Mn-Mn and ferromagnetic Ni-Ni and Ni-Mn interactions. For low Mn concentration (x), Mn-Mn interaction is negligible and hence all the spins become parallel resulting in an increase in M falling on the right segment of the Slater-Pauling (SP) curve[8] with a slope of −1, as shown in Fig. 3.1. For slightly higher x, there is hardly any Mn—Mn nearest neighbors for the ordered alloy, such as Ni_3Mn. So, the points still continue to fall on the -1 slope line (See Ni_3Mn point on Fig. 3.1). However, for the disordered alloys at still higher x, the Mn-Mn AF interaction wins over the Ni-Mn FM interaction and Mn spins tend to cancel each other. As a result, M shows a bending over beyond which the magnetic moment comes mainly from nickel ions and decreases with increasing Mn which causes the filling up of the nickel d shell. Finally, M decreases with x following the left segment of the SP curve and ferromagnetism is lost around x ~ 30 at. % Mn. This is found in most experiments. So, our findings that in the present alloys long-range FM disappears at x = 25, is more or less justified.

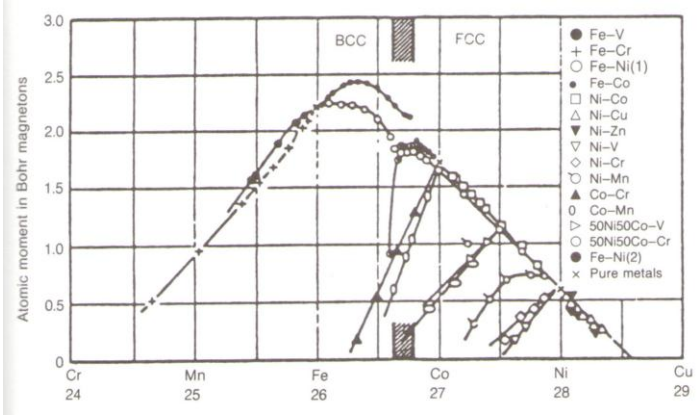

Fig. 3.1 Slater-Pauling Curve: The average atomic moment is plotted against the number of valence ($3d + 4s$) electrons.

Finally, the magnetic behaviour of Ni-Mn alloys is typical of a competing interacting system with ferromagnetic and antiferromagnetic regimes enclosing a concentration range in which only magnetic short-range order (MSRO) exists.

3.3 Experimental Procedure

The electronic configuration of Ni is [Ar] $3d^8\ 4s^2$ and that of Mn is [Ar] $3d^5\ 4s^2$. The melting points of nickel and manganese are as high as 1455 ˚C and 1245 ˚C, respectively. Hence it is difficult to make homogeneous alloys with them as constituents. Ni-Mn alloys with 15, 20, 25, 30, 35, and 37 at. % Mn were arc melted in argon atmosphere with appropriate proportions of Ni and Mn. Then the ingots were homogenized for 3 days at 1000 ˚C and small cylindrical samples were spark cut for each composition. Their sharp corners were rounded off so that the demagnetization factor is reasonably uniform. Each sample was encapsulated in a quartz tube in argon atmosphere, annealed for 3 hours at 1100 ˚C, and then quenched in water. This treatment ensured the absence of an ordered Ni_3Mn phase which is strongly ferromagnetic (T_C ~ 700 K). However, atomic short-range ordering could not be ruled out. A final annealing was done in argon atmosphere at 1000 ˚C to reduce strain introduced due to cold rolling. We performed the magnetic measurements using a vibrating sample magnetometer (VSM), a superconducting

quantum interference device magnetometer (SQUID, MPMS of Quantum Design), and a PPMS VSM of Quantum Design. The x-ray diffraction of the samples was carried out using a Philips XRD machine (X-Pert PRO Diffractometer) with a Guinier-type camera employing a focusing geometry and a solid-state detector. The radiation used was Cu $K_{\alpha 1}$. The chemical composition of the alloys was determined using standard analytical methods such as energy-dispersive x-ray analysis (EDAX).

3.4 Experimental Results and Discussions

3.4.1 Structural Properties

XRD measurements revealed that all the alloys are of single face-cantered-cubic phase. A typical XRD pattern for the $Ni_{85}Mn_{15}$ sample is shown in Fig. 3.2. Table 3.1 shows the measured lattice constants as a function of alloy composition. These lattice constants differ by only 1.4 to 2.8 % from that of pure Ni. We also note that the lattice constant increases monotonically with the increase of Mn concentration implying a good control of the alloy composition. As mentioned earlier, there are significant difficulties in forming the fully random alloy. The problem is the precipitation of a second phase of ordered $L1_2$ Ni_3Mn which is ferromagnetic with T_C ~ 700 K and lattice parameter ~ 3.60 Å as against ~ 3.57 Å for the disordered $Ni_{75}Mn_{25}$.

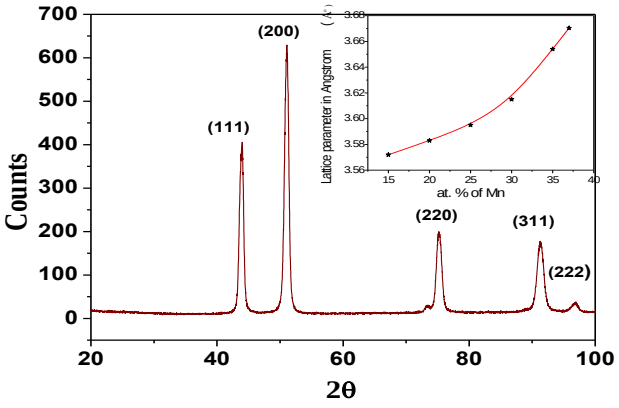

Fig. 3.2 XRD pattern of 15 % Mn alloy. The inset shows the variation of the lattice parameter with increasing Mn content (at. %).

TABLE 3.1. Alloy compositions and their lattice constants with errors.

Mn Conc. (at. %)	Lattice Parameter (Å)
15	3.572 ± 0.004
20	3.583 ± 0.007
25	3.595 ± 0.007
30	3.615 ± 0.005
35	3.654 ± 0.006
37	3.670 ± 0.004

For any disordered system, there may be some local preferences between like or unlike atoms. This is called clustering or short-range order. Cowley[9] introduced a parameter α_i which is a measure of the average number of unlike nearest neighbours throughout the crystal. We have applied the Rietveld method to analyze the x-ray diffraction data to calculate this short-range order parameter of the $Ni_{75}Mn_{25}$ sample. By definition $\alpha_i = 1 - p_i / x_A$, where p_i is the probability that the atomic site i is occupied by an A atom. The probability that we get from Rietveld analysis is 0.7373, which deviates from 0.75. Hence the value of the short-range order is given by $\alpha_i = 1 - (0.7373/0.75) = 0.0169$. Therefore the percentage of short-range order is $\sim$1.7 %. Our alloys are definitely not "fully random" but contain $\sim$ 98.3 % of disordered $Ni_{75}Mn_{25}$. The point to note here is that the observed exotic complex mixtures of magnetic phases that include short-range ordering, clustering, randomness on the nm scale, etc., do not affect our phase diagram. The small amount of ordered ferromagnetic Ni_3Mn phase ($\sim$ 1.7 %) only adds a small temperature-independent moment since $T_C >> 300$ K. Our M vs. H data for the MCP alloy (x = 25) at 300 K is a straight line passing through the origin, just like that of a paramagnet without any detectable hysteresis (see Fig. 3.3).

3.4.2 DC Magnetization

Magnetization measurements M(T) of Ni_{100-x} Mn_x ($15 \leq x \geq 37$) samples were done in the temperature range of 5–350 K, both in low (~ 20 Oe) using a SQUID magnetometer and high (~ 120 kOe) fields. For zero-field-cooled (ZFC) measurements, the samples were cooled down from 350 to 5 K in zero magnetic fields. After cooling, a small field of 20 Oe was applied and held constant while *M* was measured as the temperature was raised slowly up to 350 K. Subsequently the temperature was lowered down to 5 K and the field-cooled (FC) data were taken while heating till 350 K. During this temperature cycle, M (T) was quasistatically measured for finding the various transition temperatures as shown in Fig. 3.4. Many of the conclusions in this section are supported by the hysteresis loop data reported in the next subsection on high-field magnetization.

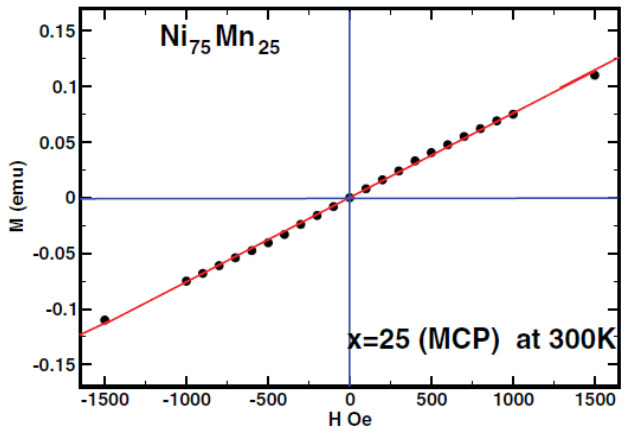

Fig. 3.3 M (H) data for the MCP alloy (x = 25) at 300 K showing paramagnetism without any detectable hysteresis.

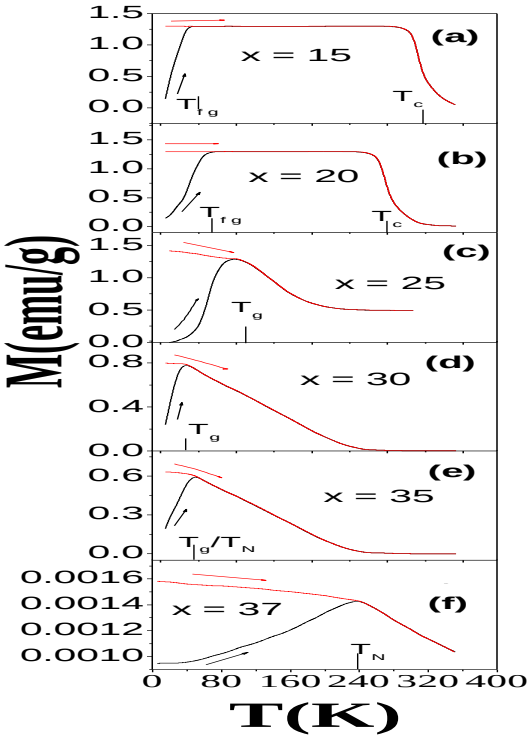

Fig.3.4 Magnetization vs. temperature curves for Ni-Mn alloys between 5 and 350 K on heating after ZFC (black/full line) and then again heating after FC (red/dashed line) in a magnetic field of 20 Oe.

We see from Fig. 3.4 that for alloys with x = 15 and 20, ZFC and FC M(T) curves show irreversibility in the low-temperature region. As T increases from 5 K, there is a bifurcation between ZFC and FC M(T) curves at T_{fg} indicating a transition from a re-entrant ferro SG-like state to a ferromagnetic state. In the intermediate temperature range, both ZFC and FC M(T) remain constant almost until T_C is reached, as found from the dip in dM/dT vs. T plots (not shown here), which is the point of inflection of the M(T) vs. T curve. This is in contrast to the concave M(T) curve beyond the kink points in Fig. 1 of Ref. 1, for x = 23 and 23.5. At low temperatures, our alloys with x = 15 and 20 exhibit a re-entrant/ferro spin-glass-like mixed phase having a spontaneous FM moment as well as glassy behavior below T_{fg} [as seen from M(H) curves at 5 K in the next subsection]. The sample with x = 15 has T_{fg} = 37 K and T_C = 310 K while the sample with x = 20 has T_{fg} = 60 K and T_C = 270 K. This "re-entrant" phase having a

"mixed" character was predicted theoretically[6] long back and involves below T_{fg} a SG ordering of the spins transverse to the coexisting FM moments, while in the FM state above T_{fg} the transverse SG ordering is absent and only the FM remains. It must be stressed here that this coexistence of FM and SG phase below T_{fg} is not a spatially segregated coexistence of infinite ferromagnetic clusters decoupled from finite clusters. The coexistence takes place over the whole sample. The FM ordering persists down to the lowest temperatures ($T << T_{fg}$). AuFe[10] is the first system where the coexistence was observed just below the percolation threshold of 15 at. % Fe. Fe_{80-x} Ni_x Cr_{20} ($10 \leq x \leq 30$) alloys, with a variation of Ni from 10–30 at.% at the cost of Fe with Cr remaining fixed, is another system, similar to the present Ni-Mn, which offered a unique opportunity of observing various magnetic phases such as ferromagnetic, mixed ferro-spin-glass, spin-glass, and antiferromagnetic.[11-13]There the dominant competing interactions were from FM Ni-Cr and AF Cr-Cr interactions which produce FM-SG-like coexisting phases.

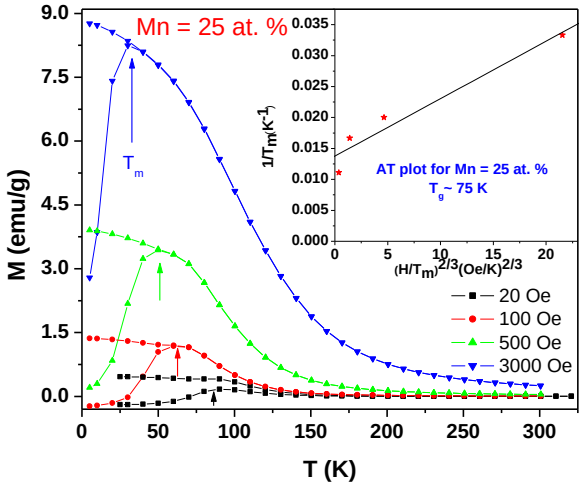

Fig. 3.5 Zero-field-cooled (ZFC) and field-cooled (FC) magnetization curves at H = 20, 50, 200, and 3000 Oe for the alloy $Ni_{75}Mn_{25}$. The inset shows the AT plot giving the glass transition temperature T_g ~ 75 K.

We associated the lower temperature transition at T_{fg} for x = 15 and 20 and the single transition for x = 25 (MCP alloy) with a spin-glass-like phase. Figure 3.5 shows zero-field-cooled (ZFC) and field-cooled (FC) magnetization curves at H = 20, 50, 200, and 3000 Oe for the MCP alloy $Ni_{75}Mn_{25}$. We find a gradual shift of T_m [where ZFC M(T) shows a peak] toward lower temperatures at higher external fields. The ZFC peak at T_m in the SG-like state is due to the gradual unfreezing of moments which allows the magnetic field to align them. Beyond T_m we observe the paramagnetic ∼1/T fall for both the ZFC and FC M(T) and hence no irreversibility for $T > T_m$. At higher applied fields the magnetic field itself tends to disrupt the freezing and hence thermal unfreezing is effective only till a gradually lower value of T_m. This approaches the glass transition temperature T_g as $H \rightarrow 0$ as given by de Almeida-Thouless (AT) relation[12] $1/T_m \sim (H/T_m)^{2/3}$. The inset of Fig. 3.5 shows the AT plot giving the glass transition temperature $T_g \sim$ 75 K, quite different from T_g/T_{fg} found from the bifurcation temperature of 100 K in Fig. 3.4 and ac susceptibility data reported in Section 3.4.4.

The samples with x = 25, 30, 35, and 37 have only one type of transition which can be clearly seen from the steep rise in the M(T) curves [Figs. 3.4(c)– 3.4(f)] until a maximum is reached and then a clear knee indicating a paramagnetic to a spin-glass-like (PM-SG)/antiferromagnetic (AF) transition. T_g/T_{fg} for x = 25 is 100 K and T_g of x = 30 is 29 K. T = 40 K for x = 35 may be a spin-glass freezing temperature or a Neel´ temperature (T_g/T_N) whereas for x = 37, 237 K is clearly the Neel´ temperature T_N, since the moment decreases abruptly at this concentration from 0.6 to 0.0016 emu/g as x changes from 35 to 37. For x = 30–37, the spin-glass-like/antiferromagnetic state goes directly to the paramagnetic one without passing through any intervening ferromagnetic phase.

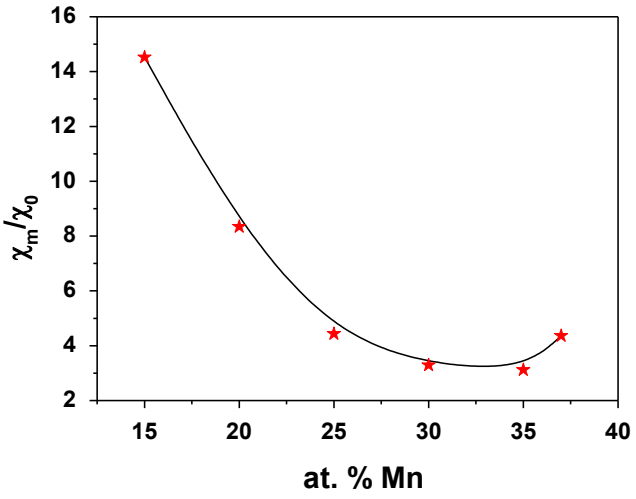

Fig. 3.6 χ_m/χ_0 vs. Mn concentration (at. % Mn) in $Ni_{1-x}Mn_x$ alloys.

In Fig. 3.6, the ratio χ_m/χ_0 vs. Mn concentration (at. % of Mn) is plotted, where χ_m and χ_0 are the demagnetization-corrected low-field susceptibilities (after zero-field cooling) at the maximum values and at 5 K, respectively. We find that the ratio value decreases with increasing x. It is as large as $\sim$ 15 for x = 15 indicating a long-range ferromagnetic order, while at x = 25, the ratio approaches the value ~ 4.4. It is interesting to note that subsequently the value of the ratio reaches a minimum around 35 at. % Mn and then it starts increasing indicating the onset of another long-range order (here antiferromagnetic).

We also show in Fig. 3.7 the data taken for all the samples with a VSM but only down to 80 K at 20 Oe. Excellent reproducibility of the data taken by two different instruments of widely varying sensitivity (SQUID and VSM) gives us great confidence in our data and hence the conclusions drawn there from.

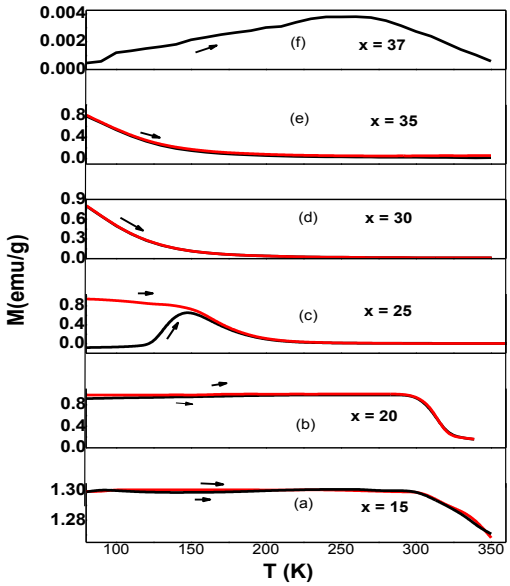

Fig. 3.7 Magnetization (emu/g) vs. temperature curves for Ni-Mn alloys between 80 and 350 K on heating after ZFC (black line) and then again heating after FC (red line) in a magnetic field of 20 Oe using a vibrating sample magnetometer (VSM).

3.4.3 High-field magnetization and hysteresis loops

Hysteresis loops were obtained for each sample after cooling in zero fields to 5 K from above $T_C/T_{fg}/T_g/T_N$ and measured in fields up to 50 kOe using the vibrating-sample magnetometer. In Fig. 3.8 we have plotted the magnetization of all six samples at 5 K only till 16 kOe. They show drastic changes with Mn content. For the samples with x = 15 and 20, 16 kOe was sufficient for magnetic saturation. In case of x = 25, the magnetization was still rising at the highest attainable field of 120 kOe**,** as shown in the inset of Fig. 3.8, top panel and this locates the tri-critical point. The re-entrant/ferro spin-glass (FSG)-like mixed phases for x = 15, 20, and 25 have spontaneous FM moments below T_{fg}. This is seen clearly from their respective values of H_C of 30, 90, and 400 Oe at 5 K which is much less than their T_{fg} of 37, 60, and 100 K, respectively. Finally their H_C's tend to zero above their T_C's of 311, 270, and 100 K, respectively. The increase of H_C with Mn is what is expected. H_C increases with the increase of

impurity content and the associated lattice strain. The bell-shaped low-field region for x = 25 resembles those observed in spin glasses but the sample still retains a high susceptibility at low temperatures. For lower values of x, the $M(H)$ curves saturate at fields ~1 kOe like those of ferromagnets but with the increase of x, the lack of saturation gradually becomes more evident and finally around x = 37 their curvature disappears and $M(H)$ becomes almost linear implying an antiferromagnetic character (bottom panel of Fig. 3.8).

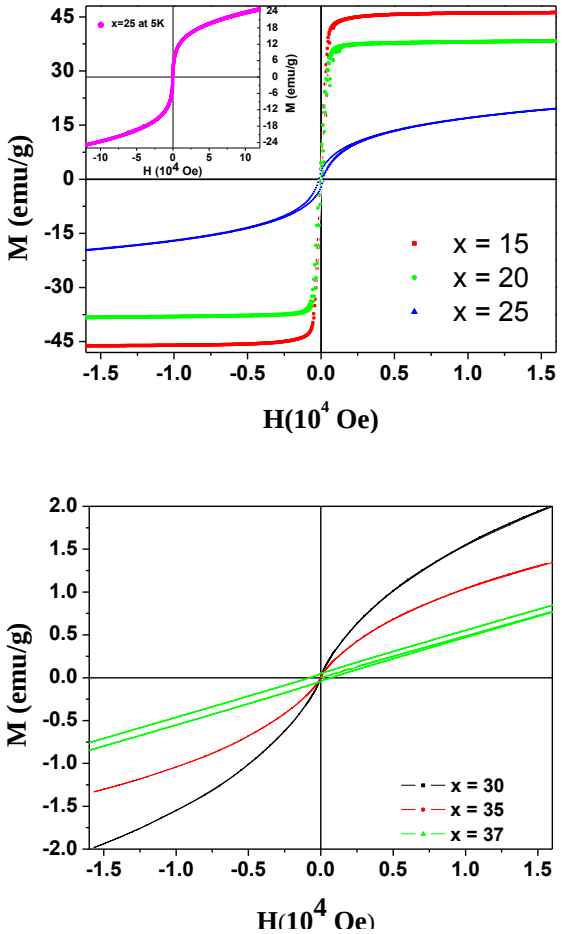

Fig. 3.8 Magnetization measured at low temperatures (5 K) as a function of applied fields H till 50 kOe (shown only till 16 kOe). The inset in the top panel shows the M(H) data till 120 kOe of the sample with x= 25.

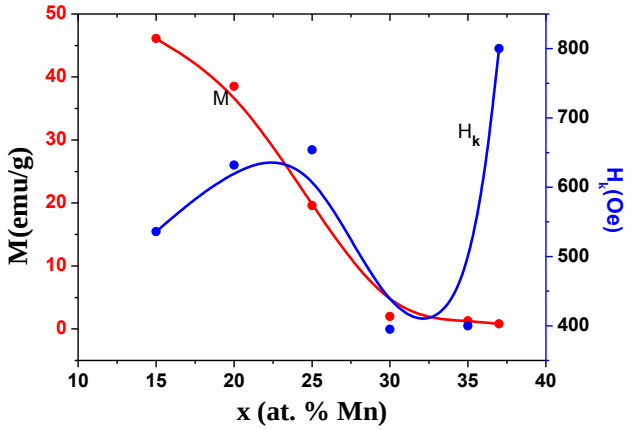

Fig. 3.9 Average magnetization (M) and uniaxial anisotropy field (H_k) vs. x (at. % Mn).

We also observe that every sample has an uniaxial anisotropy field (H_k) which we found by using the singular point detection technique[14] (the second derivative of the virgin M-H curves gives a sharp peak at H_k). H_k is plotted against Mn concentration, x in Fig. 3.9 and so is M(x) at 16 kOe which shows a sharp decrease from ~ 46 to ~1 emu/gm from the FSG to the AFM phase. It should be noted that the anisotropy field changes with the magnetic phase of the samples, e.g. from x =15 to the multicritical point (x = 25), H_k increases slowly, then it drops till x ~ 30 and then rises sharply as the AFM state grows. Here larger fields are necessary to change the preferred orientation as LRO antiferromagnetic phase develops thereafter. We notice that H_K shows anomaly while passing through the multicritical point which is the boundary between ferromagnetic and antiferromagnetic phases. Table 3.2 gives the values of x, M at 16 kOe, H_k, $T_{fg}/T_g/T_N$ (obtained from the bifurcation of ZFC and FC curves), and T_c. The sudden fall of magnetization beyond x = 25 is obvious from its values at H = 1 kOe as given in Table 3.2 and is indicative of the disappearance of long-range ferromagnetism.

Table 3.2 Magnetic properties of $Ni_{1-x}Mn_x$ samples.

x (at. % Mn)	M at H = 1 kOe (emu/g)	H_k (Oe)	T_{fg} / T_g/ T_N (K)	T_c (K)
15	43.33	536	37	311
20	36.12	632	60	270
25	6.80	654	100	100
30	0.31	395	29	-
35	0.22	400	40	-
37	0.05	800	237	-

M(T) data for x = 15, 20, and 25 at 3000 Oe from 5-40 K have been analyzed (fits not shown) in terms of Bloch's spin-waves spin-wave theory. We found that the spin-wave stiffness constants are 236±12, 117±3, and 110±2 meV $Å^2$ as against 525 meV $Å^2$ for Ni. This establishes firmly that ferromagnetism persists even below T_{fg}.

3.4.4 AC susceptibility

AC-susceptibility (χ_{AC}) was measured in $Ni_{100-x}Mn_x$ alloys with x = 25, 20, and 30 after ZFC to 5 K from 300 K and measuring in small ac-fields of 1 Oe at 2.9, 29, 290, 590 and 601 Hz and 5 Oe at ~ 100 to 10,000 Hz using MPMS and PPMS, respectively for probing the possible spin-glass-like ordering observed in dc M(H,T) studies. The spin-freezing temperatures of the alloys were estimated from the temperature dependence of χ_{AC}. They agreed reasonably well in most cases with those found from the DC magnetization measurements. We found that improper thermal treatment (quenching) leads to irreproducible T_g/T_{fg} but T_C is too robust to be affected by short-range order.

(i) x = 25

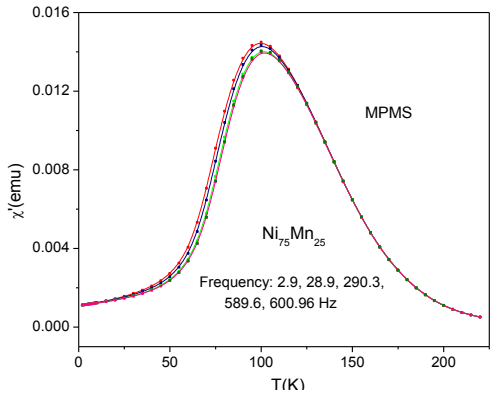

Fig. 3.10 Real part of ac-susceptibility χ' (emu) vs. T between 10 and 300 K for x = 25 at several frequencies using MPMS.

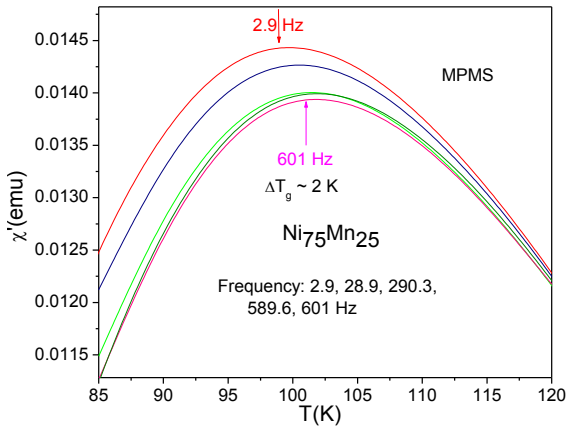

Fig. 3.11 Fig. 3.10 on an expanded scale between 85 and 120 K for x = 25 for finding the frequency dependence of T_g.

$Ni_{75}Mn_{25}$ is the most interesting as well as complicated composition because it is the MCP with three co-existing magnetic phases. Figure 3.10 shows the real part of ac-susceptibility χ' (emu) vs. T for x = 25 at several frequencies. All of them have rounded maxima around 100 K; the lowest frequency has the highest χ' which is rather obvious since at low frequencies clusters of all size respond to magnetic fields whereas at high frequencies only smaller clusters do. They converge to a non-zero $\chi'(T)/\chi'(T_g)$ of ~ 0.1 as $T \rightarrow 0$ K and are frequency independent above T_g. In canonical spin glasses, say, CuMn (4.4 at. %)[12], $\chi'(T)/\chi'(T_g) \sim 0.5$ as $T \rightarrow 0$ K. As shown in Fig. 3.10 which is actually Fig 3.10 on an expanded scale, there is an increase in T_g of ~ 3 K around 100 K with a 200-fold increase in frequency from 3 to 600 Hz. For canonical spin glasses T_g decreases with increasing frequency since the smaller clusters have lower freezing temperature. Many of the above features in x = 25 are not typical in canonical spin glasses since after all, x = 25 and T ~ 100 K is the MCP where spin-glass, ferro-spin-glass, and ferromagnetic phase boundaries intersect.

Measuring χ' (T) in ac-fields of 5 Oe between 10 and 300 K using the PPMS we get what is shown in Fig. 3.12. Here ΔT_g ~ + 7 K around 100 K as ν changes from ~ 100 to 5000 Hz.

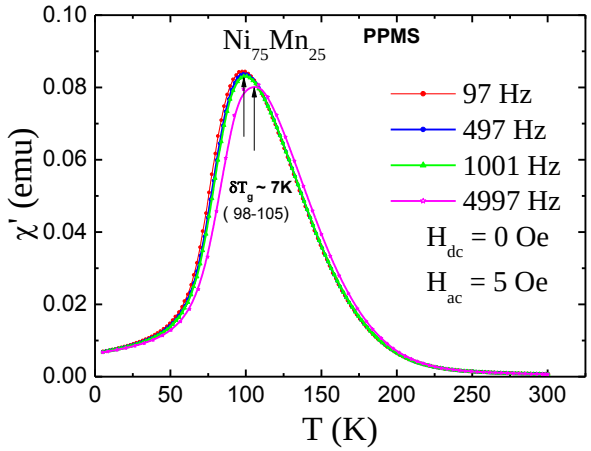

Fig.3.12 Real part of ac-susceptibility χ' (emu) vs. T for x = 25 at several frequencies between 100 and 5000 Hz using PPMS.

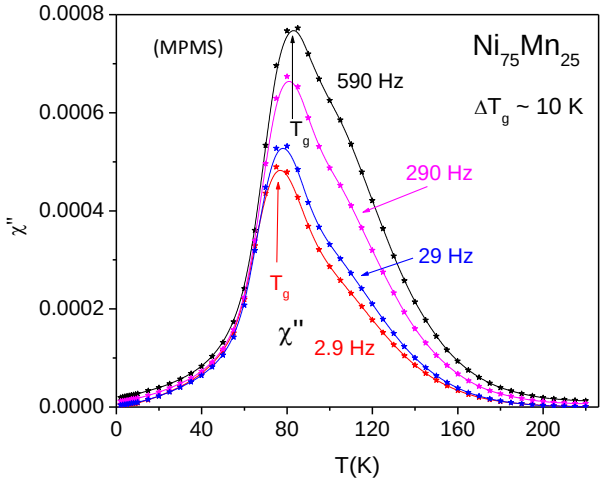

Fig.3.13 Imaginary part of ac-susceptibility χ'' (emu) vs. T for x = 25 at several frequencies using MPMS

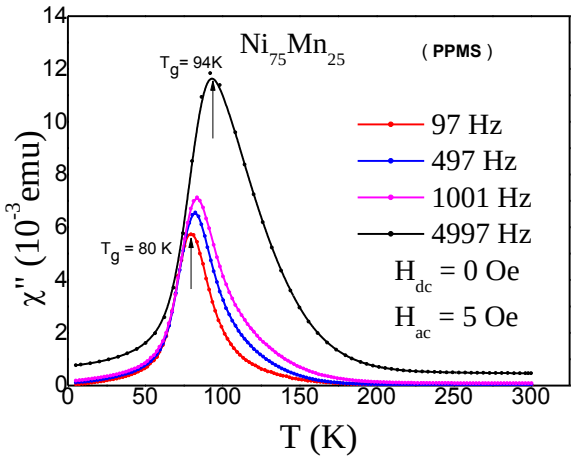

Fig.3.14 Imaginary part of ac-susceptibility χ'' (emu) vs. T for x = 25 at several frequencies between ~ 100 and 5000 Hz using PPMS.

The imaginary part χ'', the absorption part of the susceptibility is the Fourier transform of the two-spin correlation function which characterizes the dynamics of the magnetic system. χ'' is expected to show some anomaly near the magnetic phase transitions. χ'' extrapolates to ~ 50 % of its peak value as $T \rightarrow 0$ in Cu-Mn and Ag-Mn spin glasses[12] but in EuSrS, this extrapolates to zero as $T \rightarrow 0$. Figures 3.13 and 3.14 show the imaginary part of ac-susceptibility χ'' (emu) vs. T for x = 25 at several frequencies, measured with an MPMS and a PPMS, respectively. The peaks are much sharper than those of χ'. χ'' extrapolates to zero as $T \rightarrow 0$ as in EuSrS. Also their magnitudes increase with ν as in many SG's. χ'' shifts by ~ + 10 K from 80 K for ~ 3 to 600 Hz (MPMS) and + 14 K for ~ 100 to 5000 Hz (PPMS).

(ii) x = 20

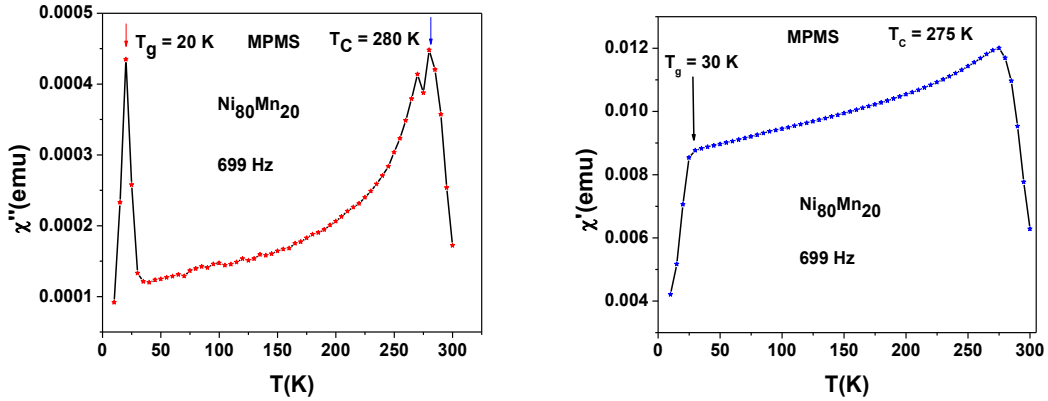

(a) (b)

Fig.3.15 (a) Real part of ac-susceptibility χ' (emu) vs. T and (b) Imaginary part of ac-susceptibility χ'' (emu) vs. T for x = 20 at 699 Hz, using MPMS.

DC measurements in the alloy with x = 20 had indicated two transitions at T_{fg} = 60 K and T_C = 270 K. Figure 3.15(a) shows in the real part χ' of the susceptibility a shoulder at 30 K and a peak at 275 K whereas in Fig. 3.15(b) the imaginary part χ'' gives a very sharp peak at 20 K and another at 280 K. Both χ' and χ'' extrapolate to ~ 25 % of their peak values as $T \rightarrow 0$. Whereas T_C remains more or less the same in DC and ac-χ measurements, the contradiction in the value of T_{fg} forced us to probe ac χ' and χ'' with PPMS and shown in Figs. 3.16 and 3.17, respectively.

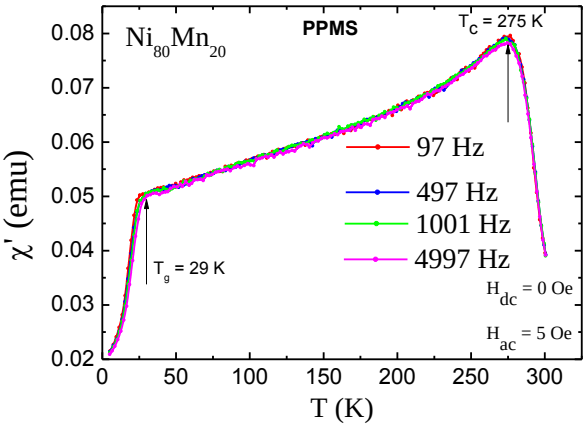

Fig.3.16 Real part of ac-susceptibility χ′ (emu) vs. T for x = 20 between 100 and 5000 Hz using PPMS.

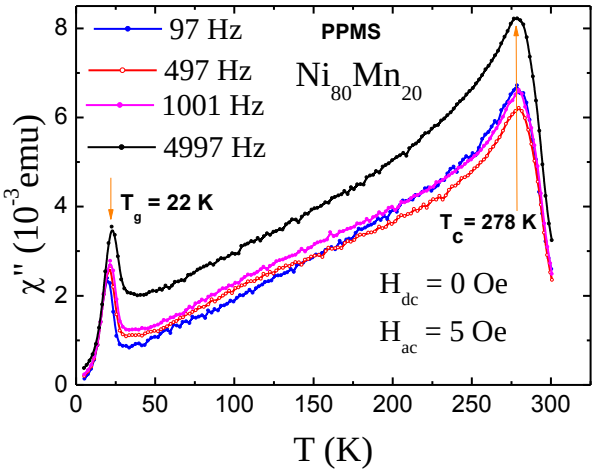

Fig.3.17 Imaginary part of ac-susceptibility χ′′ (emu) vs. T for x = 20 between 100 and 5000 Hz using PPMS.

Here χ′ shows a shoulder at 29 K and a peak at 275 K whereas χ′′ gives a very sharp peak at 22 K and another at 278 K. So, MPMS and PPMS give the same data even quantitatively. So we conclude that T_{fg} is possibly quite sensitive to quenching conditions and repeated the ac χ′

measurements with a different piece of the same composition (x = 20) annealed for 48 hrs and quenched to room temperature from 1200^0 C. Figure 3.18 plots χ' vs. T showing clearly the standard increase in T_{fg} with frequency and ΔT_{fg} ~ 12 K (62 to 74 K) in the frequency range 111-9997 Hz. This also confirms that T_{fg} ~ 60 K as found from DC measurements and more importantly the sensitivity of transition temperatures to annealing conditions.

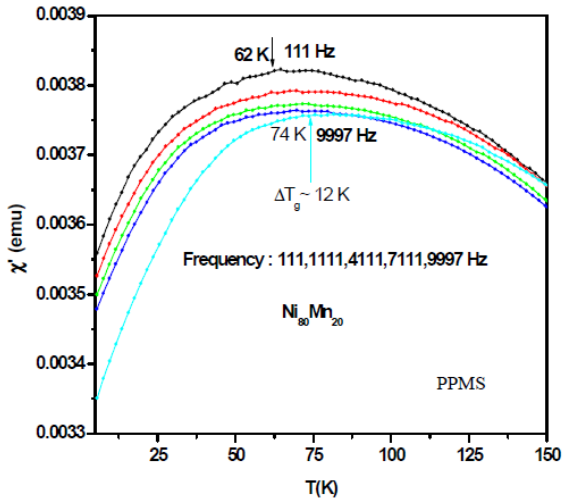

Fig.3.18 Plot of χ' vs. T with a different piece of the same composition (x = 20) annealed for 48 hrs and quenched to room temperature from 1200^0 C and using a PPMS. It shows that T_{fg} increases with frequency.

(iii) x = 30

The zero-DC field AC susceptibility of $Ni_{70}Mn_{30}$ was done with an AC drive field of 5 Oe between 11 and 7111 Hz using PPMS. Figure 3.19 shows the imaginary part of ac-susceptibility χ'' (emu) vs. T for x = 30 with different frequencies. From the temperature dependence of the in-phase (χ') **(**not shown here) and the out-of-phase (χ'') we notice a steep rise around 18 K which is not too different from T_{fg} (29 K) found from the DC data. The cusp like

peak in χ'' and the dependence of the location of the cusp on frequency confirms the freezing temperature. χ'' increases with frequency as expected.

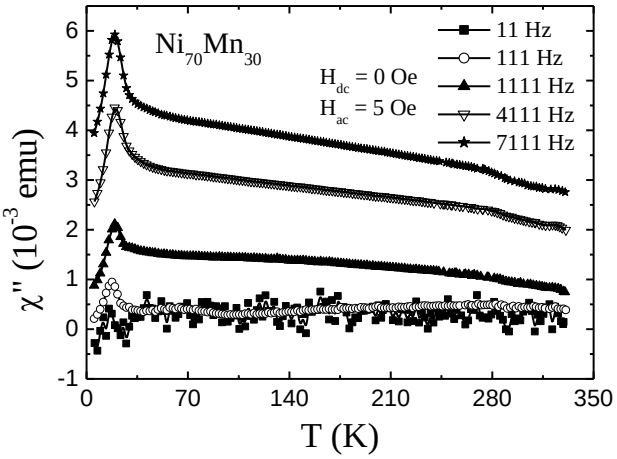

Fig.3.19 Imaginary part of ac-susceptibility χ'' (emu) vs. T for x = 30 with different frequencies using PPMS.

3.4.4 Magnetic relaxation

Thermoremanent magnetization is a thermally activated process. When the applied magnetic field is removed, the magnetization tries to approach the remanent magnetization in order to minimize the energy of the system. A magnetic field of 100 Oe was applied to the sample at 300 K and the sample was cooled down to the measuring temperature. After the temperature was stabilized, the magnetic field was set to zero and the magnetization vs. time M(t) measurements were started and continued for about 13000 s. Figure 3.20 plots the experimental time decay of normalized magnetization ln[M(t)/M(0)] for $0 < t < 10{,}000$ s for $Ni_{75}Mn_{25}$ alloy at different temperatures. The magnetization shows anomalously slow relaxation as we approach and cross the glass-transition temperature. Around and below 70 K, although for long times (> 6000 s) ln[$M(t)/M(0)$] can be fitted to a straight line; its slope is so small that anomalously slow (power law or logarithmic) decay is suggested.

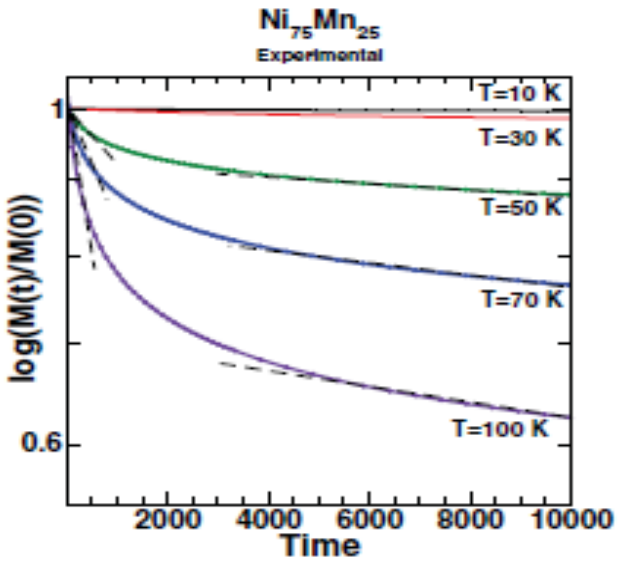

Fig.3.20 Time decay of magnetization for $Ni_{75}Mn_{25}$ alloy at different temperatures. The magnetization shows anomalously slow relaxation as we approach and cross the glass-transition temperature below 100 K where we can no longer fit the data to exponential decay functions.

On the theoretical side, the magnetic pair energies $J^{QQ/}(R)$ are used to calculate the time-dependent magnetic moment via a Landu-Lifshitz-Gilbert (LLG) equation of motion. This is an important tool to study the existence of the spin-glass phase. We have used an atomistic approach as proposed by Skubic et al.[15] based on density functional theory, starts with the LLG equation. Figure 3.21 shows the behaviour of log[M(t)/M(0)] vs. t for the composition $Ni_{75}Mn_{25}$ (MCP). The linear fits at small and asymptotic times indicate decays at two time scales: a fast decay initially, indicating decay to a local minimum in the energy landscape. At long times the system slowly relaxes toward the global minimum. Table 3.3 shows these decay rates associated with the two relaxation processes just described. This has been done for both the experimental data and the LLG results. We note that across the whole temperature range they agree rather well with exponential relaxations at high temperatures to an almost logarithmic relaxation at 10 K. This is a definite signature of the spin-glass phase.

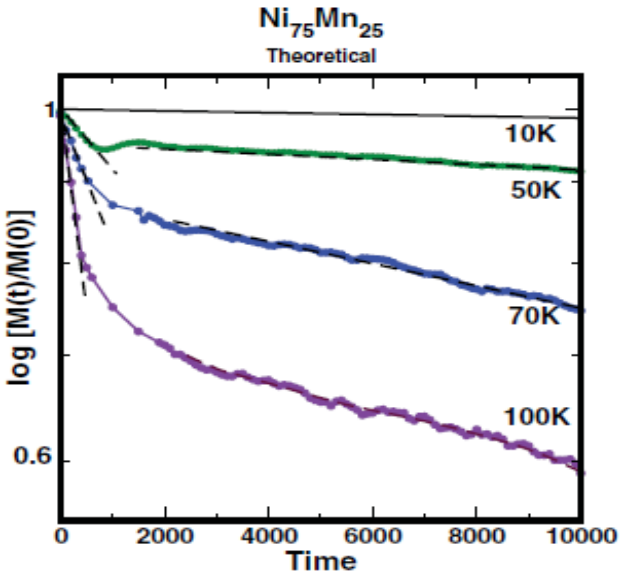

Fig.3.21 LLG results for the time decay of magnetization for $Ni_{75}Mn_{25}$ at different temperatures. Here too the alloy magnetization shows anomalously slow relaxation as we approach and cross the glass-transition temperature below 100 K. This is to be compared with Fig. 3.20 (experimental).

Table 3.3 The decay rates for the initial fast decay and the subsequent decay to a global minimum [m(t)/m(0) = exp (-t/τ)] are shown for both the experimental data and LLG simulation results. The alloy shows freezing behavior at low temperatures. The asterisk (*) indicates that the fit is a straight line which is almost horizontal.

	Experimental		LLG	
Temperature (K)	τ_1^{-1}	τ_2^{-1}	τ_1^{-1}	τ_2^{-1}
100	820	93	813	140
70	482	76	449	120
50	245	45	200	41
30	21	10		
10	*	*	*	*

3.4.5 Experimental Phase Diagram

Figure 3.22 depicts our magnetic phase diagram of disordered $Ni_{1-x}Mn_x$ alloys showing ferromagnetic (FM), ferro-spin-glass (FSG), conventional (canonical) spin-glass (SG), paramagnetic (PM), and antiferromagnetic (AFM) regions. The values of T_C, T_{fg}, T_g, and T_N are taken from Fig. 3.4 (H = 20 Oe). The lines joining the first three all meet at a point which is called the multicritical point (MCP; x = 25, T = 100 K). Beyond the MCP, at higher at. % of Mn, the spin-glass state directly goes to the paramagnetic state (up to 30 at. % Mn) or the antiferromagnetic state to the paramagnetic state (for 35 and 37 at.% Mn) with no intervening ferromagnetic phase. Beyond x = 25 till 30, T_g goes down; then at 35 there is a slight increase in the bifurcation temperature while M gradually decreases all the way (from ~1 to 0.6 emu/g). However, according to the neutron diffraction work[16] long-range antiferromagnetism does not set in for x = 30 but x = 35 at. % Mn is indeed antiferromagnetic but T_N could not be found because of the weak Bragg peak and the temperature-dependent diffuse scattering. For x = 35, they found long-range antiferromagnetic order with T_N anywhere between 90 and 360 K. For lower values of x, below the multicritical point, the samples pass through two phases—ferromagnetic (FM) and re-entrant spin-glass or ferro-spin-glass. In re-entrant spin-glass (RSG or FSG) systems, with decreasing temperature one observes a paramagnetic-ferromagnetic transition at T_C. Then at a lower temperature T_{fg}, spin-glass-like properties show up. In the phase diagram we get a critical concentration which is the point (x = 25) where T_C and T_{fg} (100 K) come together. We further note that the value of T_{fg} increases and T_C decreases with increasing x. The variation of T_g with Mn concentration is very interesting. Up to x = 30, it decreases linearly with increasing x, then we get T_N in place of T_g signifying AFM order which increases with Mn concentration. The boundary between the re-entrant/ferro-spin-glass (FSG) and the canonical spin-glass (SG) phases is a vertical line which touches the multicritical point (x = 25).

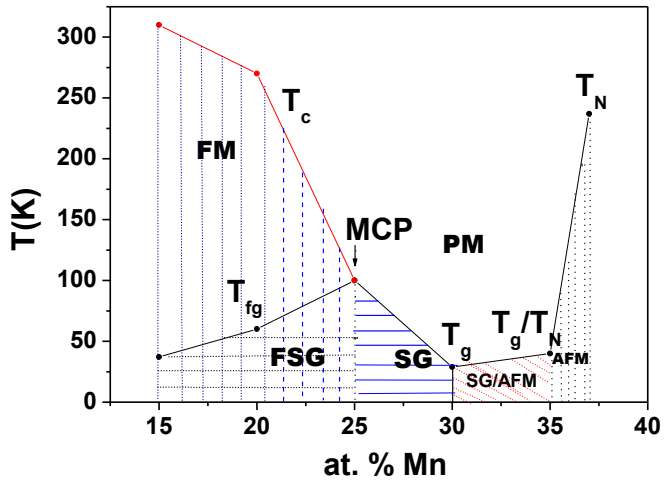

Fig.3.22 Experimental phase diagram (temperature vs. composition) of disordered $Ni_{1-x}Mn_x$ alloys.

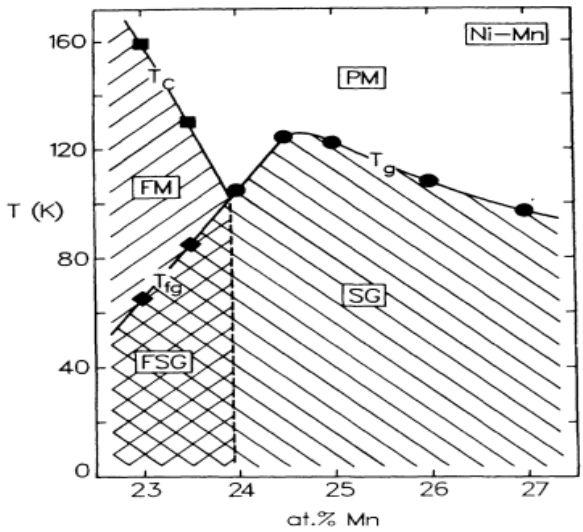

Fig.3.23 Magnetic phase diagram of disordered $Ni_{1-x}Mn_x$ alloys (x = 23-27) obtained by Kouvel et al.[3]

For comparison we show in Fig. 3.23 the magnetic phase diagram of disordered $Ni_{1-x}Mn_x$ alloys for x = 23-27 obtained in 1987 by Kouvel et al.[3]. In this narrower composition range, there is good qualitative agreement with the phase diagram of the present work, except that i) the MCP is at x = 24 instead of 25 at % Mn which is not a big difference in view of the fact that the disordered state depends very much on the effective quenching of the alloys from high temperatures and ii) the 2-phase (SG-PM) line from the MCP has a positive slope resulting in further increase of T_g till x = 24.5 and then a negative slope till x = 27. In contrast in the present work the 2-phase lines starting from the MCP (x = 25) has a positive slope on the ferromagnetic (FM) side and a negative slope on the antiferrromagnetic (AFM) side. On the Mn-poor side the two-phase (FM and FSG) line gives lower T_{fg} as Mn decreases and on the Mn-rich side the two-phase (PM and SG) line gives lower T_g as Mn increases. This is most logical since the short-range order or the autocorrelation function of the spin-glass state is gradually destroyed with the advent of long-range order of both kinds, FM and AFM.

The phase diagram that we obtained from magnetization data shows an interesting concentration range ($15 \leq x \leq 25$) in which the system undergoes two magnetic transitions on lowering the temperature: from paramagnetism to 'ferromagnetism' and from 'ferromagnetism' to a spin-glass-like state. For ($25 \leq x \leq 35$), however, only paramagnetic to spin-glass-like transition is observed and x = 37 shows only one transition but that is from a paramagnetic to an antiferromagnetic state. Since the magnetic properties of quenched Ni-Mn alloys depend strongly on composition around 25 at. % Mn, it is essential to ensure an accurate determination of composition. So, we have taken EDAX (Energy dispersive X- ray analysis) of every sample and got satisfactory results as seen from Table 3.4. We find (inset of Fig. 3.2) that the lattice

parameter increases monotonically with x, the Mn concentration and shows no anomaly as the magnetic state widely changes from a mixed FM-SG-like state to an AFM one.

Table 3.4. EDAX Quantification

Sample	Element	Wt. %
$Ni_{85}Mn_{15}$	Ni Mn	85.6 14.4
$Ni_{80}Mn_{20}$	Ni Mn	81.4 18.6
$Ni_{75}Mn_{25}$	Ni Mn	73.7 26.3
$Ni_{70}Mn_{30}$	Ni Mn	69.2 30.8
$Ni_{65}Mn_{35}$	Ni Mn	64.2 35.8
$Ni_{63}Mn_{37}$	Ni Mn	63.2 36.8

3.5 Theoretical Analysis

3.5.1 Electronic Structure

Using a first-principles theoretical analysis we have obtained an accurate electronic structure of these alloy systems. This involves two steps: first a density-functional based derivation of the Hamiltonian "potential parameters" and structure matrix which describe the chemistry and crystallography of the alloys. Second, we need an accurate technique to deal with the disorder in the system and average over the disordered configurations. For the former we have chosen the tight-binding linear muffin-tin orbital (TB-LMTO) method[17] and for the latter the augmented space recursion (ASR) formalism.[18]This formalism gives a prescription of how to obtain the configuration average of Green's and response functions in a disordered system by downfolding onto a specific subspace of the configuration space. Details have been discussed in

detail in a monograph.[19] This method goes beyond the single-site, mean-field coherent potential approximation (CPA) and three of the successful generalizations of the CPA are based on this theorem (traveling cluster CPA[20], itinerant CPA[21], and cluster CPA[22]). The configuration-averaged Green's function $\langle\langle G^{\sigma}_{\vec{R}_i L\, \vec{R}_i L}(E+i\delta^+)\rangle\rangle$ leads to the local density of states, the charge and magnetization densities, and the local magnetic moment per atom:

$$
\begin{aligned}
n^{\sigma}(E,\vec{R}_i) &= -\frac{1}{\pi}\mathrm{Im}\langle\langle G^{\sigma}_{\vec{R}_i L \vec{R}_i L}(E+i\delta^+)\rangle\rangle, \\
\rho^{\sigma}(\vec{r}-\vec{R}_i) &= \int_{-\infty}^{E_F} dE\, |\Phi(\vec{r}-\vec{R}_i,E)|^2 n^{\sigma}(E,\vec{R}_i), \\
m(\vec{R}_i) &= \int_{AS} d^3\vec{r}\{\rho^{\uparrow}(\vec{r}-\vec{R}_i)-\rho^{\downarrow}(\vec{r}-\vec{R}_i)\}.
\end{aligned}
\qquad (3.1)
$$

Here R_i labels an atomic sphere around an ion core sitting at the site i, L are the angular momentum quantum numbers (l,m), σ is the spin label, and AS is the atomic sphere $|r - R_i| < r_0$. The interesting result that comes out of these calculations is the composition variation of the average local magnetic moment per atom. This is something we can compare with experiments and ascertain whether our electronic structure method is appropriate for further study. Figure 3.24 shows this comparison to be satisfactory within the limits of our approximation and gives us confidence for the next step.

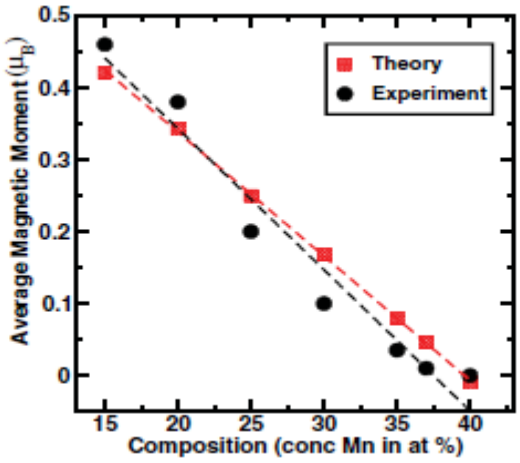

Fig.3.24 Experimental and theoretical magnetic moments as functions of composition.

3.5.2 Mean-field and Monte Carlo analysis of the random Heisenberg Model

We have obtained a mean-field calculation of the critical temperatures and obtained the magnetic phase diagram in Fig. 3.25. If we compare this phase diagram with Fig. 3.22 we see that our mean-field-based calculation qualitatively yields phase boundary as a function of Mn concentration with a ferromagnetic phase for $x < 15$, an antiferromagnetic phase for $x > 37$, with glassy phases in between. Of course, it grossly overestimates critical temperatures, which is not surprising for a simple mean-field calculation and the shape of the paramagnetic-spin-glass boundary is rather crudely reproduced.

We followed up the mean-field analysis with a Monte Carlo simulation using the J_{ij}^{QQ}, calculated by us earlier. We note two points: First, the Monte Carlo had to be carried out in a chemically disordered alloy. This is because in the temperature range where the magnetic transition takes place, the alloy remains chemically disordered. To obtain a disordered unit cell, we first calculated the chemical exchange integrals based on a philosophy identical to the magnetic case: starting from a disordered background and embedding an AA, AB, or BB pair configuration before calculating the total energy differences. Having obtained these, we ran a Monte Carlo routine to obtain the disordered background. Finally, we turned on a Monte Carlo analysis of magnetic moments against the random atomic background. Second, Monte Carlo can give us information only across a para-ferro transition. The compositions were so chosen as to be in the region where we have a para to ferromagnetic transition: at compositions with $x = 15$, 20, 25, 30, 35, and 37 at. %. Comparison between Figs. 3.25 and 3.22 shows that the Monte Carlo transition temperatures are now quite near the experimental values.

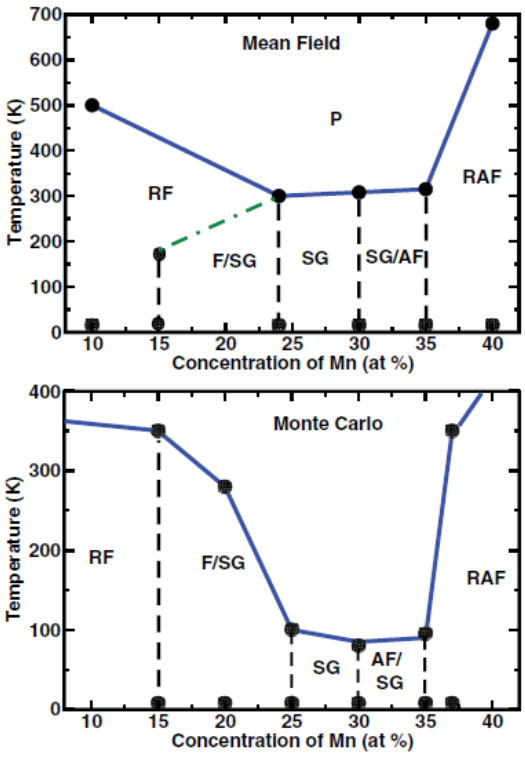

Fig.3.25 Top: Phase diagram based on a mean-field calculation. The critical temperatures are overestimated. Bottom: The same based on a Monte Carlo estimates. Now the critical temperatures and compositions are nearer to the experimental values.

3.6 Conclusions

We conclude from a detailed experimental magnetic study of several disordered Ni_{1-x} Mn_x alloys that the spin-glass-like state in these alloys below T_{fg} has a spontaneous (FM) moment. This moment decreases slowly with rising temperature and merges smoothly with the spontaneous moment of the FM state at the multicritical point (MCP) around 25 at. % Mn. The existence of the re-entrant SG phase, a canonical SG phase, and the onset of an antiferromagnetic phase around 37 at. % Mn is also confirmed. In brief, we found ferromagnetic LRO with re-entrant spin-glass (RSG)/ferro-spin-glass (FSG) phase for $x \leq 25$, an antiferromagnetic LRO

around $x \sim 37$, and a gradual change from a canonical spin-glass state to a long-range AF phase in the intermediate composition region.

A first-principles density functional based theory predicts magnetization, as a function of composition, which is in good agreement with experiments. Since we believe that the spin-glass transition is a dynamic freezing of spin degrees of freedom, we studied magnetization relaxation using LLG formalism. We showed that in the composition range where experiments show spin-glassy behaviour, we also see anomalously slow relaxation of magnetization.

Bibliography

1. R. Hahn and E. Kneller, Z. Metallkd. **49**, 426 (1958).
2. J. S. Kouvel and C. D. Graham, J. Phys. Chem. Solids **11**, 220 (1959).
3. W. Abdul-Razzaq and J. S. Kouvel, Phys. Rev. B **35**, 1764 (1987).
4. R. G. Aitken, T. D. Cheung, J. S. Kouvel, and H. Hurdequint, J. Magn. Magn. Mater. **30**, L1 (1982).
5. J. J. Hauser and J. E. Bernardini, Phys. Rev. B **30**, 3803 (1984).
6. A. Mookerjee, Pramana **14**, 11 (1980); M. Gabay and G. Toulouse, Phys. Rev. Lett. **47**, 201 (1981).
7. W. J. Carr, Phys. Rev. **85**, 590 (1952).
8. R. M. Bozorth, Ferromagnetism (D. Van Nostrand Company, Inc.), New York, 1951.
9. J. M. Cowley, Phys. Rev. **77**, 669 (1950).
10. B. R. Coles, B. V. Sarkissian, and R. H. Taylor, Philos. Mag. B **37**, 489 (1978); B. H. Verbeek and J. A. Mydosh, J. Phys. F **8**, L109 (1978).
11. A. K. Majumdar and P. v. Blanckenhagen, Phys. Rev. B **29**, 4079 (1984).
12. J. A. Mydosh, *Spin Glasses: An Experimental Introduction* (Taylor & Francis, London, 1993).
13. D. Chowdhury and A. Mookerjee, J. Phys.: Condens. Matter **17**, 5049 (1984)**.**
14. F. Bolzoni and R. Cabassi, Physica B 346-347, **524** (2004).
15. B. Skubic, J. Hellsvik, L. Nordström, and O. Eriksson, J. Phys.: Condens. Matter **20**, 315203 (2008).
16. O. Moze, T. J Hicks and P. von Blanckenhagen, J. Magn. Magn. Mater**. 42**, 103(1984).
17. O. K. Andersen and O. Jepsen, Phys. Rev. Lett. **53**, 2571 (1984).
18. A. Mookerjee, J. Phys. C **6**, L205 (1973).
19. A. Mookerjee, in *Electronic Structure of Alloys, Surfaces, and Clusters*, edited by D. D. Sarma and A. Mookerjee (Taylor & Francis, London, 2003).
20. R. Mills and P. Ratanavararaksa, Phys. Rev. B **18**, 5291 (1978).
21. S. Ghosh, P. L. Leath, and M. H. Cohen, Phys. Rev. B **66**, 214206 (2002).
22. Moshiour Rahaman and A. Mookerjee, Phys. Rev. B **79**, 054201 (2009).

CHAPTER IV

Magneto-transport properties in disordered Ni-Mn alloys around the multicritical point

4.1 Preamble

We present the results of detailed measurements of the temperature and field dependence of the electrical resistivity, ρ of disordered $Ni_{100-x}Mn_x$ alloys (x = 15, 20, 25, 30, 35, and 37) in the temperature range $5 \leq T \leq 350$ K using the four-probe method. We find distinctly different behavior of ρ(T) below and above the multicritical point (MCP) x = 25 recently found by us through detailed magnetic measurements in the *same set of samples*. In the ferromagnetic/ferro-spin-glass ($x \leq 25$) phase, ρ(T) is dominated by large electron-phonon and electron-magnon s-d scattering while in the spin-glass/antiferromagnetic regime ($x \geq 25$) resistivity minima show up due to larger disorder with resistivity ~ (150-185) μΩcm. Here ρ(T) is dominated by e-e interaction ~ - √T and electron-phonon s-d scattering. The magnetoresistance is negative below and positive above the MCP.

4.2 Earlier studies

The magnetic phase diagram of Ni-rich $Ni_{1-x}Mn_x$ ($15 \leq x \leq 37$) alloys around the multicritical point was established recently[1]. Now we have taken up the transport studies on the *same set of alloys*. *Oftentimes*, this is not the case and the interpretation of the resistivity data based on their magnetic state becomes less reliable, especially when one of the components (here Mn) has a much higher vapor pressure. In general, electrical transport properties of metallic alloys, whether amorphous or crystalline, have always attracted a lot of attention. In the present disordered Ni-Mn alloy system, frustration due to competing magnetic interactions leads to interesting macroscopic properties, both magnetic and transport. Often the spin-glass state is

sandwiched between long-range FM and AFM phases. Reentrant behavior has been found in a variety of disordered magnetic materials in which there is a coexistence of spin-glass and long-range ferromagnetic ordering. On cooling, such materials often exhibit a transition from the paramagnetic (PM) to the ferromagnetic phase at the Curie temperature T_C, and on further cooling a spin-glass-like phase appears at T_g when the spins become locally *canted* and in zero fields ferromagnetism along z-direction coexists with transverse freezing of spins in the X-Y plane. This is commonly known as the reentrant-spin-glass (RSG) or ferro-spin-glass (FSG) phase. This interpretation is based on the transverse spin freezing approach of Mookerjee and Roy[2] and Gabay and Toulouse[3]. In the last few decades, a large number of attempts have been made both theoretically as well as experimentally, but a complete understanding of their electrical transport properties has not yet been achieved. To the best of our knowledge, hardly any attempt has been made yet in investigating electron transport properties in Ni-Mn *alloys near the multicritical point*.

In transition metal alloys the electrical resistivity arises due to the scattering of conduction electrons by phonons and magnons, apart from the residual resistivity. In simple metals, the electron-phonon interaction is well described by Bloch-Grüneissen formula that considers intraband s-s electron-phonon scattering whereas in transition metals and their alloys, scattering involving s-d transitions, in addition to the above s-s term, has to be considered. Besides these, scattering of conduction electrons by localized as well as itinerant magnetic electrons (often called spin-disorder resistivity) has got an important role in transition metal alloys.

4.3 Theory

A theoretical calculation for the temperature dependence of resistivity in these polycrystalline materials is very difficult for various reasons. The absence of a proper band structure calculation poses the main hurdle. No theory has been developed clearly so far which can describe the band structure as well as the spin structure of these kinds of 3d transition-metal alloys. In concentrated disordered magnetic alloys, the electron transport is much more difficult

to understand because of the involvement of a large number of complicated scattering mechanisms. In 3d transition metals and alloys scattering of the conduction s electrons by phonons and their interaction with magnetic spin system (spin-disorder resistivity) are the main sources of the temperature dependence of the resistivity.

The measured resistivity in these alloys has contributions from different physical phenomena. If we assume the validity of Matthiessen's rule, then the electrical resistivity has got contributions from static disorder, i.e., the residual resistivity (ρ_0), the electron-phonon scattering (ρ_{ph}), and the magnetic scattering (ρ_{mag}). Hence we can write

$$\rho(T) = \rho_0 + \rho_{ph}(T) + \rho_{mag}(T) \qquad (4.1)$$

In the strong scattering regime, near the Anderson localization, the Boltzmann formalism breaks down and so is the Matthiessen's rule. This is one of the reasons for concentrating on the higher temperature region where we apply Eq. (4.1) above the resistivity minima, if present. To estimate the magnetic contribution to the resistivity from the measured ρ(T), we have subtracted the ($\rho_0 + \rho_{ph}$) term from the total resistivity and assumed the validity of Matthiessen's rule. Taking the standard Bloch-Wilson formula[4] for ρ_{ph} in the case of transition metals and their alloys, the expression for ρ(T) becomes

$$\rho(T) = \rho_0 + A\left(\frac{T}{\theta_D}\right)^3 \int_0^{\theta_D/T} \frac{z^3}{(1-e^{-z})(e^z-1)} dz + \rho_{mag} \qquad (4.2)$$

where ρ_0 and A are temperature-independent constants and θ_D is the Debye temperature. Generally, both in ρ_{ph} and ρ_{mag}, the scattering may take place within a single band (s-s) or may involve s-d transitions. ρ_{ph} (T) goes as T^3 at low temperatures and as T above θ_D.

According to Rivier and Adkins[5] for spin-glass systems $\rho_{mag} \sim T^{3/2}$ below the freezing temperature (T_f) but Fisher[6] found a magnetic contribution of the form BT^2-$CT^{5/2}$ below T_f with constants B and C > 0. He also concluded that the $T^{3/2}$ variation is due to ferromagnetically ordered spins in a spin glass. Thus ρ(T) takes the following two different forms due to ρ_{mag} predicted by the above two theories:

$$\rho(T) = \rho_0 + A\ (\frac{T}{\theta_D})^3 \int_0^{\theta_D/T} \frac{z^3}{(1-e^{-z})(e^z-1)} + BT^{3/2} \qquad (4.3)$$

and

$$\rho(T) = \rho_0 + A\ (\frac{T}{\theta_D})^3 \int_0^{\theta_D/T} \frac{z^3}{(1-e^{-z})(e^z-1)} dz\ + BT^2 - CT^{5/2} \qquad (4.4)$$

Based on the spin-wave dispersion relation $E_q = Dq^2$, Kasuya[7] had given the following expression for the spin-disorder resistivity for ferromagnetic metals:

$$\rho_{mag}(T) = \frac{\pi^3 VmG_{s-d}^2}{8Ne^2\eta E_F}(g-1)^2\ j\ (\frac{kT}{k_F^2 D})^2 \qquad (4.5)$$

where G_{s-d} is a parameter which describes the strength of the s-d interaction, g is the Landé factor, j is the total angular momentum quantum number of each magnetic atom, E_F is the Fermi energy of the conduction electrons, D is the spin-wave stiffness constant, and V and N are the volume and the number of atoms in the crystal, respectively. A similar result was obtained using a slightly different method by Mannari[8]. He estimated ρ_{mag} for Ni and found excellent agreement with the measurements of White and Woods[9] for the case of Fe, Co, and Ni [where ρ = (13-16) x 10^{-6} T^2 Ω cm] in the low–temperature range. Therefore in ferromagnets, the resistivity of the system can be written as

$$\rho(T) = \rho_0 + A\ (\frac{T}{\theta_D})^3 \int_0^{\theta_D/T} \frac{z^3}{(1-e^{-z})(e^z-1)} dz\ + BT^2 \qquad (4.6)$$

The resistance of an electrical conductor has been found to either increase (positive magnetoresistance) or decrease (negative magnetoresistance) in the presence of a magnetic field. Theoretical models of the positive and negative magnetoresistance relevant to the present work are briefly described below.

Normal magnetoresiatance: The normal positive magnetoresistance is inherent in all systems having free electrons. Theories based on the free-electron model lead to a zero magnetoresistance. A two-band model[10] consisting of two overlapping bands of s and d electrons was therefore proposed. In this model the transverse magnetoresistance, in small magnetic fields *H*, is given by,

$$(\frac{\Delta\rho}{\rho})_n = 1/2ne(\frac{H}{\rho})^2 \qquad (4.7)$$

where $\left(\frac{\Delta\rho}{\rho}\right)_n$ is called the "normal magnetoresistance," ρ being the electrical resistivity in zero magnetic fields, n is the number of electrons per unit volume, and e is the electronic charge. The above expression is in fairly good agreement with the experimental results.

Negative magnetoresistance: Béal-Monod and Weiner[11] calculated the negative magnetoresistivity of dilute alloys containing transition-metal impurities and exhibiting Kondo resistance anomaly. Their calculations were based on a third-order perturbation expansion of the s-d exchange Hamiltonian. The calculation of the conduction-electron scattering amplitude, in the zero-field limit, yielded the famous Kondo logarithmic temperature dependence. The theory of Bẻal-Monod and Weiner is restricted to alloy systems in which the spins are isolated and hence the spin correlations of the magnetic impurities were ignored.

4.4 Experimental details

The Ni-Mn alloy preparation was described earlier in details in Chapter III, Section 3.3 and structural properties in Section 3.4.1. A four-probe AC method was used for measuring the electrical resistivity in the temperature range 5-350 K using Quantum Design's Physical Property Measurement System (PPMS-6500) with an 8 T superconducting magnet. The electrical contacts were spot welded to the sample. The sample current was ~ 100 mA at a frequency of 133 Hz. Data were taken at 1 K interval or less in the whole temperature region and at fixed fields till 8

T. A typical sample used for resistivity measurements has l (distance between voltage probes) = (0.134 ± 0.001) cm, b (breadth) = (0.246 ± 0.001) cm, and t (thickness) = (0.073 ± 0.001) cm. In this system the experimental resolution (ΔR/R) of resistance is ~ 1 in 10^5. However, the error in the resistivity due to uncertainties in the measurements of geometrical factors of the samples is ~ 3 %.

4.5 Results and discussion

4.5.1 Magnetic *phase of Ni-Mn alloys*

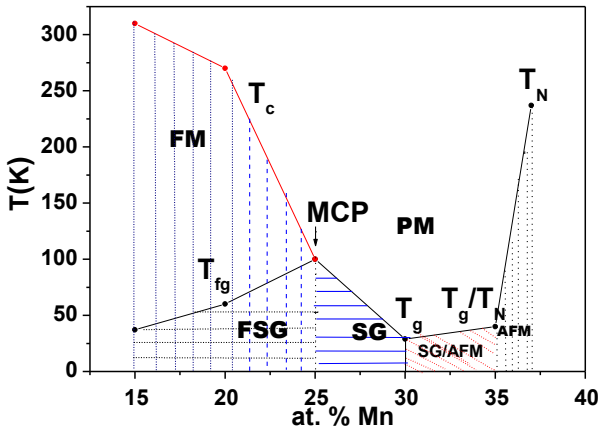

Fig.4.1 Magnetic phase diagram (temperature vs. composition) of disordered $Ni_{1-x}Mn_x$ alloys ($15 \leq x \leq 37$).

Extensive ac-susceptibility χ (T) and detailed DC magnetization measurements have been done under various field-cooling conditions to establish the magnetic phases of disordered $Ni_{100-x}Mn_x$ system over a wide concentration range ($15 \leq x \leq 37$) encompassing the critical concentration ($x \sim 25$)[1]. The resulting magnetic phase diagram is presented in Fig. 4.1. For the samples below x = 25 at. % of Mn, we find a double transition, one from a paramagnetic to a ferromagnetic long range order (LRO) state at the Curie temperature T_C and then another to a

ferro-spin-glass mixed phase at T_{fg}. Through the de Almeida-Thouless (AT) plot and the field-independent points of inflection in M (T), we further establish the glass-transition temperature T_{fg} of the multicritical point (MCP) to be ~ 100 K for the alloy at x = 25. The values of the Curie temperature (T_C) and the saturation magnetization are found to decrease with increasing Mn concentration and meet the ascending line of T_{fg} at the multicritical point. For the alloys with x = 30 and 35, a conventional/canonical spin-glass along with short range antiferromagnetic state appears which gradually evolves to an antiferromagnetic state in the intermediate region of composition, and then an antiferromagnetic LRO around 37 at. % Mn.

4.5.2 General features of the experimentally observed $\rho(T)$

We are presenting in Fig. 4.2 high-resolution AC resistivity data for $Ni_{100-x}Mn_x$ ($15 \leq x \leq 37$) alloys between 5 and 350 K. Distinct minima have been observed for all the alloys above the critical composition (x ~ 25) but none below it except for a kink around the freezing temperature. The resistivity curve of the multicritical composition neither gives minima nor any kink but a point of inflection around the multicritical point (T = 100 K). The values of resistivity at 5 and 300 K, $T_{min.}$, temperature coefficient of resistivity, TCR [$= \rho^{-1}(d\rho/dT)$] at 100 K, DOM (Depth of minima), total change in resistivity $\Delta\rho$ ($\Delta\rho = \rho_{300K} - \rho_{min.}$, where $\rho_{min.}$ = resistivity at $T_{min.}$), and $\Delta\rho/\rho_{300K}$ are all calculated from the data and are given in Table 4.1 along with the relevant transition temperatures. The high values of the electrical resistivity at 5 K imply strong disorder in these alloys. We see that DOM and $\Delta\rho/\rho_{300K}$ decreases whereas ρ increases as we move towards higher Mn concentration.

We see that T_{min} is almost constant (33, 36, and 36 K) and DOM's are about 0.2 % with no systematic dependence on the value of the resistivity. This is due to the fact that the variation in the resistivity with temperature in the present series is found to be small ~ 5 μΩcm, compared to that for concentrated CuMn alloys (say, $Cu_{64}Mn_{36}$) which also has spin-glass characteristics with antiferromagnetic short range order[12] where it is about 10 μΩcm.

Table 4.1: Mn concentration (x) dependence of magnetic transition temperatures (T_C, T_{fg}, T_g, T_N), resistivities ρ at 5 and 300 K, $T_{min.}$, TCR [$\rho^{-1}(d\rho/dT)$] at 100 K, DOM, and $\Delta\rho/\rho_{300K}$ of γ-$Ni_{100-x}Mn_x$ ($15 \leq x \geq 37$) alloys.

Alloy composition (x)	T_c (K)	T_{fg} / T_g/ T_N (K)	ρ_{5K} μΩcm	ρ_{300K} μΩcm	T_{min} (K)	TCR $\rho^{-1}(d\rho/dT)$ ($\times 10^{-4}$/K)	Depth of minima (%)	$\Delta\rho/\rho_{300K}$ (%)
15	311	37	86	147	-		-	-
20	270	60	101	133	-		-	-
25	100	100	128	148	-		-	-
30	-	29	144	147	33	1.5	0.20	2.0
35	-	40	149	153	36	2.0	0.23	3.3
37	-	237	183	188	36	2.5	0.22	3.1

4.2(a)

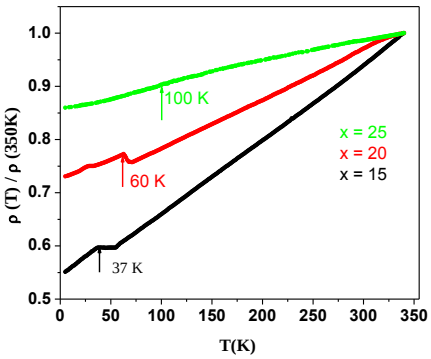

4.2(b)

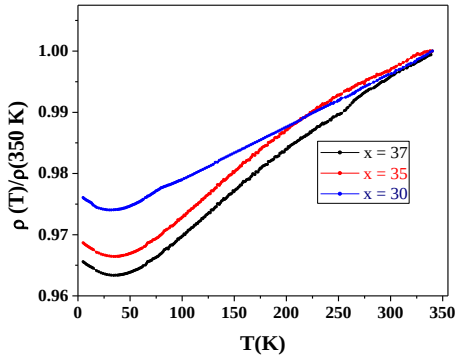

4.2(c)

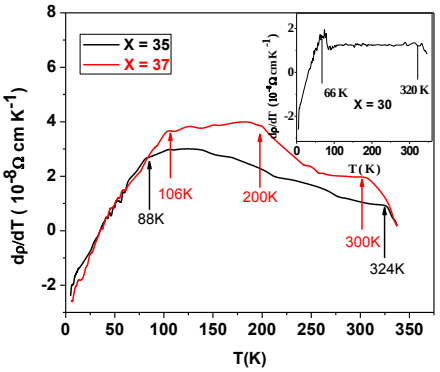

Fig.4.2 Experimental ρ(T) plot of $Ni_{100-x}Mnx$ alloys (a) x = 15, 20, and 25 (b) x = 30, 35, and 37, and (c) dρ/dT vs. T for x = 35 and 37 (inset for x = 30), all from 5 to 350 K.

From the ρ(T) curves of Fig. 4.2, the following observations could be made:

i) There are distinct signatures of magnetic transitions around their T_{fg} (for x = 15 and 20) and at $T_{fg}/T_C/T_g$ for x = 25. The ρ(T) data for alloys with x = 15 and 20 (Fig. 4.2(a)) show distinct kinks around 37 and 60 K, respectively. It is to be noted from Table 4.1 that the ferro-spin-glass transition temperatures T_{fg} of these alloy are 37 and 60 K, respectively which we had obtained from earlier magnetic measurements[1]. The variation of ρ(T) is quite linear with temperature beyond T_{fg}. For x = 25 (which is the multicritical composition) we get no kink but a point of inflection at $T_{fg} = T_C = T_g \sim 100$ K indicating a change of phase. For x = 15, 20, and 25, the linearity in ρ(T) continues till 350 K (the highest temperature of measurements) indicating no saturation effects. The above notable discontinuities/point of inflection around the transition temperatures are closely connected to the magnetic transitions in these alloys. The scattering due to disorder decreases when the magnetic phase changes from the spin-glass state to the ordered ferromagnetic state. The kinks around ferro-spin-glass transitions, showing a drop in the resistivity, indicate a large decrease in the spin-disorder scattering. This is also compatible with our dc magnetic measurements. According to the data in the literature[13], it follows that the temperature dependence of the electrical resistivity for ferromagnetic alloys shows a discontinuity that corresponds approximately to their transition temperatures. *Thus the magnetic phase transitions show up very nicely in electrical transport measurements as well.*

(ii) The ρ(T) curves for x = 30, 35, 37 (Fig. 4.2(b)) start deviating from linearity (slower than linear) roughly beyond 100 K ($\approx \Theta_D/3$). This behavior manifests itself in the dρ/dT vs. T plots as well (Fig. 4.2(c)).

(iii) From Figs. 4.2(a) and 4.2(b), it can be seen that $\Delta\rho/\rho_{300K}$ at 5 K increases with x as expected.

(iv) To get an overall view of the temperature dependence of the resistivity, the temperature derivative dρ/dT has been found from T_{min} (~ 36 K) to 350 K. There are two changes in slope in dρ/dT curves for the alloys with x = 30 (inset of Fig. 4.2 (c)) and 35 (Fig. 4.2 (c)), one at 66 and 88 K and another at 320 and 324 K, respectively. However, for x = 37, we have three changes in slope at 106, 200, and 300 K, respectively as shown in Fig. 4.2 (c). The lower temperature change of slope indicates that ρ changes from a non-linear (actually quadratic which is a transition region between T^3 and T in Bloch-Wilson formula[4] for ρ_{ph} as analyzed below to a linear (electron-phonon scattering) variation with T. The second change of slope at higher temperatures where it drastically reduces with T is an indication for a tendency for the electrical resistivity to saturate (slower than linear in T). This is often observed in high resistivity alloys[14] with ρ ≥ 150 μΩcm where thermal and compositional disorders become equally important for resistivity saturation. The temperature coefficient of resistivity TCR (= $\rho^{-1}d\rho/dT$) for the alloys with x = 30, 35, and 37 are, respectively (0.59, 0.11, and 0.09) x 10^{-4}/K. These are comparable with the extrapolated values of TCR of Fig. 4 of reference 12 for FeNiCr alloys of similar values of ρ. Most likely, the additional change of slope for x = 37 is just an indication of resistivity saturation as early as 200 K.

4.5.3. Analysis of the $\rho(T)$ data for samples with x=30, 35, and 37

(a) ρ(T) below T_{min}/2

This region covers the resistivity well below the minima at T_{min}. The low temperature resistivity minima is generally explained in terms of Kondo effect where ρ(T) is given by

$$\rho(T) = \rho_0 - m \ln (T). \qquad (4.8)$$

The Kondo minima have some salient features as:

i) The minima disappear in the presence of magnetic fields, ii) Usually these minima appear in very dilute, low resistive alloys, and iii) T_{min} depends on the impurity concentration and the magnetic state of the alloys.

However, our disordered Ni-Mn alloys satisfy none of the above three criteria since the minima do not disappear in magnetic fields, all the three alloys are highly resistive (~140-180 μΩcm), and T_{min} (~ 36 K) does not depend on the concentration of Mn as well their magnetic state (spin-glass or antiferromagnetic). So, Kondo effect could be easily ruled out here. Hence to interpret the minima in these disordered alloys we use the theory of Altshuler and Aranov[15] wherein electron-electron interaction effects in the presence of weak localization can explain the increase in resistivity with decreasing temperature for $T << T_{min.}$. The basic idea behind this theory is that electrons in disordered alloys (where electron mean free path is of the order of interatomic distance) do not follow the classical Boltzmann trajectories. More likely, they diffuse from site to site with multiple elastic scattering. This leads to a phase coherence between the electron's counter-propagating partial waves which, in turn, enhances the probability for an electron to return to its starting point. Thus the electrons get localized and the resistivity increases. Now, this phase coherence could be destroyed by inelastic scattering, magnetic fields, and electron-electron (e-e) interaction effects and thus the additional resistivity reduces. The electrical conductivity due to e-e interaction is given by Lee and Ramakrishnan[16] as

$$\sigma(T) = \sigma_{0+} m_\sigma \sqrt{T}, \qquad (4.9)$$

where m_σ contains the screening constant for Coulomb interaction F_σ and the diffusion constant D. Equation (4.9) in terms of resistivity can be written as

$$\rho(T) = \rho_{0+} m_\rho \sqrt{T}, \qquad (4.10)$$

where it is assumed that that $m_\sigma \rho_0 \sqrt{T} << 1$ and $m_\rho = - m_\sigma \rho_0^2$.

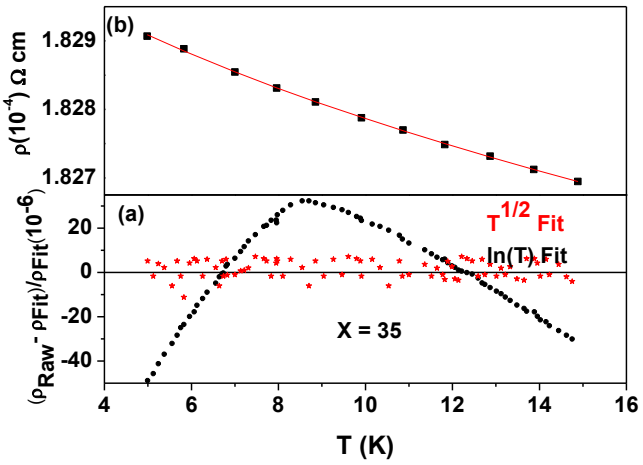

Fig.4.3 For the alloy with x = 35 (a) the residuals vs. temperature for fitting the data to $T^{1/2}$ and ln (T) and (b) resistivity data (shown every 1 K only) along with the best fit to $T^{1/2}$, in the temperature range 5-15 K.

Fig. 4.3(b) is a plot of the resistivity data along with the best-fit to $T^{1/2}$ from 5 to 15 K although we have fitted our data to both Eqs. (4.8) and (4.10). They show two distinct features. Firstly, the values of the normalized χ^2 for the fits to Eq. (4.8) (~ 10^{-8}) are found to be an order of magnitude higher than that to Eq. (4.10) (~ 10^{-9}), the experimental resolution being 1 part in 10^5. Secondly, the plot of $(\rho_{Raw}-\rho_{Fit})/\rho_{Fit}$ vs. temperature for the $T^{1/2}$ fit is found to be random whereas that for the ln (T) fit shows a systematic trend. A typical plot of the temperature dependence of the residuals is shown for the alloy with x = 35 in Fig. 4.3(a). It is clearly seen that in this region ρ(T) data are much better described by the $T^{1/2}$ dependence (correlation coefficients better than 0.999).

The values of m_ρ, the coefficient of the $\sqrt{T}$ term, are found in the range - (8-13)×10^{-2} $\mu\Omega cmK^{-1/2}$ and are of the same order - (8-15)×10^{-2} $\mu\Omega cmK^{-1/2}$ as found in $Cu_{100-x}Mn_x$ (x = 60, 73, 76, and 83) alloys showing similar resistivity minima[17].

Again, as shown in Fig. 4.4, the data for x = 37 between 5 and 15 K (well below T_{min} = 36 K) also give an excellent fit to Eq. (4.10), i.e., $\rho(T) \sim -\sqrt{T}$ with a correlation coefficient of 0.9996 and a normalized χ^2 of ~ 10^{-9}. Thus the $\sqrt{T}$ dependence of resistivity strongly establishes the electron-electron interaction effects in this temperature region. Table 4.2 gives the values of the best-fitted parameters and the corresponding values of χ^2 for both the fits ($-\sqrt{T}$ and – ln (T)).

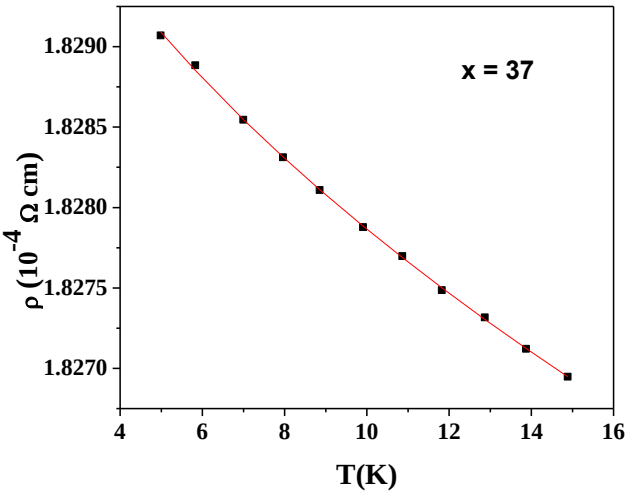

Fig.4.4 Resistivity vs. temperature data (5 – 15 K, well below minimum of 36 K) for the alloy with x = 37 in zero fields and the best fit to $\rho(T) = \rho_0 + m_\rho\sqrt{T}$.

Table 4.2: Sample composition, values of the best-fitted parameters, and the corresponding χ^2 for both the fits to Eqs. (4.10) and (4.8) from 5 to 15 K.

$Ni_{100-x}Mn_x$ x at. %	$\rho(T) = \rho_0 + m_\rho\sqrt{T}$			$\rho(T) = \rho_0 - m\ln T$		
	ρ_0 ($\mu\Omega$cm)	m_ρ ($\mu\Omega$cm $K^{-1/2}$) 10^{-2}	χ^2 10^{-9}	ρ_0 ($\mu\Omega$cm)	m ($\mu\Omega$cm $K^{-1/2}$) 10^{-2}	χ^2 10^{-8}
30	140	-08	2.3	140	20	4.3
35	149	-10	3.2	150	33	4.7
37	180	-13	2.6	180	17	4.5

(b) $T_{min}/2 \leq \rho(T) \leq 2T_{min}$

In this temperature range we have e-e interaction effects as well as different inelastic and magnetic scattering processes competing to give rise to the resistivity minima. For these compositions, the alloys pass from a spin-glass to an antiferromagnetic phase. Hence some magnetic contribution is expected. Besides this, the usual electron-phonon scattering will have their low-temperature contribution to the resistivity. We have satisfactorily fitted our data taking Bloch-Wilson formula[4] for ρ_{ph} as given by the second term of Eq. (4.2) and the e-e interaction effects given by Eq. (4.10). The coefficients of the interaction term (m_ρ) lies in the range (13 – 16) x 10^{-2} $\mu\Omega cmK^{-1/2}$ (x = 30, 35, and 37) in the temperature range 16-64 K and the calculated values of m_σ [$m_\rho = - m_\sigma\rho_0^2$] are 62, 65, and 49 $(\Omega cmK^{1/2})^{-1}$ for x = 30, 35, and 37 respectively. These are almost an order of magnitude larger than the near-universal value of 6 $(\Omega cmK^{1/2})^{-1}$. However, somewhat similar values were also found in an earlier study[18]. The coefficient of the low-temperature phonon term is of the order of 10 $\mu\Omega$cm in agreement with another similar system[12] $Cu_{100-x}Mn_x$. However, if the resistivity minima were due to Kondo effect, we tried that fit as well by replacing Eq. (4.10) by Eq. (4.8) but the fits are much inferior providing further

evidence in favor of e-e interaction effects as the most probable mechanism for the occurrence of resistivity minima. The value of normalized χ^2 is of the order of 10^{-9} which is consistent with our experimental resolution of $\Delta R/R \sim 10^{-5}$. All the fitting parameters, temperature range of the above fits, and the values of χ^2 are given in Table 4.3. Here we observe that with increase in Mn concentration the residual resistivity increases ((145-183) μΩcm) but the Debye temperature has no systematic dependence on concentration**.** Figure 4.5 shows the data along with the best-fitted graph of $\rho(T)$ to $\rho_0 + \rho_{ph} + m_\rho\sqrt{T}$ for x = 35 in the temperature range 16-64 K. The high resolution of the data makes the depth of minimum (only ~ 0.2 %) so prominent.

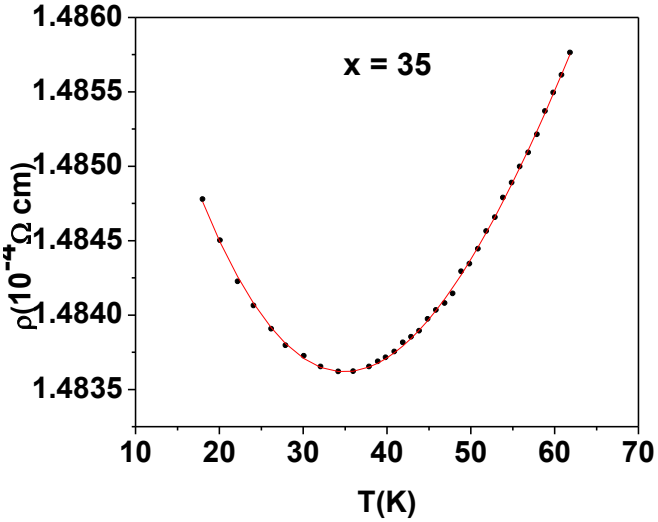

Fig.4.5 The data along with the best fit of $\rho(T)$ to $\rho_0 + \rho_{ph} + m_\rho\sqrt{T}$ are shown for x = 35 in the temperature range 16-64 K.

Table 4.3: Composition, range of fit, best-fitted parameters ρ_0, Θ_D, A, and m_ρ and χ^2 for fits to $\rho_0 + \rho_{ph} + m_\rho\sqrt{T}$.

% of Mn (x)	Fit range (K)	ρ_0 ($\mu\Omega$cm)	Debye Temp Θ_D (K)	A ($\mu\Omega$cm)	m_ρ ($\mu\Omega$cm $K^{-1/2}$) 10^{-2}	m_ρ/ρ_0^2 $(\Omega cmK^{1/2})^{-1}$	χ^2
30	16-64	145	352	08	-13.0	62	2.7E-9
35	16-64	149	304	14	-14.6	65	1.4E-9
37	16-64	183	340	21	-16.4	49	1.5E-9

(c) Resistivity well above the minima ($\rho(T) \geq 65$ K)

The two features, namely the shape of $\rho(T)$ curve and the occurrence of maxima in $d\rho/dT$, give indications of possible magnetic contributions to the electrical resistivity. In this temperature range of 65-300 K, the linear temperature dependence is ascribed to the high temperature electron-phonon scattering for x = 30 and 35 where $\rho(T) = \rho_0 + \rho_{ph}$. The presence of only the phonon term in the resistivity in this range (65-300 K) is quite reasonable because T_g and T_N are only around 30-40 K. One does not expect magnetic contribution in this range of temperature. Very good fits of the resistivity data of alloys with x = 30 and 35 have been obtained. But for the alloy x = 37, we expect magnetic contributions along with that of phonons

because T_N ~ 240 K. Masharov[19], considering scattering of conduction electrons by both localized and itinerant electrons, found that $\rho_{antiferro}(T) = B_1 T^2$ with B_1 of the order of $10^{-5}\mu\Omega cmK^{-2}$. The Debye temperature (θ_D) for these alloys is around ~ 340 K and the mean temperature of this range of 65-300 K is ~ $\theta_D/2$. Hence, $\rho(T)$ can be written as $\rho_0 + \rho_{ph} + B_1 T^2$, where B_1 is as defined above. Fitting the data for x = 37 is found to be very satisfactory with normalized mean-squared deviation χ^2 consistent with the experimental accuracy. We have defined normalized χ^2 as

$$\chi^2 = \frac{1}{N}\sum_{i=1}^{N}\frac{(\rho_{imeasured} - \rho_{ifitted})^2}{\rho_{mean}^2}$$

where N is the number of data points, $\rho_{measured}$, ρ_{fitted}, and ρ_{mean} are the measured, fitted, and the mean of the measured values of the resistivity, respectively. The values of the parameters and χ^2 along with their range of fits are given in Table 4.4. The coefficient of the T^2 term (B_1) comes out of the same order as that of the theoretical prediction[19] of $10^{-5}\ \mu\Omega cmK^{-2}$. However, no such magnetic contributions (~T^2) was found for x = 30 and 35.

Figures 4.6 (a), (b), and (c) show the best-fitted graphs of ρ (T) to $\rho_0 + \rho_{ph}$ or $\rho_0 + \rho_{ph} + B_1T^2$, for x = 30, 35, and 37, respectively in the temperature range 65-300 K.

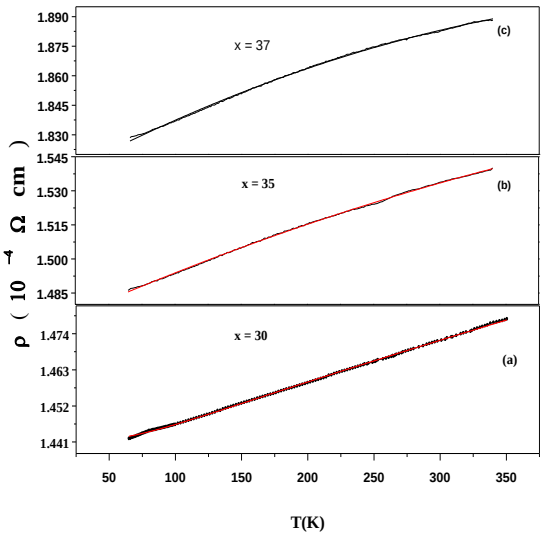

Fig. 4.6 (a), (b), and (c) The data along with the best fits of ρ (T) to $\rho_0 + \rho_{ph}$ for x = 30 and 35 and to $\rho_0 + \rho_{ph} + B_1T^2$, for x =37, respectively in the temperature range 65-300 K.

Table 4.4: Composition, fit functions, range of fit, best-fitted parameters A, B_1, and the values of the normalized χ^2.

% of Mn (x)	Fit function	Fit range (K)	A Coefficient of phonon term (μΩ cm)	B_1 $(\mu\Omega cmK^{-2})10^{-6}$	χ^2 (10^{-9})
30	$\rho(T) = \rho_0 + \rho_{ph}$	65-350	11	-	2.9
35	$\rho(T) = \rho_0 + \rho_{ph}$	65-350	11	-	3.7
37	$\rho(T) = \rho_0 + \rho_{ph} + B_1T^2$	65-350	9	11	2.5

4.5.4. Analysis of $\rho(T)$ data for samples with x = 15, 20, and 25

(a) $T < T_{fg}$

Due to exchange interaction between the host conduction electrons and the spins of the magnetic impurities, the resistivity of spin glasses at low temperatures ($T < T_{fg}$) varies as $A+BT^2-CT^{5/2}$ with all positive coefficients[6]. The coefficient B signifies the ferromagnetic contribution whereas the last term ($CT^{5/2}$) is due to coexisting spin-glass character. Figure 4.7 shows ρ (T) data along with the best-fitted graphs to $\rho(T) = A+BT^2-CT^{5/2}$ for the three samples with x = 15, 20, and 25 below T_{fg}. Composition, best-fitted parameters A, B, C, and the values of normalized χ^2 and correlation coefficient R^2 are given in Table 4.5. Here we find that the values of both the coefficients B and C decrease with increasing concentration of Mn. However, the overall change in resistivity is ~ 5-10 % for 25-50 K change of temperature with no systematic composition dependence.

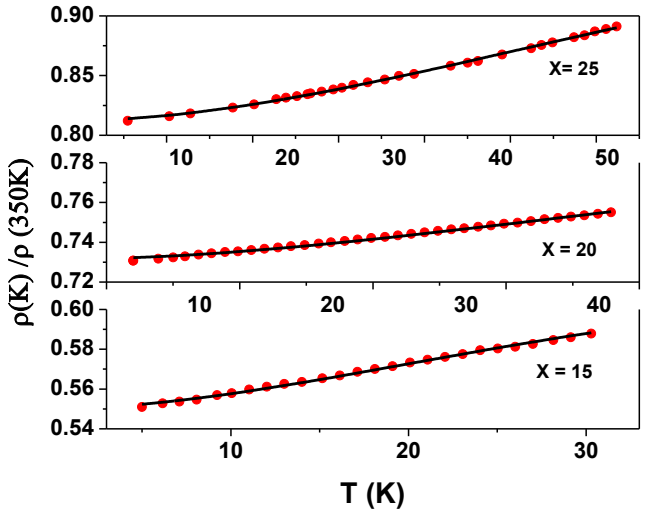

Fig. 4.7 ρ (T) data along with the best fit to Eq. $\rho(T)=A+BT^2-CT^{5/2}$ for the three samples with x = 15, 20, and 25 below T_{fg}.

Table 4.5: Composition, best-fitted parameters A, B, C, and the values of normalized χ^2 and correlation coefficient R^2.

Mn %	A ($\mu\Omega$cm)	$Bx10^{-5}$ ($\mu\Omega cmK^{-2}$)	$Cx10^{-5}$ ($\mu\Omega cmK^{-2.5}$)	χ^2	R^2
15	0.5506±0.0002	12±0.5	1±0.1	9.33E-8	0.9993
20	0.7310±0.0002	4.0±0.2	0.43±0.01	1.69E-7	0.9982
25	0.8600±0.0001	1.0±0.1	0.12±0.01	2.93E-8	0.9988

(b) T well above T_{fg}

From Table 4.1 we see that these samples are all ferromagnetic with co-existing ferro-spin-glass mixed phase. In Fig. 4.2(a) we have already shown their resistivity vs. temperature plots in zero fields. The electrical resistivity in these alloys has contributions from static disorder, electron-phonon scattering, and magnetic scattering and is given in theory by Eq. (4.1), where $\rho_{mag}(T) = BT^2$ for s-s scattering and ρ_{mag} (s-d) has no tractable T-dependence[13]. Figure 4.8 shows the data along with the best fits to Eq. (4.1) for the three samples. All the fitting parameters and the fit characteristics are given in Table 4.6.

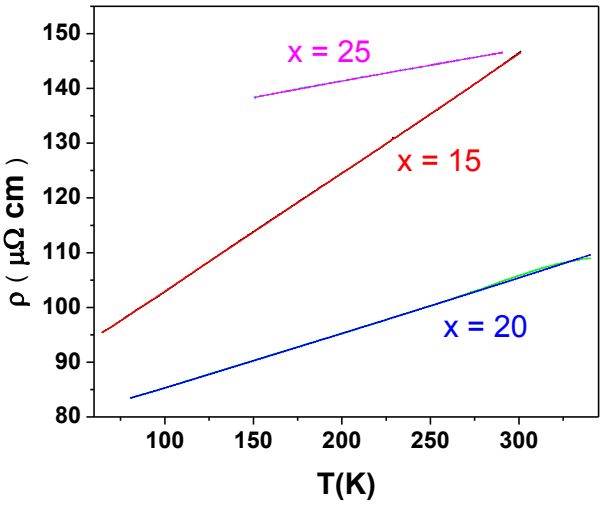

Fig.4.8 ρ (T) data along with the best fits to Eq. (4.1) for the three samples with x = 15, 20, and 25.

Table 4.6: Composition, fit functions, range of fit, best-fitted parameters ρ_0, Θ_D, A, B, and the values of correlation coefficient R^2 and normalized χ^2.

% of Mn (x)	Fit function	Fit range (K)	ρ_0 (μΩ cm)	Debye Temp. Θ_D (K)	A (μΩcm)	B (μΩcmK^{-2}) 10^{-6}	R^2	χ^2 10^{-9}
15	$\rho(T) = \rho_0 + \rho_{ph} + BT^2$	65-300	86	485	83	64	0.99973	42
20	$\rho(T) = \rho_0 + \rho_{ph} + BT^2$	80-300	98	346	54	34	0.99973	4.6
25	$\rho(T) = \rho_0 + \rho_{ph}$	150-300	128	226	40	-	0.99952	0.14

It is seen from Table 4.6 that for the two ferro-spin-glass alloys (x = 15 and 20), ρ(T) has some magnetic contributions as well but for the one at the MCP (x = 25) we have found none. Also, B, the magnetic scattering strength (s-d scattering at higher temperatures), decreases with x, i.e., ferromagnetism is gradually weakening with increasing Mn. Moreover, the fit has become significantly better for x = 25 since the latter, above 100 K, has contributions only from phonons.

The most interesting conclusion is that the strength of the electron-phonon interaction, A (Tables 4.4 & 4.6) decreases from 83 to 9 μΩcm as the Mn content increases. Correspondingly [ρ (~ 340 K) - ρ (~ 65 K)]/ρ (~ 65 K), a measure of the electron-phonon scattering above 65 K also decreases from 54 to 3 %.

4.6 *Magnetoresistance*

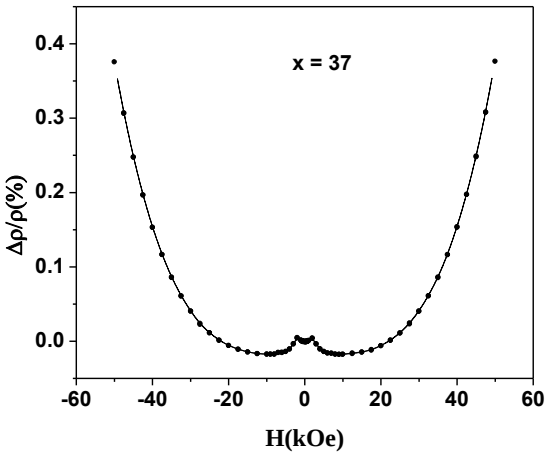

Fig.4.9 Resistivity vs. applied magnetic fields for sample with x = 37 at 5 K and up to 50 kOe.

Figure 4.9 is a plot of the resistivity vs. applied magnetic fields for sample with x = 37 at 5 K (well below the resistivity minimum) and up to 50 kOe. We observe a positive transverse MR varying much faster than B^2, more like B^4 and ~ 0.36 % at 50 kOe. This positive MR provides further evidence for the electron-electron interaction effects at the lowest temperatures using which we interpreted the resistivity minima data. The other two samples also having resistivity minima, x = 35 and 30, show positive MR ~ B^n with n ~ 3.5 and 3, respectively with MR ~ 0.27 and 0.17 %.

The butterfly-kind of structure in MR vs. H at low fields, viz., first a positive MR till ~ 1 kOe (< 0.01 %), then a negative MR till 5 kOe (magnitude < 0.03 %), and finally a sizable positive MR at high fields, has also been observed for the other two samples as well (x = 30, 35; plots not shown). But this low-field(< 5 kOe) butterfly-kind of structure of the MR is not very clear. However, this could be due to the low-field positive MR predicted for antiferromagnets by Yamada and Takada[20]. They argue that when the magnetic field is parallel to the sublattice magnetization it might reduce spin fluctuations in one sublattice and enhance it in the other, the sum total producing a positive MR. When the magnetic field is normal to the sublattice magnetization, the MR is zero. So for polycrystalline samples like the present ones, as the field increases, the MR could change from positive to zero and then finally to negative. To summarize, all the samples above the critical composition (x = 25) have a positive MR as expected in polycrystalline metallic antiferromagnetic systems[21] showing evidence of e-e interaction.

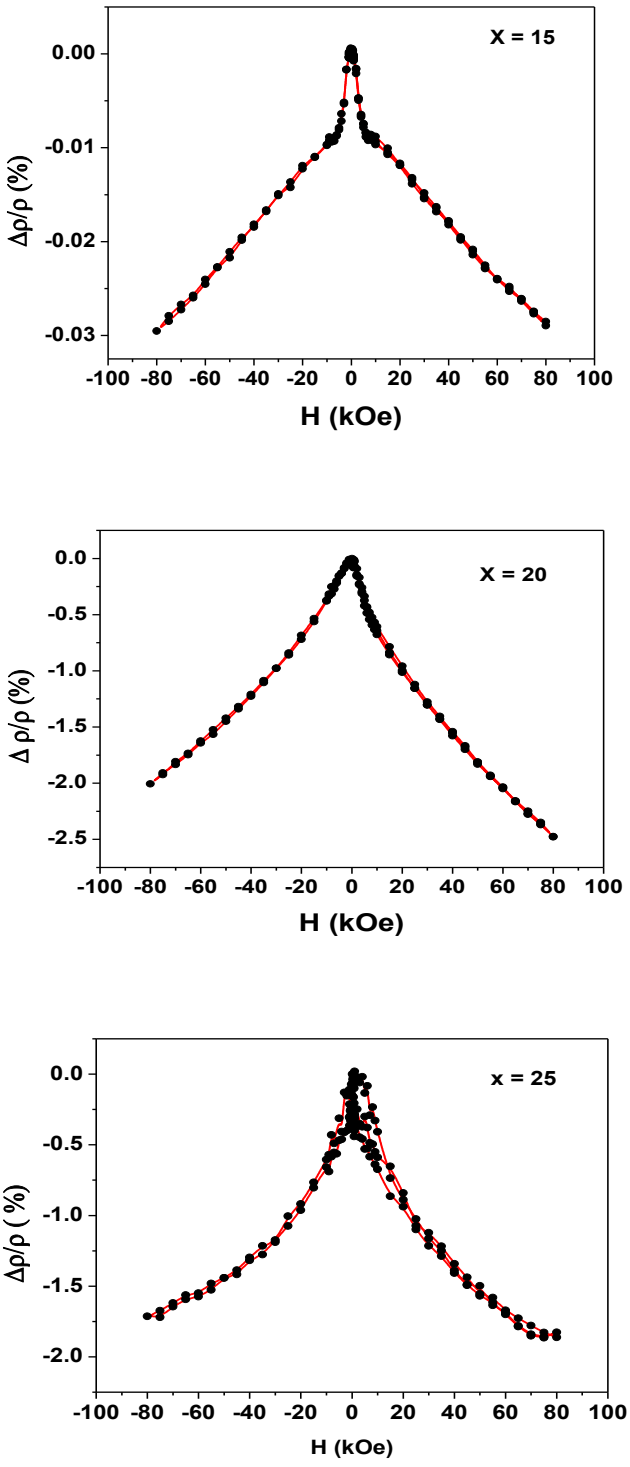

Fig. 4.10 (a) - (c) Plots of resistivity vs. magnetic fields at 5 K for alloys with x = 15, 20, and 25.

There is a distinct difference in the behavior of MR above and below the MCP (x = 25). It is positive above and negative below. All the alloys (x = 15, 20, and 25) exhibit a negative transverse magnetoresistance (MR) in the temperature range of measurement (5 – 300 K) and shown in Fig. 4.10 (a)-(c) at 5 K. The magnitude of the MR decreases with increasing Mn concentration, say at 5 K and 80 kOe, it is 3.0 % for $Ni_{85}Mn_{15,}$ 2.3 % for $Ni_{85}Mn_{15}$, and 1.25 % for $Ni_{75}Mn_{25}$. Figure 4.10(a) shows that there is a sharp low-field negative MR at 5 K for x = 15 (T_C ~ 310 K) till about 5 kOe (~ saturation field of pure Ni) due the ferromagnetic anisotropy of resistance (FAR) (from spin-orbit interaction in ferromagnets). The negative MR beyond 5 kOe varies almost linearly with H till the highest fields. The physics behind this negative MR is due to less electron-magnon scattering at higher fields since some magnons are quenched by the Zeeman term in the magnon dispersion relation. At 300 K, the initial drop in TMR at 5 K due to FAR almost disappears because 300 K is just below its T_C. For x = 20, 300 K is above its T_C of 270 K and the initial drop at 5 K disappears completely. For x = 25 (T_C ~ 100 K), the negative TMR of 1.25 % at 5 K understandably disappears (< 0.1 %) at 300 K since there are no magnons anyway for $T >> T_C$.

4.7 Conclusions

The interpretation of the electrical transport and the magnetic phases complement each other to a large extent. It is seen from the temperature dependence of resistivity that ρ(T) exhibits distinctly different behavior below and above the multi-critical point (MCP) x = 25.

i) In the SG/AFM regime (x ≥ 25) resistivity minima show up due to larger disorder with resistivity ~ (145-180) μΩcm. Here ρ(T) is analyzed in terms of electron-electron interaction

effects (~ - C$\sqrt{T}$) and electron-phonon s-d scattering. The minima are ascribed to electron-electron interactions. The value of the coefficient C is similar to those found in systems showing resistivity minima due to quantum interference effects.

ii) In the FM/FSG ($x \leq 25$) phase $\rho(T)$ is dominated by spin-glass contributions at low temperatures and large electron-phonon and electron-magnon s-d scattering at higher temperatures. The magnetic term B (s-d) ~ 50 $\mu\Omega cmK^{-2}$ is 3 times as large as that of pure Ni (13-16) $\mu\Omega cmK^{-2}$. This is not surprising since the magnetic contribution in Ni is from s-s electron-magnon scattering for $T < 10$ K whereas our range of fit was typically 70-300 K where s-d electron-magnon scattering is much more dominant.

iii) Finally, the MR of the alloys with $x \leq 25$ is negative whereas those for $x \geq 25$ are positive. They are governed by different mechanisms.

Bibliography

1. Pampa Pal, Rudra Banerjee, Radheshyam Banerjee, Abhijit Mookerjee, Gopi Chandra Kaphle, Biplab Sanyal, J. Hellsvik, Olle Eriksson, P. Mitra, A. K. Majumdar, and A. K. Nigam, Phys. Rev. **85**, 174405 (2012).

2. A. Mookerjee and S. B. Roy, Pramana **14,** 11 (1980).

3. M. Gabay and G. Toulouse, Phys. Rev. Lett. **47,** 201 (1981).

4. A. H. Wilson, Proc. R. Soc. London A **167**, 580 (1938).

5. N. Rivier and K. Adkins, J. Phys. F: Metal Phys. **5,** 1745 (1975).

6. K. H. Fisher, Z. Phys. **B 34**, 45 (1979).

7. T. Kasuya, Prog. Theor. Phys. (Kyoto) **16**, 58 (1956); *ibid* **22**, 227 (1959).

8. I. Mannari, Progr. Theoret. Phys. (Kyoto) **22**, 335 (1959).

9. G. K. White and S. B. Woods, Philos. Trans. R. Soc. London A **251**, 273 (1959).

10. J. P. Jan, in *Solid State Physics*, edited by F. Seitz and D. Turnbull (Academic Press, New York, 1957), Vol. 5, p. 27.

11. M. T. Béal-Monod and R. A. Weiner, Phys. Rev. **170**, 552 (1968).

12. A. Banerjee and A. K. Majumdar, Phys. Rev. B **46**, 8958 (1992).

13. D. A. Goodings, Phys. Rev. **132**, 542 (1963).

14. T. K. Nath and A. K. Majumdar, Phys. Rev. B **53**, 12148 (1996).

15. B. L. Altshuler, and A. G. Aranov, Solid State Commun. **30**, 115 (1979).

16. P. A. Lee and T. V. Ramakrishnan, Rev. Mod. Phys. **57**, 287 (1985).

17**.** S. Chakraborty and A. K. Majumdar, Physical Review B **53**, 6235 (1996).

18. S. Banerjee and A. K. Roychowdhury, Solid State Commun. **83**, 1047 (1992).

19. S. I. Masharov, Phys. Stat. Sol. **21**, 747 (1967).

20. Hiroshi Yamada and Satoshi Takada, J. Phys. Soc. Jpn. 34, 51(1973).

21. R. Mallik, E. V. Sampathkumaran, and P. L. Paulose , Appl. Phys. Lett. **71**, 2385 (1997).

CHAPTER V

Probing exotic magnetic phases and critical behavior of Ni-rich γ-NiFeCr alloys

5.1 Preamble

A systematic study has been done to determine the magnetic properties as well as the critical exponents of a set of Cr-rich γ-NiFeCr alloys. The Curie temperature and the spontaneous magnetization decrease rapidly with increasing Cr and decreasing Fe concentration. The static critical exponents and the amplitudes, related to the transition near the Curie temperature, are obtained through detailed DC-magnetization and AC-susceptibility measurements. The values depart significantly from the 3D-Heisenberg model and those of pure Ni due to competing pair interactions in the system.

5.2. Motivation

The 3d transition metal alloys like NiFeCr are of great importance due to a variety of physical properties and consequent applications. These alloys, which are extremely sensitive to the concentration of magnetic components present, show complex magnetic behavior. These are very prospective materials for use in nuclear fusion reactors due to high corrosion resistance and potentially small radiating swelling. These can also be used as buffer layers in high-density magnetic storage devices. The complex magnetic properties can be understood by antiferromagnetic exchange interaction between Cr atoms from which a competition arises

between ferromagnetic and antiferromagnetic exchange interactions. These competing exchange interactions exhibit long-range ferromagnetic/antiferromagnetic order as well as spin-glass-like ordering depending on the concentration of magnetic components present in the system. Magnetic NiFeCr ternary alloys having competing exchange interactions is one of such systems which shows diverse magnetic phases within the same crystallographic phase and is extremely sensitive to the concentration of Cr. This can be explained by strong competing ferromagnetic [I(Ni-Ni), I(Fe-Ni), I(Ni-Cr), I(Fe-Cr)] and antiferromagnetic [I(Fe-Fe), I(Cr-Cr)] exchange interactions. These conflicting pair interactions exhibit different kinds of exotic magnetic phases like spin glass, ferromagnetic, antiferromagnetic, etc. and compositional phase transition from long-range FM ($Ni_{74}Fe_6Cr_{20}$) to long-range antiferromagnetic one, passing through intermediate phases of SG and RSG with decreasing Fe and increasing Cr concentration. This stimulates us to develop new experimental and theoretical analysis to investigate this system more accurately. However, a large number of work on this system have been done both experimentally as well as theoretically but still not much on with high concentration of Cr (18-23%).

5.3 Experiment

The $Ni_{100-x-y}Fe_xCr_y$ alloys (x = 1~6, y = 18~23) were prepared by arc melting the constituents under argon atmosphere. The purities of the starting materials were of 99.999% obtained from M/s Johnson Matthey Inc., England. Each sample was encapsulated in an evacuated quartz ampule, annealed at 1150 ^oC for 100 h. A subsequent fast quench into oil was performed as a step to prevent any possible chemical clustering and to preserve their high-temperature γ-phase (FCC) and also the random substitutional disorder. After cold rolling, the

homogenized alloys in bulk form were cut to various sizes and annealed at 900 ^{o}C for 24 h in argon atmosphere to reduce strains due to cold work and finally they were quenched in brine. The typical compositions of the alloys are 73-80 at. % Ni, 1-6 at. % Fe, and 18-23 at. % Cr. All the samples were characterized through the X-ray diffraction (XRD) method to investigate the possible presence of any second phase (say, bcc) apart from fcc γ-phase. The diffraction patterns reveal that all the alloys have single-phase f.c.c structure, with lattice parameter a = (3.54±0.01) Å. There is a very small change in lattice constant with concentration. Energy dispersive X-ray analysis (EDXA) technique has been used to check the variations in the homogeneity of the alloys and found the compositions within 0.5 % in all the three constituents. This is quite acceptable. Magnetization measurements were performed using a MPMS Quantum Design SQUID magnetometer operating in the RSO mode. The magnetization M was recorded as a function of temperature at fixed applied magnetic fields according to the zero filed cooling (ZFC) and field cooling (FC) prescriptions. Measurements of M versus H at fixed temperatures were also done. In order to minimize the demagnetization effects, the field was always kept parallel to the sample. The temperature dependent real and imaginary parts of the AC susceptibility were measured from 4 K to 300 K in the frequency range 1-1000 Hz with a Quantum Design PPMS. The amplitude of the exciting AC field was kept fixed to 5 Oe. No external DC field was applied in these measurements.

5.4 Results and Discussions

5.4.1 Lattice parameter

The X-ray diffraction of the samples was done using a Philips XRD machine (X'Pert PRO Diffractometer) with a Guinier type camera employing a focusing geometry and a solid-state detector. The radiation used was Cu $K_{\alpha 1}$. The chemical composition of the alloys was determined using standard analytical methods like energy-dispersive X-ray analysis (EDAX). XRD measurements revealed that all the alloys are of single f.c.c phase. The measured lattice constants differ by only ~ 2.5 % from that of pure nickel. A typical lattice constant for $Ni_{79}Fe_1Cr_{20}$ alloy is a = (3.54±0.01) Å. A typical XRD pattern for $Ni_{79}Fe_1Cr_{20}$ is shown in Fig. 5.1. However, the value of 'a' did not differ much for other samples.

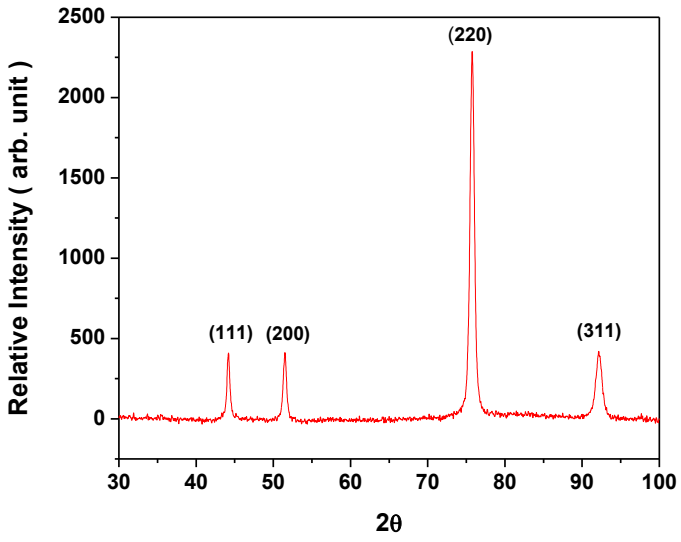

Fig.5.1 XRD pattern of $Ni_{79}Fe_1Cr_{20}$ alloy.

5.4.2. Ternary composition diagram

Figure 5.2 shows the ternary composition diagram of the $Ni_{100-x}Fe_xCr_y$ alloys. The magnetic phases at 10 K, obtained from the magnetic measurements detailed below from sub-sections 5.4.3 and beyond, are also indicated in the diagram. We find that at 10K $Ni_{79}Fe_1Cr_{20}$ and $Ni_{76}Fe_2Cr_{22}$ are AFM's, $Ni_{80}Fe_2Cr_{18}$, $Ni_{77}Fe_5Cr_{18}$, and $Ni_{73}Fe_4Cr_{23}$ are FM's, $Ni_{74}Fe_6Cr_{20}$ is a SG and $Ni_{74}Fe_4Cr_{20}$ is a paramagnet.

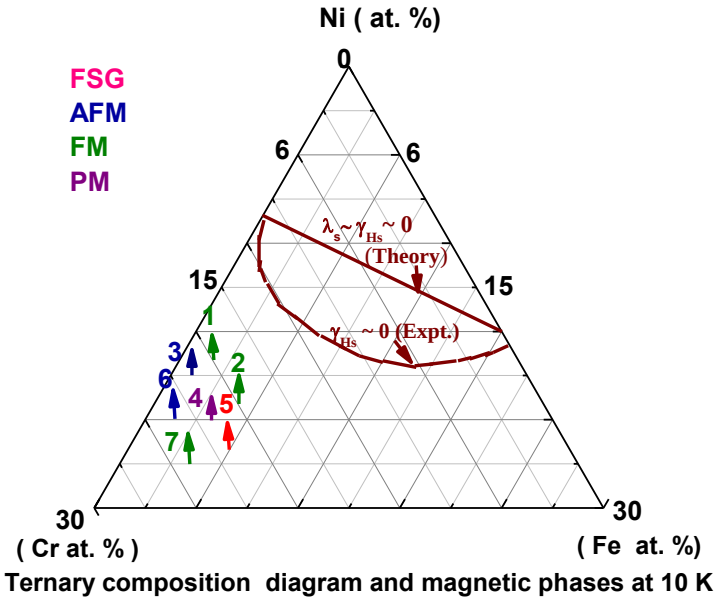

Fig.5.2 Ternary composition diagram of Ni-rich γ-NiFeCr alloys. Their magnetic phases at 10 K are also indicated. 1. $Ni_{80}Fe_2Cr_{18}$, 2. $Ni_{77}Fe_5Cr_{18}$, 3. $Ni_{79}Fe_1Cr_{20}$, 4. $Ni_{76}Fe_4Cr_{20}$, 5. $Ni_{74}Fe_6Cr_{20}$, 6. $Ni_{76}Fe_2Cr_{22}$, 7. $Ni_{73}Fe_4Cr_{23}$. Also shown are the theoretical and experimental $\lambda_{Hs} \sim \gamma_{Hs} \sim 0$ lines.

In Fig. 5.2, the solid line represents the coefficient of linear magnetostriction (λ_S) ~ 0 and Hall conductivity (γ_{Hs}) ~ 0 which are theoretically predicted while the line with considerable curvature is the experimentally established $\gamma_{Hs} \sim 0$ line at 10 K and it lies much below from the

theory one. We observe that γ_{Hs} is negative for all the seven samples taken here and its negativity increases with increasing Cr concentration (18-23%). The sign of γ_{Hs} is determined by the dominating carriers in different sub-bands and their spins and it should be negative for the present ferromagnetic samples[1]. It is to be noted that the total orbital angular momentum and hence λ_S and γ_{Hs} change sign at the composition where Fermi level crosses the point of intersection of the spin-down bands of Ni and Fe.

5.4.3 DC- magnetization

The DC magnetization yields the transition temperatures ($T_C/T_{fg}/T_N$) for all the alloys. Figure 5.3(a) shows a representative M versus T measurement for the alloy $Ni_{73}Fe_4Cr_{23}$ measured at H = 30, 50, 100, and 200 Oe. A clear ZFC-FC splitting occurs at low temperatures as expected for a re-entrant system. This splitting is associated with canting temperature T_{fg}. In Fig. 5.3 (b) an H-T phase diagram, derived from our data, is shown. The temperatures T_{fg} were obtained from the points where the ZFC and FC curves split and the Curie temperatures $T_C(H)$ were estimated from the first derivative of M(T) graphs. This diagram illustrates the peculiarities of the different magnetic phases. When the temperature is decreased, a transition occurs from the paramagnetic state to a ferromagnetic phase where the order parameter is the spontaneous magnetization. Upon further decreasing the temperature, the system enters into a spin-glass-like state below $T_{fg}(H)$ where effects of disorder and frustration play a major role, as revealed by the ZFC-FC irreversibility in the magnetic properties. Due to freezing of transverse degrees of freedom, the spins become canted at this temperature. It can be clearly noticed from the Fig. 5.3(a) that the bifurcation temperature shifts towards lower temperatures with increasing applied magnetic fields and vanishes at a field of 200 Oe. This is one of the characteristics of spin-glass-like systems.

(a)

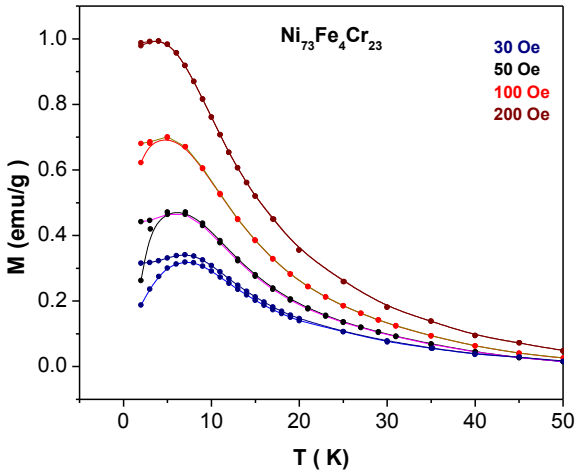

(b)

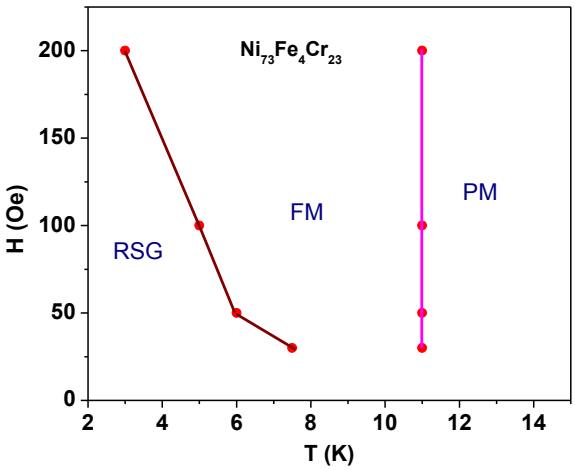

Fig.5.3 (a) Magnetic moment as a function of temperature for $Ni_{73}Fe_4Cr_{23}$ measured at H = 30, 50, 100, and 200 Oe according to the zero-field cooling (ZFC) and field cooling (FC) prescriptions. (b) H-T diagram for $Ni_{73}Fe_4Cr_{23}$ showing the location of paramagnetic (PM), ferromagnetic (FM), and re-entrant spin glass (RSG) regions.

Among all the seven samples, $Ni_{74}Fe_6Cr_{20}$ has the highest T_C of 193 K followed by 69, 20, 12, and 7 K for the others and also the highest T_g (13 K) followed by 8, 4, and 4 K. We have noticed that the transition temperatures (T_C and T_g) strongly depend on the concentration of Fe as well as Cr in the system. Even addition of very small amounts of Fe enhances the transition temperatures (T_C) a lot while it decreases with increasing Cr concentration. This is mainly due to competing exchange interactions between Fe-Fe, Cr-Cr, and Fe-Cr. The first two are antiferromagnetic and the last one is a ferromagnetic interaction. We have found T_C, T_N, and T_{fg} for every alloy and found no systematic variation of $T_C/T_{fg}/T_N$ with Ni, Fe, and Cr concentration. The values of $T_C/T_{fg}/T_N$ of all the seven samples are given in Table 5.1.

Table 5.1: Values of T_C, T_N, and T_{fg}

Sample Designation	T_C (K)	T_{fg} (K)	T_N (K)	Magnetic moment at 2 K and 1 Tesla (emu/g)	Magnetic moment at 2 K and 0.1 Tesla (emu/g)
$Ni_{80}Fe_2Cr_{18}$	20	8	-	7.1	6.2
$Ni_{77}Fe_5Cr_{18}$	69	4	-	9.3	6.6
$Ni_{79}Fe_1Cr_{20}$	-	-	18	< 0.1	0.02
$Ni_{76}Fe_4Cr_{20}$	7	4	-	4.8	2.0
$Ni_{74}Fe_6Cr_{20}$	193	13	-	18	17.8
$Ni_{76}Fe_2Cr_{22}$	-	-	22	1.7	0.5
$Ni_{73}Fe_4Cr_{23}$	12	6	-	4.3	2.0

From Table 5.1 it can be seen that upon varying the concentration of Ni, Fe, and Cr the system passes through different kinds of magnetic phases like ferromagnetic (FM), antiferromagnetic (AFM), and ferro-spin-glass (FSG). As shown in Figs. 5.3(a), 5.4(a), and 5.4 (b) we find that there is an additional transition in M(T) curve below T_C for almost all the samples (except the antiferromagnets $Ni_{76}Fe_2Cr_{22}$ and $Ni_{79}Fe_1Cr_{20}$). This is interpreted in terms of a re-entrant or ferro-spin-glass phase due to competing ferro- and antiferromagnetic pair interactions. The ZFC curves for $Ni_{76}Fe_4Cr_{20}$ show peaks at T_{fg} (4 K) which remains almost constant with increasing applied magnetic field.

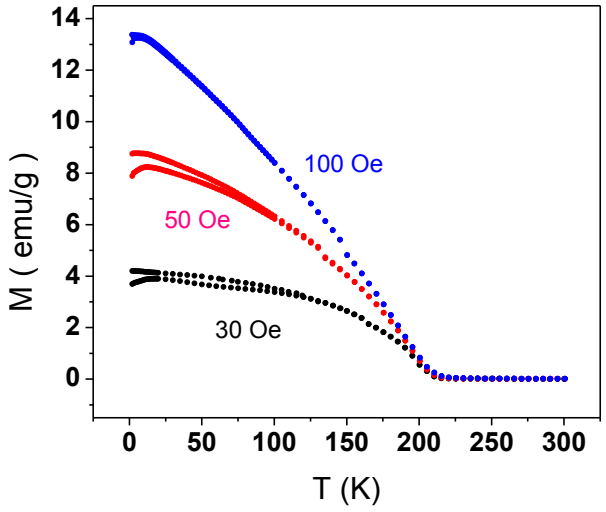

(a)

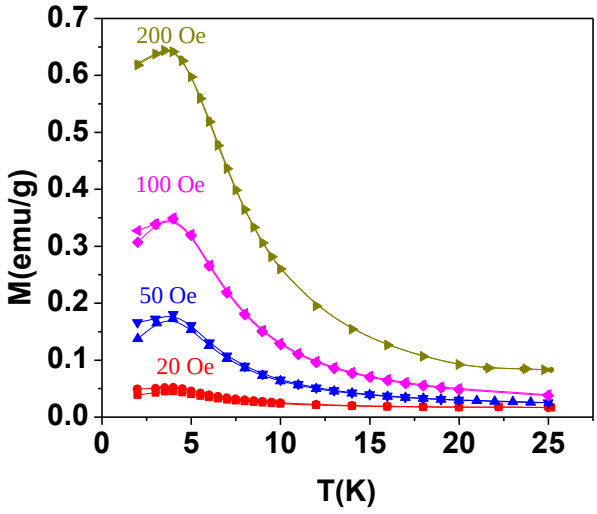

(b)

Fig.5.4 (a) Magnetic moment as a function of temperature for $Ni_{74}Fe_6Cr_{20}$ alloy measured at H = 30, 50, 100 Oe (b) $Ni_{76}Fe_4Cr_{20}$ alloy at H = 20, 50, 100, and 200 Oe according to the zero field cooling (ZFC) and field cooling (FC) prescriptions.

5.4.4 AC-susceptibility

The ac-susceptibility (χ) measurements are performed in the temperature range 2-300 K and in the frequency range 1–10000 Hz, at an AC field of 5 Oe using QDMPMS. Figures 5.5(a) and (b) show respectively the real and imaginary parts of χ versus T at different frequencies (11, 111, 4111, 7111, and 9997 Hz) for $Ni_{77}Fe_5Cr_{18}$ sample.

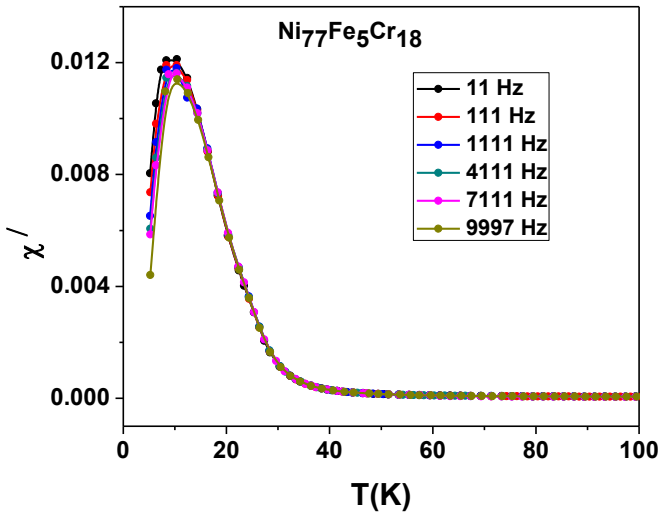

(a)

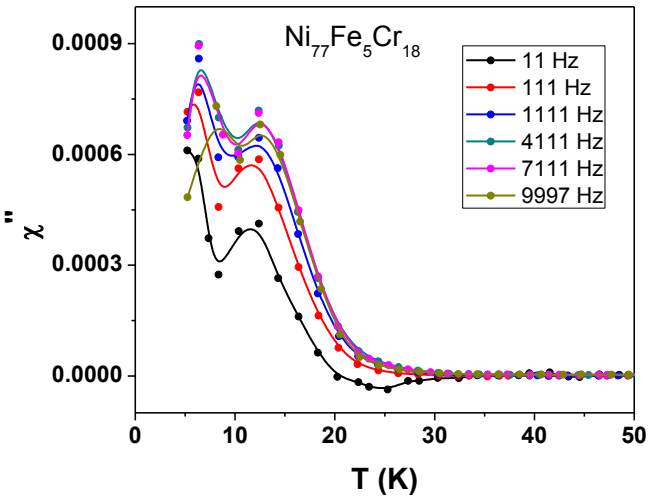

(b)

Fig.5.5 (a) and (b) Real and imaginary parts of χ versus temperature at several frequencies for sample $Ni_{77}Fe_5Cr_{18}$.

The T_C's found from ac measurements are in good agreement with .those found from dc measurements. The ac χ shows strong frequency dependence as shown in the real part of χ vs. T measurements while the imaginary part gives two peaks, one around T_C and another around $T_{fg.}$ However, the imaginary part of the ac susceptibility (Fig. 5.5(b)) gives bifurcated peaks around Tg, one at around 7 K and another at 12 K and a clear dip at the temperature where real part of this susceptibility gives a sharp peak. The imaginary part of χ_{ac} is the Fourier transform of two-spin correlation function characterizing the dynamics of the magnetic systems. So, an anomalous behavior near magnetic phase transition is not unexpected. The real part of χ_{ac} gives only one peak at low temperatures and it shifts towards slightly higher temperatures as the frequency increases. Also, $\chi_{max.}$ decreases with increasing frequency. To interpret the frequency dependence of $\chi_{max.}$ and T_g, we assume the presence of clusters of different volumes which give rise to a distribution of moments in the alloy. The moments of all sizes will be able to follow the magnetic field at lower frequencies while at larger frequencies only the small moments will respond to the external field and the large clusters/moments can not. This gives rise to the larger susceptibility at lower frequencies. The maximum can be explained as a competition between two processes. The moments are frozen at the lowest temperature. But as we raise the temperature, thermal energy gives them some freedom to align and one has higher magnetization with increasing temperature. At a certain temperature all the moments unfreeze and we get a maximum χ. Further increase in the thermal energy disrupts all the alignments and so the moment starts falling as in a paramagnet. Clusters of smaller size are unlocked at lower temperatures compared to those having larger moments. For comparison, the temperature shift in terms of $(\Delta T_g / T_g) \times 100$ % per decade of ω in canonical spin glasses CuMn, AuMn, and $AgMn^2$ is ~ 0.5 %. Figure 5.6 presents the fairly strong frequency dependence of the real part of χ vs.

T which show rounded peaks at T_g, Here this alloy has a much higher value of ~ 5 % per decade. Figure 5.7 shows the variation of T_g with frequency of the applied ac field. The solid lines are just guides to the eye.

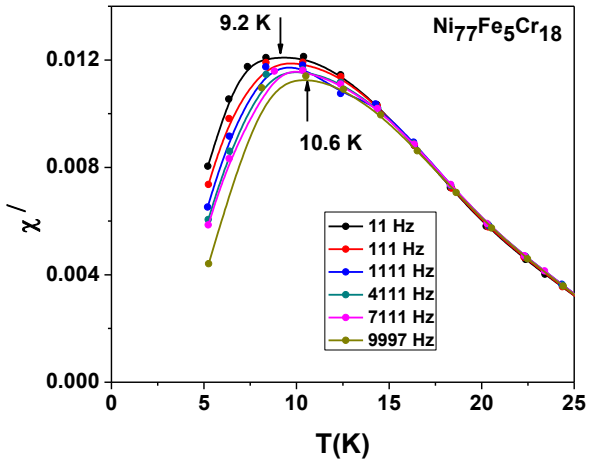

Fig.5.6 Expanded scale plot of real part of ac χ vs. temperature illustrating frequency dependence of T_{fg}.

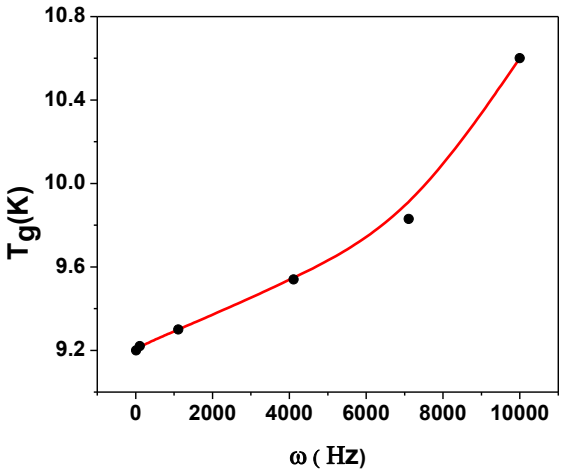

Fig.5.7 Variation of peak temperature (T_{fg}) with frequency of the applied ac field.

5.4.5 High-field magnetization and hysteresis loops

Hysteresis loops were obtained for each sample after cooling in zero fields to 2 K from above $T_C/T_{fg}/T_N$ and measured in fields up to 50 KOe using QDMPMS. In Fig. 5.8 we have plotted magnetization of all the seven samples at 2 K till 10 KOe. The behavior of M (H) changes drastically with concentration of constituent elements. For example, in $Ni_{74}Fe_6Cr_{20}$ and $Ni_{77}Fe_5Cr_{18,}$ $H_{sat.}$ (~ 1 kOe) is more than sufficient for magnetic saturation. For $Ni_{76}Fe_4Cr_{20}$ and $Ni_{80}Fe_2Cr_{18}$, $H_{sat.}$ ~ 5 kOe. For $Ni_{73}Fe_4Cr_{23,}$ the magnetization is still rising till $H_{sat.}$ ~ 10 kOe. All these 5 have $H_{sat.}$ as well as low-field magnetic hysteresis (seen on expanding Fig. 5.8) proving that the long-range ferromagnetic order still persists in the FSG phase at 2 K, i.e., below their T_{fg}'s. For the other two, namely $Ni_{79}Fe_1Cr_{20}$ and $Ni_{76}Fe_2Cr_{22}$, M(H) does not saturate even at the highest attainable field (50 kOe, not shown here) confirming their antiferromagnetic state. However, in Fig. 5.8 we have plotted the magnetization only up to 10 kOe to show the low field features better.

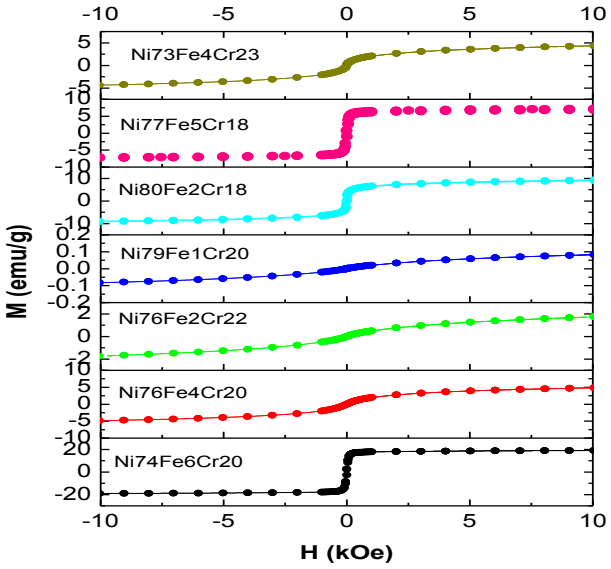

Fig.5.8 M-H curves of all the alloys till 10 kOe at 2 K.

5.4.6 Phase transitions and the associated critical exponents

The second order magnetic phase transition near the Curie point is characterized by a set of critical exponents[3], β, γ, and δ. β is the spontaneous (zero magnetic field) magnetization exponent which is defined by the following relation :

$$M_s (T) = M_0 |\varepsilon|^{\beta}, \quad \text{for } T < T_c \qquad (5.1)$$

where $\varepsilon = (T-T_c)/T_c$ and M_0 is the corresponding critical amplitude.

The critical exponent γ is considered as the isothermal magnetic susceptibility exponent which is related to χ_0, the zero-field dc susceptibility as

$$\chi_0^{-1} = \Gamma^{-1}|\varepsilon|^{\gamma}, \quad \text{for } T > T_c \qquad (5.2)$$

where Γ^{-1} is the corresponding critical amplitude.

From the magnetic field (H) dependence of M at T_C we get another critical exponent given by the relation:

$$M = DH^{1/\delta}, \qquad (5.3)$$

where D is the critical amplitude.

These three exponents follow the static scaling relationship[2], $\beta\delta = \beta + \gamma$.

The exponents often show systematic trends or crossover phenomenon as it approaches T_C. This is due to various competing couplings and disorder in the magnetic system. To find these exponents properly one has to know transition temperatures very accurately. For this purpose M (T) has been measured in all the alloys with temperature increment of 1 K, so that the T_C can be found accurately within ± 0.5 K.

Figure 5.9 (a) shows the temperature dependence of the magnetization M(T) of $Ni_{80}Fe_2Cr_{18}$ sample measured on warming following zero-field cooling (ZFC) under different applied magnetic fields (30, 50, 75, and 100 Oe). The curves show a well defined PM to FM transition at T_C = 70 K. Here, the magnetic transition temperature T_C (~ 70 K) is defined as the inflection point of M vs. T plot or the minimum of dM/dT vs. T curve (Inset of Fig. 5.9(a)). Inverse dc susceptibility $1/\chi$ (T) deduced from ZFC-M(T) at 100 Oe is plotted in Fig. 5.9(b). In the PM region, Curie-Weiss law, i.e. $\chi = C/(T - \theta_w)$ holds, where C is the material-specific Curie constant and θ_w is the Weiss temperature. In Fig. 5.9 (b) we have fitted the data with Curie-Weiss equation. It is seen that $1/\chi_{dc}$ varies linearly with temperature and this implies that Griffiths phase[4] (the phase which lies between spin-glass and paramagnetic phase) is completely absent in this system. θ_w is the Weiss temperature which is somewhat higher than the actual critical temperature.

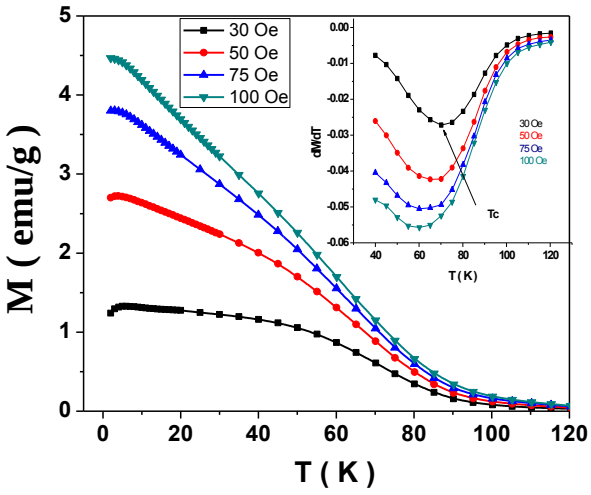

(a)

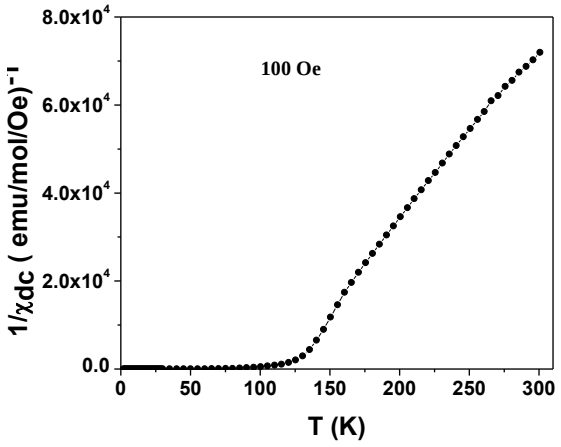

(b)

Fig.5.9 (a) M (T) under different magnetic fields for $Ni_{77}Fe_5Cr_{18}$ alloy. The inset shows dM/dT vs. T. (b) $1/\chi_{dc}$ vs. T at 100 Oe for the same alloy.

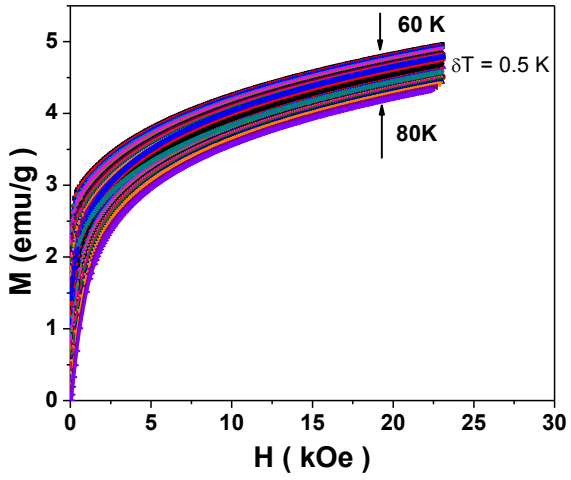

Fig.5.10 Magnetization vs. field at several fixed temperatures closely above and below T_C for the $Ni_{77}Fe_5Cr_{18}$ alloy.

Figure 5.10 shows isothermal magnetization curves around 10 % of T_C in fields ranging from 0 to 23 kOe. The conventional method to determine the critical exponents and critical temperatures involves the use of Arrot plot[5]. According to this method, isotherms plotted in the form of M^2 vs. H/M around T_C which uses critical exponents following mean-field theory. However, in our case they did not give linear isotherms, rather considerable curvature is there and this concave downward curvature clearly indicates a second-order phase transition. The deviation from linearity at low fields can come from large magnetocrystalline anisotropy[6]. In our case, we have deviations even in high magnetic fields indicating deviation of critical exponents from the mean-field value. This type of behavior is found in some magnetic glasses and crystalline ferromagnets[7] and is a subject of great interest.

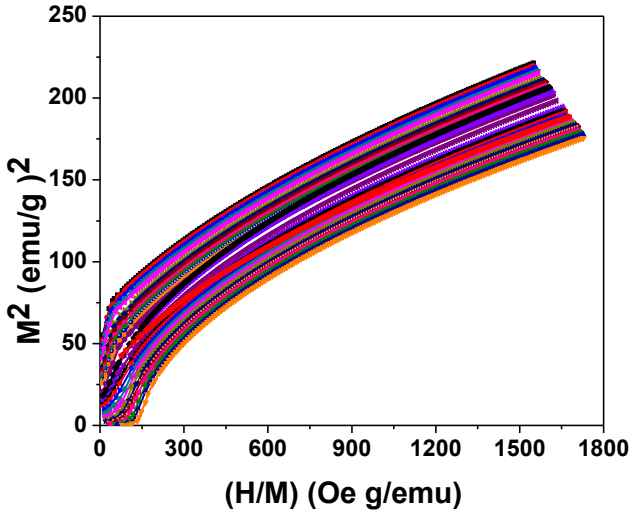

(a)

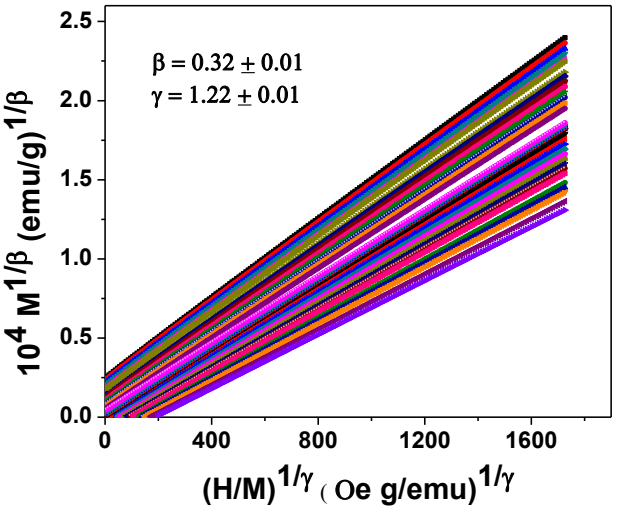

(b)

Fig.5.11 (a) Standard Arrott plot (M^2 vs. H/M isotherms) (b) Modified Arrott-Noakes (AN) plot of $Ni_{77}Fe_5Cr_{18}$ alloy.

In order to obtain a rough estimate of T_C and the critical exponents β and γ, we analyze the isotherms according to the Arrot-Noakes equation of state[8],

$$(H/M)^{1/\gamma} = at + bM^{1/\beta} \quad , \qquad (5.4)$$

where $t = (T-T_C)/T_C$ and a, b are material dependent parameters. Thus, we plot $(H/M)^{1/\gamma}$ vs. $M^{1/\beta}$ at fixed temperatures around T_C in such a way that the exponents β and γ could be varied until straight lines are obtained. However, for a prior knowledge we had to make an intelligent guess initially. We varied β from 0.2 to 0.5 in steps of 0.01 and γ from 0.9 to 1.5 in the same steps. β and γ have been varied until all isothermals are nearly parallel straight lines. The advantages of this plot are: (i) T_C can be determined accurately since the isotherm at T_C will pass through the origin, (ii) x-intercept gives χ_0^{-1}, and (iii) y-intercept gives M_S. The critical isotherm at T = 69 K

is indeed *the* line which passes through the origin giving credence to our plot. It is seen that the values of both γ (1.22) and β (0.32) are very close to those for the 3D-Ising model and β is much lower than the mean-field value of 0.5. The values of spontaneous magnetization and M_S (T) and χ_0^{-1}(T) were obtained from a linear extrapolation of the AN plots to the intercepts with $M^{1/\beta}$ and $(H/M)^{1/\gamma}$ axes, respectively.

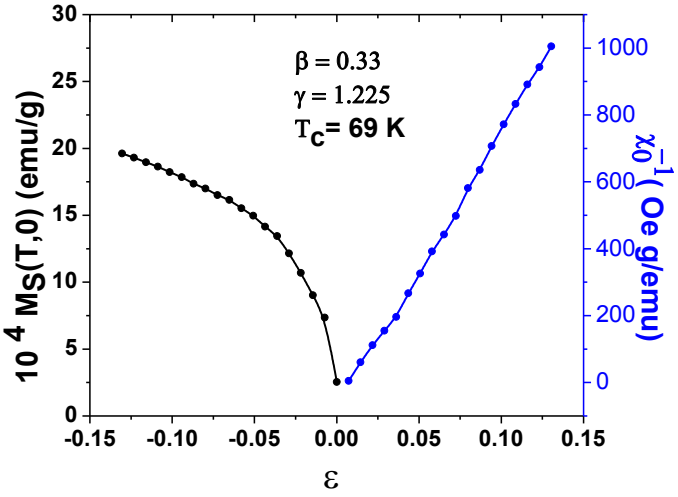

Fig.5.12 M_S and χ_0^{-1}, obtained from modified AN-isotherms, are plotted against ε.

Figure 5.12 plots Ms and χ_0^{-1} as a function of reduced temperature ε. Both these curves intersect at ε = 0, i.e. at T = T_C confirming the critical temperature. By fitting these curves to Eqs. (5.1) and (5.2), we get new values of β and γ using which a new AN plot is constructed. In an iterative process we get stable values of β, γ, and T_C.

Kouvel-Fisher plot: To determine the critical exponents as well as T_C more accurately, we have analyzed the M_S (T) and χ_0^{-1} data using the Kouvel-Fisher plot (KF)[9]. According to this

method, M_S (T,0) $\left(\frac{dM_s(T,0)}{dT}\right)^{-1}$ vs. T and χ_0^{-1}(T) $\left(\frac{d\chi_0^{-1}(T)}{dT}\right)^{-1}$ vs. T yield straight lines with slopes $\left(\frac{1}{\beta}\right)$ and $\left(\frac{1}{\gamma}\right)$, respectively. Here we have used the M_S and χ_0-1 values obtained from the intercepts of the AN plots. In this method a prior knowledge of T_C is not at all needed if the results are consistent.

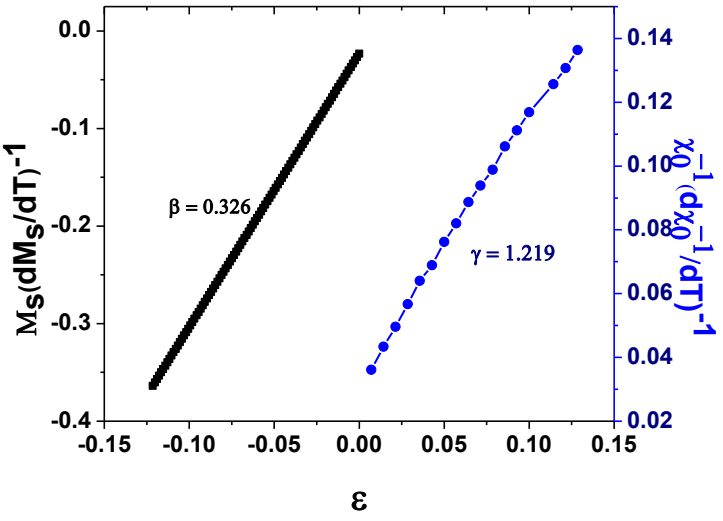

Fig.5.13 Kouvel-Fisher plots for the determination of β and γ.

The KF plots are shown in Fig. 5.13. We notice that the values of the critical exponents obtained from this method match reasonably well with those of the previous method. This implies that the estimated values of the critical exponents are self consistent and unambiguous. Since the critical isotherm obeys the relation $M = DH^{1/\delta}$, a simple plot of ln (M) as a function of ln (H), as shown in Fig. 5.15, allows the determination of δ.

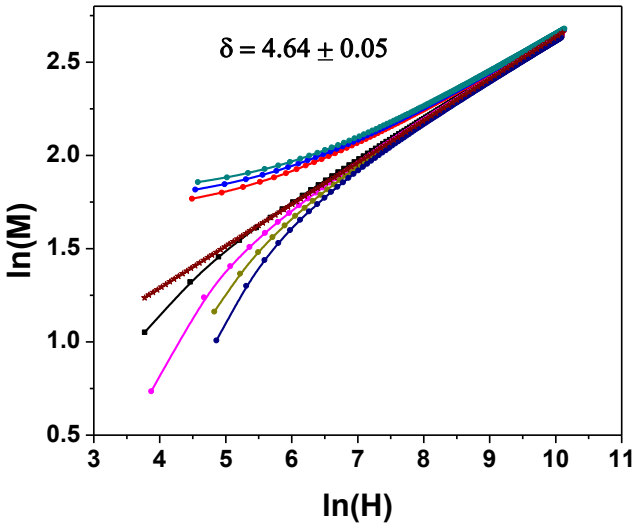

Fig.5.14 Logarithmic plot of the critical isotherms for $Ni_{77}Fe_5Cr_{18}$ alloy.

As shown in Fig. 5.14, we obtain $\delta = 4.64 \pm 0.05$. The value of δ is quite consistent (4.71) with the one calculated from the Widom scaling relationship ($\delta = 1 + \gamma/\beta$) using the previously obtained values for β (0.33) and γ (1.225). In Table 5.2 we show the values of T_C, β, γ, and δ for all the samples. The critical exponent values suggest that our samples more or less follow the 3D-Ising like model and the exponents are very close to those of pure nickel.

Table 5.2 Alloy compositions, values of T_C and critical exponents, obtained both experimentally and from KF analysis along with those for pure Ni and those of earlier reports. Blanks below are for antiferromagnetic samples.

Sample	T_C		β		γ		δ	
	Expt.	KF	Expt.	KF	Expt.	KF	Expt.	(1+γ/β)
$Ni_{80}Fe_2Cr_{18}$	20.0	20.3	0.38	0.39	1.33	1.35	4.41	4.46
$Ni_{77}Fe_5Cr_{18}$	69.0	69.0	0.33	0.32	1.23	1.22	4.64	4.71
$Ni_{79}Fe_1Cr_{20}$	-	-	-	-	-	-	-	-
$Ni_{76}Fe_4Cr_{20}$	7.0	7.1	0.35	0.34	1.25	1.24	4.61	4.65
$Ni_{74}Fe_6Cr_{20}$	193.0	192.0	0.37	0.37	1.31	1.32	4.53	4.54
$Ni_{76}Fe_2Cr_{22}$	-	-	-	-	-	-	-	-
$Ni_{73}Fe_4Cr_{23}$	12.0	12.1	0.47	0.49	1.51	1.52	4.14	4.10
Ni[9]	627.4		0.378		1.34		4.58	4.54
Mean-field			0.50		1.00		3.00	
3D-Ising			0.312		1.25		5.00	
3D-Heisenberg			0.378		1.405		4.76	

From Table 5.2 one finds that the critical exponent β typically has a value in the range of 0.3-0.4, similar to those of 3D-Heisenberg ferromagnets. The value of γ is also close to the theoretical value for the 3D-Heisenberg model. Furthermore, the critical isothermal exponents δ for all the alloys are found to be more or less similar to that of 3D- Heisenberg model (4.76).

Scaling law:

In the critical region, magnetization and internal field should obey the universal scaling behavior. Therefore for a complete knowledge of the critical behavior near ferro-para transition we have calculated critical amplitudes as well. Figures 5.15-18 show respectively plots of $M/|\varepsilon|^{\beta}$ vs. $H/|\varepsilon|^{\beta+\gamma}$, ln χ_0^{-1} vs. ln ε , ln M_s vs. ln H, and ln M_s vs. ln ε.

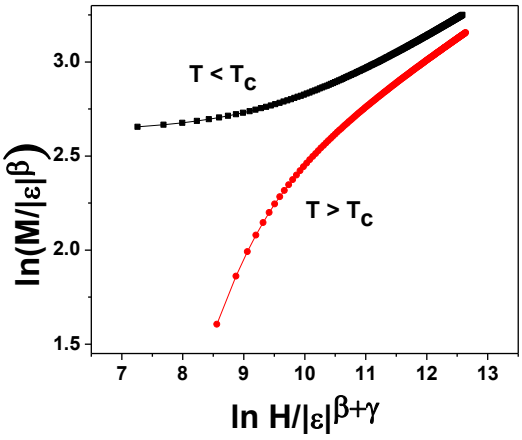

Fig.5.15 $M/|\varepsilon|^{\beta}$ vs. $H/|\varepsilon|^{\beta+\gamma}$ plot.

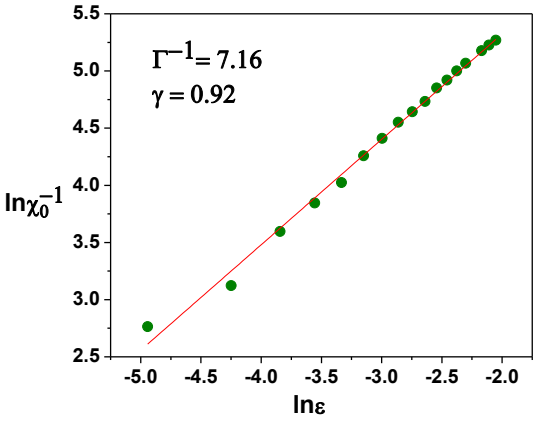

Fig.5.16 ln χ_0^{-1} vs. ln ε plot.

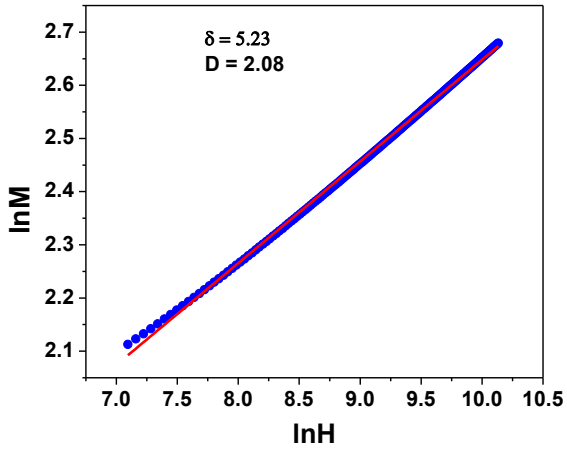

Fig.5.17 ln M_s vs. ln H plot.

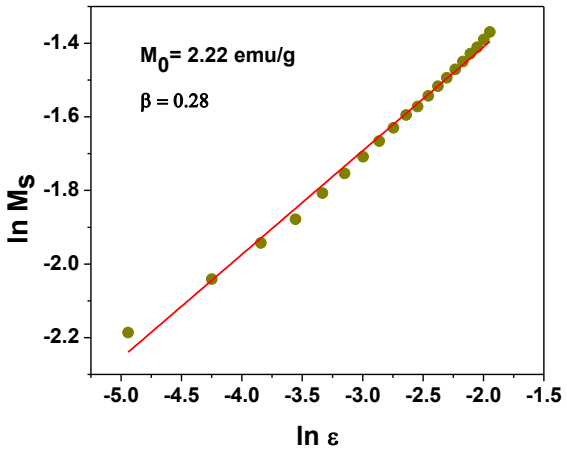

Fig.5.18 lnM_s vs.lnε plot.

The magnetization above and below T_C satisfies a single scaling equation given by $m = f_{\pm}(h)$ where $m = |\varepsilon|^{-\beta} M(\varepsilon,H)$and $h = |\varepsilon|^{-\beta\delta} H$, called scaled magnetization and scaled magnetic field. The above relation shows that m as a function of h falls on two different universal curves f-(h) for $T < T_C$ and $f_+(h)$ for $T > T_C$. If the values of the critical exponents found here are correct, then all

the data will fall on two distinct curves confirming their correct choice. It can be seen from Fig. 5.16 that the scaling is well obeyed, i.e. all the points fall on two curves: one for $T < T_C$ and the other for $T > T_C$. This implies that the values of the critical exponents and T_C are reliable. Also they are in agreement with the scaling hypothesis. The numerical values of the critical amplitudes are also important in the sense that the critical exponents in association with the corresponding critical amplitudes fully characterize the critical behavior near the FM-PM transition at T_C. Surprisingly, in our system, the values of all three critical amplitudes increase with the increase of T_C signifying correlations with magnetic order. However, it is known that the structurally disordered (quenched) alloys have significantly higher critical exponents as well as amplitudes compared to those of the crystalline ones[10].

Table 5.3 The values of the critical amplitudes of the samples and those of pure Ni are given for comparison.

Sample	Γ^{-1} (kOe g/emu)	M_0 (emu/g)	D (emu g^{-1} $Oe^{-1/\delta}$)	T_C (K)
Ni[9]	18.9	83.3	33.1	627
$Ni_{74}Fe_6Cr_{20}$	21.1	15.2	11.4	193
$Ni_{77}Fe_5Cr_{18}$	9.9	8.6	5.1	69
$Ni_{80}Fe_2Cr_{18}$	7.2	5.5	2.1	20
$Ni_{73}Fe_4Cr_{23}$	5.9	3.4	1.7	12
$Ni_{76}Fe_4Cr_{20}$	6.2	3.9	1.8	7

5.5 Conclusions

Varying concentrations of Ni, Fe, and Cr we got different magnetic states, e.g. ferromagnetic, antiferromagnetic, re-entrant spin glass like state in Cr-rich NiFeCr alloys. Several experimental techniques and different methods have been used to analyze their magnetic phases. It has been noticed that with increasing Cr concentration and decreasing Fe concentration, the system goes towards the antiferromagnetic region. Addition of Fe increases ferromagnetism whereas Cr brings in antiferromagnetism.

We have studied the critical behavior near the paramagnetic-ferromagnetic transition in these disordered re-entrant magnetic alloys. The critical exponents β, γ, and δ have been found for all the samples for making a complete study at the PM-FM phase transition temperature. The PM-FM phase transition is identified as second order in nature. The critical exponents estimated from various techniques also match reasonably well.

Bibliography

1. A. K. Gangopadhyay and A. K. Majumdar, Physical Review B, **30**, 1801(1984).
2. J. A. Mydosh, *Spin glasses: an experimental introduction* (Taylor & Francis, London, 1993).
3. H. E. Stanley, Introduction to Phase Transitions and Critical Phenomena, Oxford University Press, London, 1971.
4. A. J. Bray, Phys. Rev. Lett. **59**, 586-589 (1987).
5. A. Arrott, Phys. Rev. **108**, 1394 (1957).
6. J. E Noakes and A. Arrott, J. Appl. Phys. **38**, 973 (1967).
7. A. K. Gangopadhyay, S. B. Roy, and A. K. Majumdar, Phys. Rev. B **33**, 5010 (1984).
8. A. Arrott and J. E. Noakes, Phys. Rev. Lett. **19**, 786 (1967).
9. J. S. Kouvel and M. E. Fisher, Phys. Rev. **136**, A1626 (1964).
10. S. N. Kaul, J. Magn. Magn. Mater. **53**, 5 (1985).

CHAPTER VI

Magneto-transport studies in Ni-rich γ-NiFeCr alloys

6.1 Preamble

After magnetic phase studies we have made a detailed investigation of the magneto-transport properties of the same set of disordered Ni–rich NiFeCr alloy in the temperature range of 2 to 300 K and in magnetic fields up to 50 kOe. The resistivity data of all the alloys exhibit distinct minima lying between 10 and 24 K, unaffected by external magnetic fields. Below the minima, the resistivity is well described by the electron-electron (e-e) interaction effects ($\rho \propto \sqrt{T}$), independent of the magnetic state of the alloys. In the temperature limit, $T_{min}/2 \leq T \leq 2T_{min}$, besides the e-e interaction effects, the magnetic contribution ($\propto T^2$) has been clearly isolated. At higher temperatures, a linear electron-phonon term along with the magnetic term is observed and far above ferromagnetic Curie temperature (T_C) only the linear term persists. The values of the coefficients of the magnetic term ($\propto T^2$) come out to be of the same order as the theoretical one (10^{-5} $\mu\Omega cmK^{-2}$) implying that the magnetic contribution to the electrical resistivity arises from s-s interband scattering. Magnetoresistance (MR) measurements have shown the signature of a spin-glass phase below certain temperatures with ferromagnetic short-range order. Antiferromagnetic phases also have been identified through these transport measurements. Transverse magnetoresistance has been measured in the re-entrant, ferromagnetic, and antiferromagnetic states of the alloys mainly concentrating on the antiferromagnetic-ferromagnetic and ferromagnetic-spin-glass-like transitions. Here in this disordered system the MR over the range 2-300 K rapidly changes sign as the magnetic state changes. Below the spin-glass transition (T_{fg}), the magnetoresistance [$\Delta R(H) = R(H)-R(0)$] shows unexpected hysteresis loops. Thus we could re-establish the magnetic phase diagram (previous obtained from magnetic data) through the present transport measurements.

6.2 Complication of the problem

Though in the last few years, electrical resistivity of disordered magnetic alloys have attracted a lot of attention yet it lacks a complete understanding of the complex nature of the system. As a result, interpretations of transport properties become quite difficult and often controversial, especially when the alloys have high concentrations of 3d metals. In simple metals, the electron-phonon interaction is well described by Bloch-Grùneissen formula, which considers single-band s-s electron-phonon scattering. But in transition metals and their alloys, scattering involving s-d transitions, in addition to the above s-s term, becomes important because of large density of states of the 3-d states. Besides these, scattering of conduction electrons by localised as well as itinerant magnetic electrons (often called spin-disorder resistivity) has an important role in the resistivity of transition metal alloys. The resistivity minima, at low temperatures, in these alloys have been interpreted as the Kondo effect[1]. Later studies on amorphous metallic alloys have shown resistivity minima at low as well as relatively high temperatures. Here the minima have been interpreted as due to electron-electron interaction effects in the presence of weak localisation. Quantum interference effect is important at low temperatures and as a consequence many body effects and electron localization give quantum corrections to the conductivity of highly resistive alloys[2]. On the other hand, at very high temperature, deviation from linearity (DFL) of the resistivity violates the simple Mathiessen's rule as well as Bloch-Grùneissen theory. This happens in the case of mainly highly resistive materials[3] as well as in *d*-band alloys. In case of 3d-transition metal alloys, like NiFeCr, which are highly disordered magnetic materials, the mechanism is much more complicated due to additional scattering of magnetic spins. In this work, temperature dependence of electrical resistivity and magnetoresistance in a broad temperature range is analysed in the framework of Boltzmann and localization models. The low temperature variation of electrical resistivity reveals strong quantum interference effects.

6.3 Theory behind the work

In 3*d* transition metals and alloys scattering of conduction electrons by phonons and their interactions with magnetic spin system are the main sources of the temperature dependence of the electrical resistivity. Generally, in both these cases the scattering may take place within a single band (*s*-*s*) or may involve *s*-*d* transitions. One of the earliest proposals to account for the resistivity variation with temperature of transition metals and their alloys due to electron-phonon s-*d* scattering was made by Wilson[4]. This is given by

$$\rho_{s\text{-}d}(T) = B\left(\frac{T}{\Theta_D}\right)^3 \int_0^{\Theta_D/T} \frac{z^3 dz}{(e^z - 1)(1 - e^{-z})}, \qquad (6.1)$$

In strongly disordered alloys electron localization is important in determining the sign of the temperature coefficient of resistivity. The mutual interference between counter propagating partial waves elastically scattered from nearby ions leads to phase coherence between them. As a consequence, the probability for an electron to return to its origin is enhanced which implies a tendency of localization. Inelastic scattering and magnetic fields, however, can destroy the phase coherence and reduce additional resistivity. Besides the above, scattering of conduction s electrons by phonons and their interactions with magnetic spin systems are the two other sources of the temperature dependence of resistivity. In addition, the effect of cluster-glass type of magnetic order in the present alloy system will have sufficient magnetic contribution to the resistivity. Assuming Matthiessen's rule, the resistivity of the magnetic system can be given by

$$\rho(T) = \rho_0 + \rho_{interaction}(T) + \rho_{phonon}(T) + \rho_{magnetic}(T) \qquad (6.2)$$

$$= \rho_{0+} m_\rho' \sqrt{T} + AT^3 + BT^2,$$

where ρ_0 is the residual resistivity and phonon contribution ~ T^3 is certainly expected in the present alloy system where all the constituents are 3d metals. Electron-electron interaction effects in the weak localization limit is responsible for the resistivity minima where $\rho_{interaction}(T) \infty -\sqrt{T}$. For ferromagnetic metals, spin-wave treatment of s-d electron-magnon interaction leading to s-s transition gives rise to a T^2-dependence of the spin-disorder resistivity[5] given by

$$\rho_{mag}(T) = \frac{\pi^3 \mathscr{V} m \mathscr{G}_{s\text{-}d}^2}{8 \mathscr{N} e^2 \hbar E_F} (g-1)^2 j\left(\frac{kT}{k_F^2 \mathscr{D}}\right)^2 \qquad (6.3)$$

where $\mathscr{G}_{s\text{-}d}$, g, j, E_F, $\mathscr{D}$, $\mathscr{V}$, and $\mathscr{N}$ were all introduced in Chapter IV, below Eq. (4.5).

The resistance of an electrical conductor has been found to either increase (positive magnetoresistance (MR)) or decrease (negative MR) in the presence of magnetic fields. Theoretical models of the positive and negative MR relevant to the present work are briefly described below.

Normal MR: The normal positive MR is inherent in all systems having free electrons. Theories based on the free-electron model lead to a zero MR. A two-band model[6] consisting of two overlapping bands of s and d electrons was therefore proposed. In this model the transverse MR, in small magnetic fields *H*, is given by,

$$(\frac{\Delta\rho}{\rho})_n = 1/2ne(\frac{H}{\rho})^2 \qquad (6.4)$$

where $\left(\frac{\Delta\rho}{\rho}\right)_n$ is called the "normal magnetoresistance," ρ, n, and e have their usual meaning. The above expression is in fairly good agreement with experimental results.

Negative MR: In a metal with magnetic spins, additional quantum mechanical effects like the weak localization or suppression of the spin-flip scattering can give rise to a negative MR. Conduction electrons scatter by exchanging spins with magnetic moments. An external magnetic field increases the energy needed to flip a spin and thus decreases the amplitude of spin-flip scattering which causes resistivity to decrease. Béal-Monod and Weiner[7] calculated the negative MR of dilute alloys containing transition-metal impurities and exhibiting Kondo resistance anomaly. The calculation of the conduction-electron scattering amplitude, in the zero-field limit, yielded the famous Kondo logarithmic temperature dependence. The theory of Bẻal-Monod and Weiner is restricted to alloy systems in which the spins are isolated and hence the spin correlations of the magnetic impurities were ignored.

6.4 Experimental Details

The Ni-rich γ-NiFeCr alloy preparation was described earlier in details in Chapter V, Section 5.3 and lattice parameter determination in Section 5.3.1. The transport measurements were carried out using the standard four-probe AC method in the temperature range 2-300 K using Quantum Design's Physical Property Measurement System (PPMS-6500) with an 8 T superconducting magnet. The electrical contacts were spot welded to the sample, avoiding the formation of any insulating oxide at high temperatures, thereby providing a better electrical contact. The sample current was ~ 100 mA at a frequency of 133 Hz. Data were taken at 1 K interval or less in the whole temperature region and at fixed fields till 5 T. The accuracy in resistance measurements is better than 1 part in 10^5. The stability of the temperature during the measurements was within ±10 mK. The absolute values of the resistivity are accurate only within ± 5% due to uncertainties in the measurements of the dimensions of the samples.

6.5 Results and Discussions

6.5.1 Electrical Resistivity

High-resolution electrical resistivity data of Ni-rich γ-$Ni_{100-x}Fe_xCr_y$ alloys with *x* (1-6) and y (18-23) are presented here in the temperature range $2 < T < 300$ K. All the alloys show resistivity minima at T_{min} lying between 10 and 24 K. In Fig. 6.1, plots of the resistivity normalized to their values at 300 K are shown for all the seven samples. To get a better view of resistivity minima, low-temperature resistivity data normalized to their values at T_{min}, have been plotted till 40 K in Fig. 6.2. T_{min} is found to lie between 10 and 24 K and the depth of minima (DOM) ($[\rho(5K)- \rho(T_{min})]/\rho(5K)$) between 0.005 and 0.18%. The values of resistivity at 5 K (ρ_{5K}), T_{min}, DOM, total change in resistivity, and $\Delta\rho/\rho_{300K}$ ($\Delta\rho = \rho_{300K} - \rho_{min}$ where ρ_{min} is the resistivity at T_{min}) are given in Table 6.1.

Table 6.1: Sample designation, alloy composition, magnetic transition temperatures ($T_c/T_{fg}/T_N$), values of resistivity at 5 K (ρ_{5K}), $T_{min,}$ depth of minima (DOM), and $\Delta\rho/\rho_{300K.}$

Sample designation	Alloy composition	T_c (K)	T_{fg} (K)	T_N (K)	ρ_{5K} (μΩcm)	T_{min} (K)	DOM (%)	$\Delta\rho/\rho_{300K}$ (%)
S1	$Ni_{80}Fe_2Cr_{18}$	20	8	-	158.4	24	0.18	3.2
S2	$Ni_{77}Fe_5Cr_{18}$	69	4	-	178.5	10	0.08	4.7
S3	$Ni_{79}Fe_1Cr_{20}$	-	-	18	174.0	11	0.15	4.5
S4	$Ni_{76}Fe_4Cr_{20}$	7	4	-	186.8	10	0.04	4.8
S5	$Ni_{74}Fe_6Cr_{20}$	193	13	-	174.9	18	0.17	4.1
S6	$Ni_{76}Fe_2Cr_{22}$	-	-	22	169.9	14	0.16	4.4
S7	$Ni_{73}Fe_4Cr_{23}$	12	6	-	182.7	10	0.003	5.3

The high values of the electrical resistivity at 5 K imply strong disorder in these alloys. It is very difficult to get any systematic dependence of T_{min} or DOM on composition since all the constituents vary. This may be due to the fact that the variation in the resistivity in the present system is found to be very small, about 10 μΩcm, compared to that for the concentrated CuMn[8] alloy where it is about 100 μΩcm.

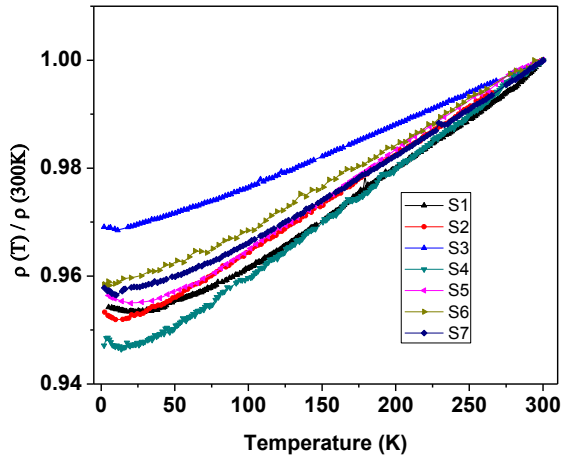

Fig.6.1 Temperature dependence of the resistivity normalized to its value at 300 K.

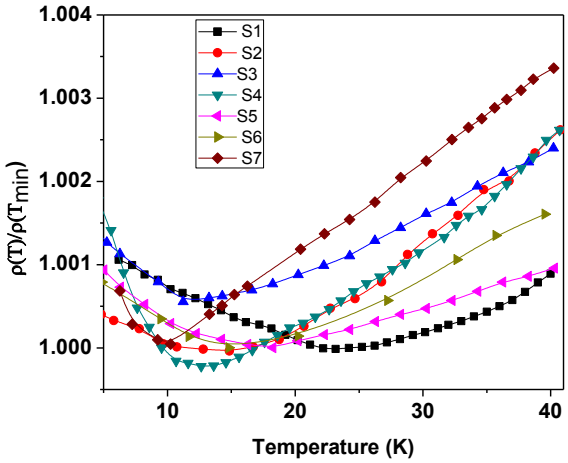

Fig.6.2 Plot of resistivity normalized to its value at T_{min} vs. temperature.

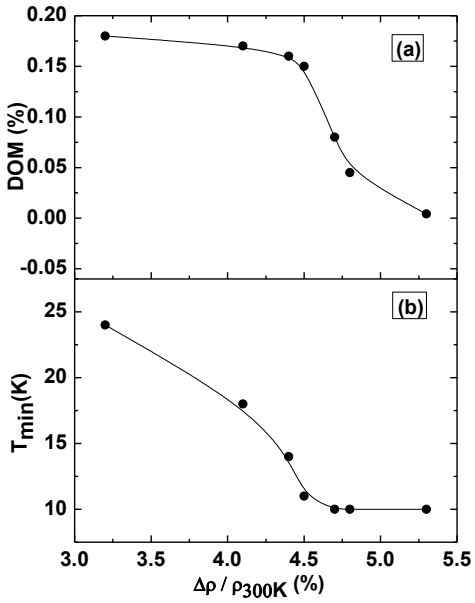

Fig .6.3 Dependence of (a) DOM and (b) T_{min} on $\Delta\rho/\rho_{300K}$ of all the 7 alloys.

In Fig. 6.3, we have plotted DOM and T_{min} with $\Delta\rho/\rho_{300K}$ to find a correlation between the three parameters. We observe that T_{min} almost remains constant for higher values ($\geq$ 4.5%) of $\Delta\rho/\rho_{300K}$. For low values of $\Delta\rho/\rho_{300K,}$ both DOM and T_{min} decrease with $\Delta\rho/\rho_{300K}$. This implies that the resistivity minima become increasingly weaker as the phonon contribution ($\Delta\rho = \rho_{300K} - \rho_{min}$) to the resistivity gets relatively larger.

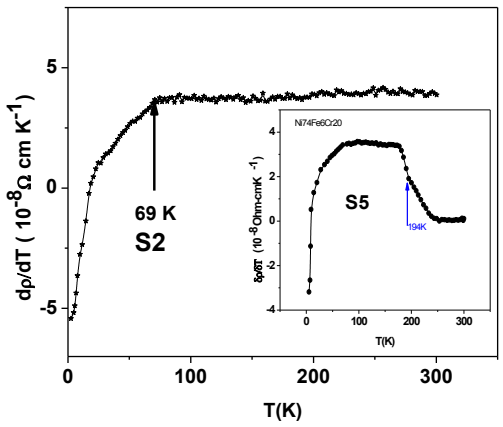

Fig.6.4 Plot of first derivative of ρ vs. temperature for alloys S2 ($Ni_{77}Fe_5Cr_{18}$) and S5 ($Ni_{74}Fe_6Cr_{20}$) in the Inset.

The temperature derivative of resistivity helps to get an overall view of the resistivity. In all the alloys, except S5, dρ/dT versus T shows a continuous, almost linear rise with temperature till a certain temperature, and then it remains constant as shown in Fig. 6.4 while in the case of S5 we found a sharp increase at low temperatures, followed by a constant portion up to 190 K and then a decrease (Inset of Fig. 6.4). The increase in resistivity at low temperatures is due to the magnetic contribution which varies faster than T whereas the phonon term, linear in T, gives rise to the constant dρ/dT at high temperatures. However, S5 exhibits a decrease with temperature after remaining constant up to 190 K which indicates a slower than linear ρ(T) and hence a tendency towards resistivity saturation. In Fig. 6.4, we also find a change in curvature of dρ/dT around their magnetic transition temperatures (T_C) of 69 and 194 K, respectively.

a) Analysis of ρ(T) data in the temperature range $2T_{min} \leq T \leq 300$ K

In this temperature range, the resistivity data show two distinct regions of dependence. In the comparatively high temperature range (200-300 K), the linear temperature dependence is ascribed to the high-temperature electron-phonon interaction (~ T) and in the low-temperature range the electron-magnon scattering (~T^2) has to be introduced. The fit functions, values of the fitting parameters, ranges of temperature, and the values of χ^2, which give the goodness of fit, for all the seven alloys are listed in Table 6.2 from which the following observations can be made.

(i) For the alloys S3 and S6 having single PM-AFM transitions at 18 and 22 K, respectively, the data fit very well with the function $a + bT^2$ in the low temperature range, beyond which the fit becomes poor and only the electron-phonon interaction term dominates. $\chi^2 \approx 10^{-8}$ is consistent with the experimental resolution. Fig. 6.5 is a plot of ρ versus T^2 for the alloy S3 and the best fitted graph. The figure shows a clear linear dependence in this temperature range. The inset of

Fig. 6.5 shows the percentage deviation of the experimental data from the best fitted curve as a function of T^2. (ii) For the rest of the alloys which are in the mixed phase with T_C and T_{fg}, an additional term cT (due to electron-phonon scattering) is added in the low temperature region and the data fit the resulting function $a + bT^2+cT$ very well.

Table 6.2: Fitting parameters for the ρ(T) data to different fit functions, temperature ranges, and the values of χ^2 for $Ni_{100-x}Fe_xCr_y$ alloys.

Sample	Fit function	Fit range (K)	a (μΩcm)	b (10^{-6}μΩcmK^{-2})	c (10^{-6}μΩcmK^{-1})	χ^2 (10^{-8})
S1	$a+bT^2+cT$	50-80	158.5	4.6	3.4	1.7
	a+cT	80-300	159.1	-	3.9	4.5
S2	$a+bT^2+cT$	20-100	178.6	5.7	5.2	1.4
	a+cT	100-300	180.6	-	4.9	6.3
S3	$a+bT^2$	22-50	174.1	1.4	-	2.1
	a+cT	200-300	174.6	-	8.1	1.8
S4	$a+bT^2+cT$	20-40	186.8	2.2	2.1	4.7
	a+cT	40-300	187.0	-	2.0	3.1
S5	$a+bT^2+cT$	36-250	174.7	9.9	1.6	2.2
	a+cT	250-300	181.4	-	2.0	1.3
S6	$a+bT^2$	28-50	169.9	1.6	-	4.3
	a+cT	200-300	170.0	-	8.0	7.3
S7	$a+bT^2+cT$	20-50	182.8	3.1	4.3	1.8
	a+cT	50-300	183.3	-	6.2	1.9

Table 6.2 shows that the coefficient b has very large values for samples S2 and S5 which have comparatively high T_C. For two antiferromagnetic samples S3 and S6, though the coefficients of T^2 term are very small, still both the curves fit very well to $a + bT^2$ up to 50 K and to $a + cT$ beyond. This proves that though the samples are antiferromagnets with T_N of 18 and 22 K respectively, yet till 50 K they have magnetic contributions to the resistivity $\sim T^2$ as predicted by Masharov for antiferromagnets[9]. Those samples having lower values of T_C (S1, S4, and S7) also fits well with magnetic term but in a very narrow temperature region (given in Table 6.2) and beyond this they have only the electron-phonon interaction term as they are paramagnetic in this region. All these findings are quite compatible with our magnetic data.

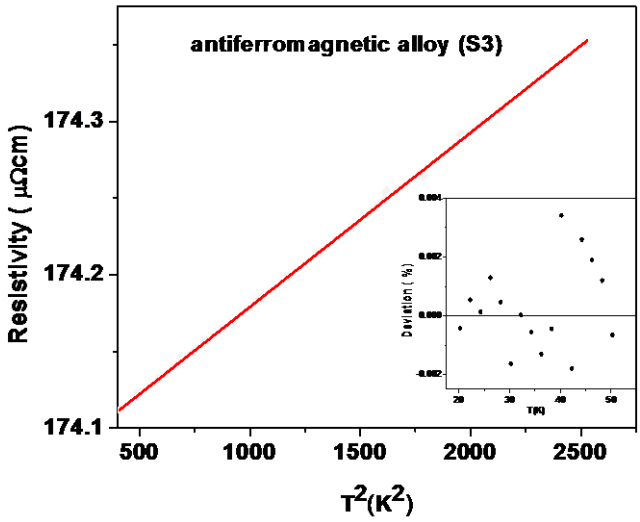

Fig.6.5 Resistivity vs. T^2 plot of the antiferromagnetic sample S3 in the temperature range 20-50 K. The solid line is the best fitted curve. The inset plots the percentage deviation of the fit from the experimental data.

b) Analysis of $\rho(T)$ data in the temperature range $T_{min}/2 \leq T \leq 2T_{min}$

In this temperature range, special attention has been paid to get a better picture of the different competing physical phenomena responsible for resistivity minima. In this range, all the alloys are ferromagnetic or antiferromagnetic or spin-glass-like. Hence magnetic contribution which we already observed at higher temperatures should be present here as well. Besides these, the usual electron-phonon scattering will have their usual contribution to the resistivity. According to Wilson[10], considering s-d scattering in addition to the s-s electron-phonon scattering, $\rho(T) \sim T^3$. This is certainly expected in the present alloys where all the constituents are 3d metals. Detailed analysis on the resistivity below T_{min} has proved that the e-e interaction effects in the weak localization limit is responsible for the minima as ($\rho_{int} \propto -\sqrt{T}$).Thus the resistivity in this region can be written as

$$\rho(T) = \rho_{0+} m_\rho' \sqrt{T} + BT^2 + AT^3. \qquad (6.5)$$

In an earlier work[8], the phonon contribution was found to be negligible compared to those from magnetic and interaction effects and so Eq. (6.5) reduces to

$$\rho(T) = \rho_{0+} m_\rho' \sqrt{T} + BT^2. \qquad (6.6)$$

We have fitted the data to both Eqs. (6.5) and (6.6) for all the alloys. Fitting to Eq. (6.5) gives an unphysical sign of A, but a fit to Eq. (6.6) is satisfactory for all the alloys. The coefficients of the magnetic contribution (B) are found to be an order of magnitude higher than those (b) obtained at higher temperatures ($2T_{min} \leq T \leq 300$ K). Earlier resistivity measurements by White and Woods[11] gave the coefficient of magnetic contribution (T^2) of the order of $10^{-5}\mu\Omega cmK^{-2}$ at very low temperatures (≤ 10 K). Here, we find an order of magnitude higher value of B which is likely due to the s-d transition gradually becoming dominant at higher temperatures (typically 30 K here).

Fig. 6.6 shows resistivity vs. temperature data in the range 12-40 K fitted to $\rho(T) = \rho_0 + m_\rho'\sqrt{T}+BT^2$ along with the best fitted curve for sample S1.

The high resolution data makes the depth of the minimum (only ~ 0.2 %) so prominent. All the fitting parameters and the temperature ranges of all the samples are given in Table 6.3. They show excellent fits with normalized χ^2 of the order of 10^{-8} which is again consistent with our experimental resolution. It is found that the coefficient of the interaction term ($\sim\sqrt{T}$) is of the order of 10^{-2} $\mu\Omega cmK^{-1/2}$ except for the alloys S3 and S6 where it is an order of magnitude higher. Interestingly, the magnetic coefficient terms of those alloys are of an order of magnitude lower implying that the electron-electron interaction effects in these alloys dominate over the magnetic contributions compared to those of the other samples. Finally, the present range of temperature hardly includes the spin-glass-like transition temperature (T_{fg}) to have a dominant spin-glass contribution except marginally for S5.

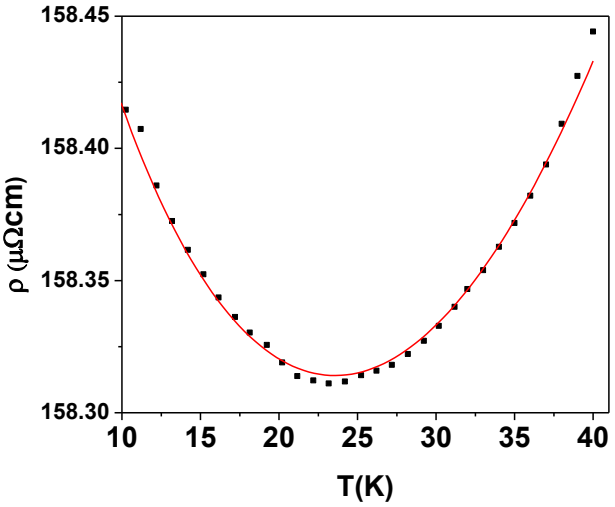

Fig.6.6 Resistivity vs. temperature data in the range 12-40 K fitted to Eq. (6.6) along with the best-fitted curve for sample S1.

Table 6.3: Sample designation, range of fit, values of the fitted parameters, and the normalized χ^2 for fits to Eq. (6.6).

Sample Designation	Range of fit (K)	ρ_0 ($\mu\Omega$cm)	m_ρ^* ($\mu\Omega$cmK$^{-1/2}$) (10^{-2})	B($\mu\Omega$cmK^{-2}) (10^{-5})	χ^2 (10^{-8})
S1	12-40	158.3	-8.1	11.3	4.5
S2	5-20	178.5	-3.0	23.7	1.9
S3	6-22	174.0	-13.9	2.9	7.7
S4	5-20	186.8	-2.2	27.9	3.4
S5	9-36	174.7	-6.1	34.2	2.7
S6	7-28	169.8	-15.5	2.5	8.5
S7	5-20	182.7	-7.0	14.8	5.9

c) Analysis of $\rho(T)$ data in the temperature range $\rho(T) \leq T_{min}/2$

Resistivity well below the minima for highly disordered systems follows $\sqrt{T}$ dependence and has been interpreted in terms of the electron-electron (*e-e*) interaction effects in the presence of weak localization. This theory considers the phase coherence of two electrons both getting localized through elastic impurity scattering. The electrical conductivity[12], σ, due to this e-e interaction effect goes as

$$\sigma(T) = \sigma_0 + m_\sigma \sqrt{T}, \qquad (6.7)$$

where

$$m_\sigma = 1.3e^2/4\sqrt{2}\pi^2\hbar\,[4/3 - 3/2\,F_\sigma][k_B/\hbar D]^{1/2}. \qquad (6.8)$$

Here F_σ is the screening constant for Coulomb interactions and D is the diffusion constant. Earlier measurements[13] on concentrated crystalline alloys had shown the value of m_σ as 6 $(\Omega cmK^{1/2})^{-1}$. But the present alloys are very much disordered and so the increase in resistivity below T_{min} may very well be attributed to the e-e interaction effects. The contributions from magnetic and phonon scattering are found to be negligible in this range. For convenience, in the present analysis, Eq. (6.7) has been modified from conductivity to resistivity as

$$\rho(T) = \rho_0 + m_\rho \sqrt{T}, \qquad (6.9)$$

where

$$m_\rho = - m_\sigma \rho_0^2, \qquad (6.10)$$

assuming $m_\sigma \rho_0 \sqrt{T} << 1$ and so all the higher order terms of $\sqrt{T}$ are negligible .

In dilute crystalline alloys, according to Kondo effect[14], the decrease in resistivity below minima follows

$$\rho(T) = \rho_0 - m \ln T, \qquad (6.11).$$

In this range, our data have been fitted to both the Eqs. (6.9) and (6.11) and it is found that values of the normalized χ^2 for the $\sqrt{T}$ fit is an order of magnitude smaller than that of the lnT fit. Moreover, the plots (not shown) of the deviation between the raw and fitted data ($\rho_{raw} - \rho_{fitted}$) vs. temperature for the lnT fit show systematic trends whereas those for the $\sqrt{T}$ it is found to be random for all these alloys. This random nature of deviations is considered as a good criterion for the goodness of the fit. Hence, a $\sqrt{T}$ dependence of the resistivity in the temperature range below minima, interpreted as coming from e-e interaction effects, is well justified here in these concentrated γ-NiFeCr ternary alloys. The details of the fitting parameters with the values of χ^2 are given in Table 6.4. The coefficient of the $\sqrt{T}$ term, i.e., m_ρ, in these alloys lies in the range (0.16-0.22) $\mu\Omega cm/K^{1/2}$. The calculated values of m_σ [using Eq. (6.10)] are in very good agreement with the near-universal value of 6 $(\mu\Omega cmK^{1/2})^{-1}$.

Table 6.4: Sample designation, values of the fitted parameters along with values of χ^2 for fits to Eq. $\rho(T) = \rho_0 + m_\rho\sqrt{T}$ and the corresponding calculated values of m_ρ and m_σ.

Sample designation	ρ_0 ($\mu\Omega$cm)	m_ρ ($\mu\Omega cmK^{-1/2}$) 10^{-2}	χ^2 (10^{-8})	m_σ ($\Omega cmK^{1/2})^{-1}$
S1	158.4	- 0.16	1.1	6.2
S2	178.6	- 0.18	3.1	5.5
S3	174.1	- 0.22	2.2	7.1
S4	188.8	- 0.18	1.7	5.2
S5	175.0	- 0.20	4.3	6.4
S6	170.1	- 0.21	1.2	7.2
S7	183.0	- 0.20	3.1	6.1

6.5.2 Magnetoresistance

Here we report measurements of transverse magnetoresistance (MR) covering paramagnetic (PM), ferromagnetic (FM), antiferromagnetic (AFM), and ferro-spin-glass (FSG) mixed phases as found from the magnetic data. In the previous chapter we have seen that only $Ni_{79}Fe_1Cr_{20}$ (S3) and $Ni_{76}Fe_2Cr_{22}$ (S6) are antiferromagnets at 2 K while the rest of the samples are ferromagnets with a low temperature coexisting re-entrant ferro-spin-glass (FSG) phase. All these phases are better understood from our MR measurements. In this temperature range, the MR exhibits three distinct features: (i) low-field hysteresis effects in the so-called FSG state

which disappears in high fields (> 2 kOe), (ii) negative MR as we generally find for ferromagnets, and (iii) MR changes sign form negative to positive at higher fields for the antiferromagnetic samples. The magnetic field enhances (or suppresses) the spin fluctuations in the magnetic sub-lattice parallel (or antiparallel) to the field. The positive[15] MR results from a competition between suppression and enhancement of the spin fluctuations.

(i) Low-filed hysteresis effect:

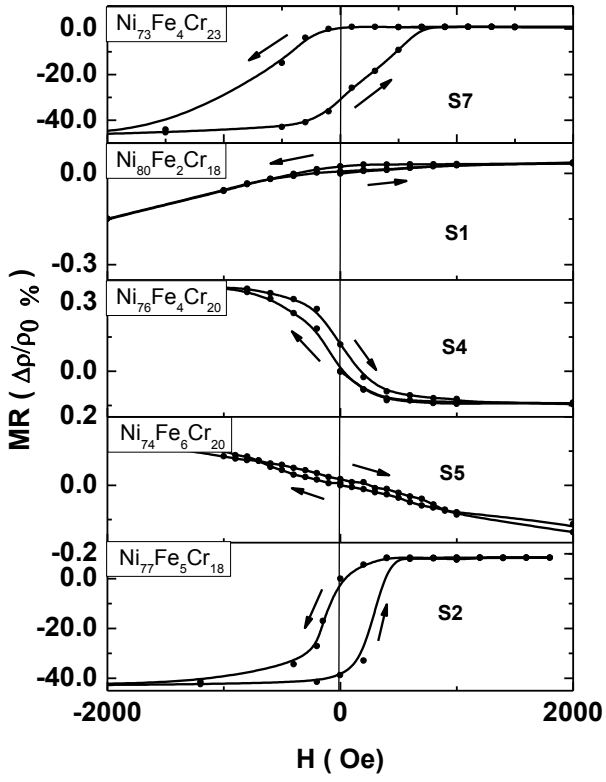

Fig.6.7 Low-field MR curves at 2 K for the samples having re-entrant FSG phase.

Figure 5.2 of Chapter V shows the ternary composition diagram of Ni-rich γ-NiFeCr alloys. Their magnetic phases at 2 K are also indicated. Figure 6.7 here shows the hysteresis effect in MR at 2 K of $Ni_{73}Fe_4Cr_{23}$ (S7, T_{fg} ~ 6 K), $Ni_{80}Fe_2Cr_{18}$ (S1, T_{fg} ~ 8 K), $Ni_{76}Fe_4Cr_{20}$ (S4, T_{fg} ~ 4 K), $Ni_{74}Fe_6Cr_{20}$ (S5, T_{fg} ~ 13 K), and $Ni_{77}Fe_5Cr_{18}$ (S2, T_{fg} ~ 4 K). The outstanding feature of these MR curves is the low-field hysteresis effects and the reversible behaviour at higher fields. It should be noted that the MR is positive here in the low-field region for 3 alloys and negative for $Ni_{76}Fe_4Cr_{20}$ (S4) and $Ni_{74}Fe_6Cr_{20}$ (S5). In view of this unexpected result we have examined this behaviour in Fig. 6.8 for sample $Ni_{73}Fe_4Cr_{23}$ (S7) at several temperatures which covers the whole FSG region and find that the loop area decreases as we approach T_{fg} (~ 6 K).

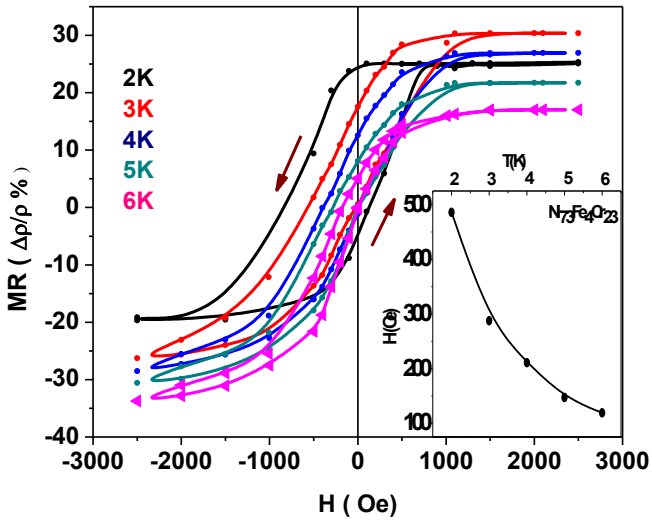

Fig.6.8 Low-field MR hysteresis curves at 2, 3, 4, 5, and 6 K of sample $Ni_{73}Fe_4Cr_{23}$ (S7, T_{fg} ~ 6 K). The inset shows the loop width in Oe as a function of temperature.

It is to be noted that at higher temperatures ($T > T_{fg}$) MR is almost reversible (no hysteresis) while at lower temperatures it is irreversible which is a signature for the existence of a SG

component in the FSG[16] phase, FSG-FM transition at T_{fg} separating the two regimes. The hysteretic effect (loop width in the inset of Fig. 6.8) undergoes a rapid fall as we enter the FM region from the FSG state. The size of magnetic domain changes as the samples enter the FSG[17] state from the FM one. The alloys undergo PM→FM→FSG transitions as we lower the temperature from room temperature. Thus the MR measurements presented here strongly support the magnetic phase diagram.

(ii) Negative MR:

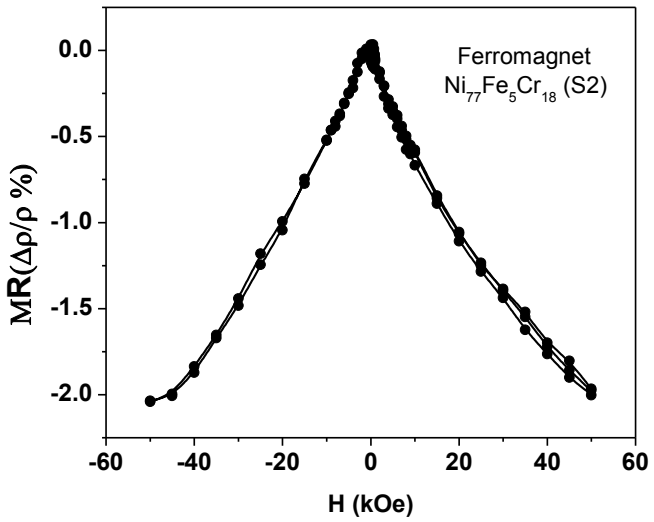

Fig.6.9 MR curve for $Ni_{77}Fe_5Cr_{18}$ (S2) at 50 K till 50 kOe.

Figure 6.9 is a plot of MR vs. H till 50 kOe for $Ni_{77}Fe_5Cr_{18}$ (S2) at 50 K. According to our magnetization data at 50 K the sample is in a FM state (T_C = 69 K). This negative transverse MR is a signature of ferromagnetism and is present in all the 5 FSG alloys below their respective T_C's. It shows a sharp low-field negative transverse MR of ~ 0.5 % at 5 kOe. The physics behind

this negative MR is that there is less electron-magnon scattering at higher fields since some magnons are quenched by the Zeeman term in the magnon dispersion relation. In alloys containing small magnetic clusters, a relatively large field is necessary to overcome the anisotropy energy. So it is difficult to accomplish ferromagnetic alignment of all the moments. Hence the large magnetoresistance cannot be easily saturated.

(iii) MR changes from negative to positive:

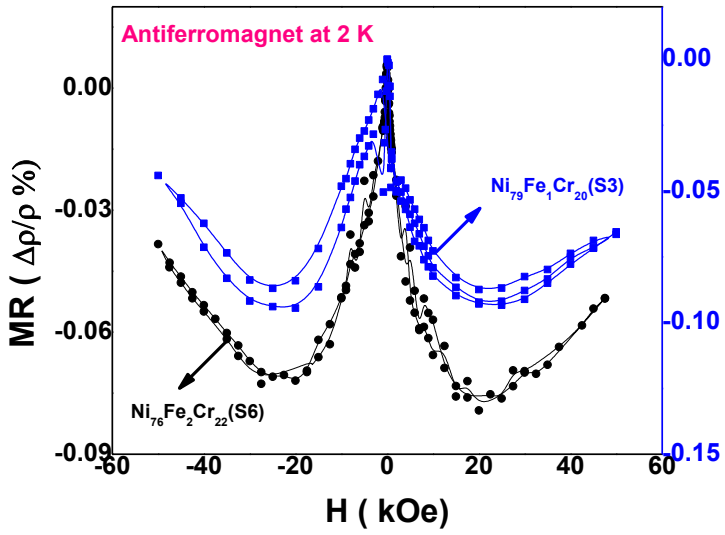

Fig.6.10 The MR curves of samples $Ni_{79}Fe_1Cr_{20}$ (S3) and $Ni_{76}Fe_2Cr_{22}$ (S6) at 2 K till 50 kOe.

Obviously, the negative MR is that of a typical ferromagnet like $Ni_{77}Fe_5Cr_{18}$ (S2) of Fig. 6.9. At lower applied fields the MR is negative since the effective field acting on the localized spins suppresses the spin fluctuations. A *positive* magnetoresistance (MR) is observed at higher applied magnetic fields (> 20 kOe). This can be interpreted as follows: The fluctuation of the spins of one sublattice may be suppressed but that of the other may be enhanced with increasing

magnetic fields. From Fig. 6.10 we see that the MR changes sign from negative to positive for both the samples $Ni_{79}Fe_1Cr_{20}$ and $Ni_{76}Fe_2Cr_{22}$ (S3 and S6 which are AFM) at 2 K.

6.6 Conclusions

In conclusion, important correlations between $\Delta\rho/\rho_{300K}$ with DOM and T_{min} are obtained from the resistivity data in γ-$Ni_{100-x}Fe_xCr_y$ ternary alloys. In addition, both the resistivity and magnetoresistance measurements reveal the different magnetic phases of the seven alloys. For example, in the FM and AFM alloys, the resistivity varies like ~ T^2 above minima and the value of the coefficient of the T^2 term decreases as we approach higher temperatures and finally the resistivity varies as T. However, in the low temperature limit, e.g, below T_{min}, though most of the samples are in spin-glass-like state, yet we hardly get any evidence of its contribution; rather we find the dominance e-e interaction effects.

Through the MR measurements, we have further strengthened the magnetic phase diagram of the re-entrant NiFeCr alloys. The above studies have thrown new light and insight into the magnetic structure by virtue of the sensitivity of the MR, not only to the magnetization, but also to the type of coupling which exists between the moments in the PM, FM, AFM, or FSG-like states. We have also been able to detect low-field hysteresis effects in the MR which we associate with a long-range ferromagnetism of the longitudinal (Z) moments coexisting with re-entrant (X-Y) spin-glass phase**.** We also propose that some moments are sufficiently free to move with the application of magnetic fields leading to an increase of MR in the AFM state.

Bibliography

1. J. Kondo, Prog. Theor. Phys. 32 (1964) 37; J.S. Dugdale, The Structures and Properties of Solids 5 - The Electrical Properties of Metals and Alloys, Edward Arnold Publications, UK, 1977.
2. B. L. Altshuler and A. G. Aronov, in *Electron-Electron Interactions in Disordered Systems*, edited by A. L. Efros and M. Pollak (North-Holland, Amsterdam, 1985).
3. Z. Fisk and G. W. Webb, Phys. Rev. Lett. **36**, 1084 (1976).
4. A. H. Wilson, Proc. R. Soc. London A **167**, 580 (1938).
5. T. Kasuya, Prog. Theor. Phys. (Kyota) **16**, 58, (1956).
6. J. P. Jan, in *Solid State Physics,* edited by F. Seitz and D. Turnbull (Academic, New York, 1957), Vol. 5, p.27.
7. M. T. Béal-Monod and R. A. Weiner, Phys. Rev. **170**, 552(1968).
8. S. Chakraborty and A.K. Majumdar, Phys. Rev. B **53,** 6235(1996).
9. S.I. Masharov, Physica Status Solidi **21**, 747 (1967).
10. A. H. Wilson, Proc. Roy. Soc. (London) A **167**, 580 (1938).
11. G. K. White and S. B. Woods, Phil Trans. Roy. Soc. London A **251**, 273 (1958).
12. P. A. Lee and T. V. Ramakrishnan, Rev. Mod. Phys. **57**, 287(1985).
13. R. W. Cochrane and J. O. Storm-Olsen, Phys. Rev. B **29**, 1088 (1984).
14. J. Kondo, Prog. Theor. Phys. **32**, 37 (1964).
15. A. K. Nigam, S. B. Roy, and Girish Chardra, Phys. Rev. B **49**, 1127 (1994).

16.Tetsuya Mizuguchi and Teiichi Miyauchi, IEEE TRANSACTIONS ON MAGNETICS, **35**, No.5 (1999); R. D. Barnard, Ch. Böttger, S. Thamm, and J. Hesse, J. Phys: Condens. Matter **4,** 7219 (1992).

17. T. Miyazaki, I. Okamoto, Y. Ando, and M. Takahashi, J. Phys F*:* Met. Phy. **18**, 1601 (1988)**.**

CHAPTER VII

Summary and future directions

In this chapter, we shall summarize this thesis by highlighting our important findings followed by some future plans.

7.1 Summary

This work is based on studying magnetic and transport properties of nickel based disordered binary and ternary alloys (Ni-Mn and NiFeCr) which is important both for understanding of magnetic phases of alloys and also from the point of view of applications. These Ni-Mn and NiFeCr alloys are used extensively in applications where heat resistance and/or corrosion resistance is required at low cost as well as in magnetic storage devices. The important findings of the present study are briefly summarized below:

i) Determination of concentration dependence of magnetic moments and transition temperatures for fcc Ni-Mn alloys experimentally and comparison with theory. Our experimental measurements and theoretical calculations for $Ni_{100-x}Mn_x$ ($15 \leq x \leq 37$) alloys establish the interesting magnetic phase diagram with different magnetic states including spin glass and re-entrant spin-glass-like phases. Magnetic phase studies have been done in disordered $Ni_{100-x}Mn_x$ system over a wide concentration range ($15 \leq x \leq 37$) encompassing the critical concentration ($x \sim 25$). This magnetic phase diagram, derived from dc magnetization and ac susceptibility data, serves as an essential reference for the changes with composition of various measured properties and of the corresponding parameters of a variety of phases including ferro-spin-glass. The detailed magnetic study of this system confirms the multicritical point (MCP). This study also reveals the existence of re-entrant magnetic phase below the MCP and long range antiferromagnetic states above this. The equilibrium field-cooled behaviour of alloys with $x \leq 25$ reveals a spontaneous ferromagnetic moment below T_{fg} indicating a spin-glass like "re-entrant" mixed phase. It was also interesting to establish the antiferromagnetic phases in these solid solutions and specifically to confirm whether ferromagnetism exists in disordered alloys

containing less than 50 at. % of Mn. We notice the decrease of the Curie temperature with Mn-content which is due to dominating negative Mn-Mn exchange interactions. In conclusion, we have proved that long range ferromagnetic order can indeed coexist with spin-glass ordering.

ii) The resistivity ρ and magnetoresistance (MR) data show qualitatively different behaviours for $x \geq 25$ and $x \leq 25$ where $x = 25$ is the MCP obtained from the magnetic data. A distinct $-\sqrt{T}$ dependence of resistivity below minima has been found in concentrated Ni_{100-x} Mn_x alloys with $x = 30$, 35, and 37 in the range $5\ K \leq T \leq T_{min/2}$ where T_{min} is around 35 K for all the three samples. Here ρ(T) is analyzed using Mathiessen's rule. The Debye temperature (θ_D) is also found to be ~ 391, 304, and 340 K, respectively for x = 30, 35, and 37 and the value of A ~ (14-29) μΩcm. However, we did not find any minimum for x = 15, 20, and 25 samples though we got distinct kinks/point of inflection around their ferro-spin glass transition (T_{fg}). The variation is more or less linear beyond T_{fg}. The Debye temperature (θ_D) is found to be 485, 346, and 226 K respectively for x =15, 20, and 25 (375 K for pure Ni) and the value of A ~ (40-83) μΩcm is much larger than that of Ni ~ 20 μΩcm. This significant enhancement of the magnetic scattering in these Ni-Mn alloys from that of pure Ni is very likely to come from disorder in the system. Besides these resistivity measurements, the MR measurements also have distinct different behavior below and above the MCP. The MR of the alloys with $x \leq 25$ is negative whereas those for $x \geq 25$ are positive and are governed by different mechanisms.

iii) The second system of alloys that we have studied is Ni-rich γ-$Ni_{100-x-y}Fe_xCr_y$ ($1 \leq x \leq 6$, $18 \leq y \leq 23$) ternary alloys around the permalloy composition The present compositions of alloys belong to the category where Ni-Ni interaction is ferromagnetic whereas Fe-Fe and Cr-Cr interactions are both antiferromagnetic.We have studied the critical phenomenon and the magnetic phase transitions in Ni-rich NiFeCr ternary alloys by using ac susceptibility and dc magnetization measurements near T_C. We have made a comprehensive study on the critical phenomenon at the PM-FM phase transition. This transition is identified to be second order in nature. We have also studied ac-susceptibility as functions of applied magnetic fields and frequency. The measurement of both real and imaginary part of χ_{ac} was helpful in identifying distinct magnetic phases. We have determined the values of T_C, β, γ, and δ from various techniques and they match reasonably well. The values are in between those theoretically

predicted by 3D Heisenberg and mean-field models but closer to the 3D Heisenberg values. It is significant that with these critical exponents, magnetization, field, and temperature (*M-H-T*) data follow the scaling equation. This result is quite surprising because the substitution of Cr is expected to destroy long-range FM order and induce formation of FM clusters, making the system more 3D Heisenberg-like. Moreover, the inhomogeneous magnetic state both below and above T_C may have serious consequences on critical behaviour. This study points toward the fact that critical phenomenon in disordered ferromagnets could not be tackled with the common universality classes, indicating perhaps they represent separate class. This should prompt further experimental studies followed by rigorous theoretical works.

iv) Detailed electrical resistivity and magnetoresistance measurements in γ-$Ni_{100-x-y}Fe_xCr_y$ ($1 \leq x \leq 6$, $18 \leq y \leq 23$) alloys have been made in the temperature range of $2 \leq T \leq 300$ K. The resistivity data of all the alloys exhibit distinct minima lying between 10 and 24 K, nearly unaffected by external magnetic fields. Below the minima, the resistivity is well described by the electron-electron (e-e) interaction effects ($\rho \propto -\sqrt{T}$), independent of the magnetic states of the alloys. Besides the e-e interaction effects, magnetic ($\rho \propto T^2$) and phonon ($\rho \propto T^3$) contributions have been distinctly isolated. The values of the coefficient of the magnetic term come out to be of the same order as the theoretical one ($10^{-5}\mu\Omega$ cm K^{-2}). This clearly shows that the magnetic contribution to the electrical resistivity arises due to the s-d and s-s scattering. Further, the nature of magnetoresistance (MR) at different temperature range (or at different magnetic states) is found to be different. In the spin-glass regime, the system exhibits a strong hysteresis/memory effects at low magnetic fields (up to ~ 1000 Oe) while we found negative MR at ferromagnetic states and it changes sign to positive as soon as the samples enter antiferromagnetic states. An attempt should be made to calculate this resistivity behavior by theoretical approaches and compare them with our experimental results.

7.2 Future Directions

Like any other studies the present one also has left us with a few problems for future investigations. The future aim of our work is to study different disordered magnetic alloys

irrespective of the form (bulk or thin film) and to look for exotic magnetic and transport behavior. In future, we want to prepare by pulse laser deposition technique (PLD) thin films of $Ni_{100-x}Mn_x$ and $Ni_{100-x-y}Fe_xCr_y$ alloys for better understanding of the physics of metallic alloys and their possible applications as nano-devices. A deviation of magnetic properties from bulk values is what is expected. The samples will be characterized with more sensitive and sophisticated instruments. The magnetization study of these thin films will be carried out as functions of applied magnetic fields as well as temperatures. The applied temperature may be high according to the requirements. The field and frequency dependence of the ac-susceptibility will also be studied for finding the magnetic phases. The magneto resistance measurement will be carried out as we expect Giant Magneto Resistance (GMR) in the temperature range 2-300K. The motivation behind this investigation will be to understand the spin-dependent scattering and the relative orientation of magnetizations in neighboring layer as well as interlayer exchange coupling.